Geochimica et Cosmochimica Acta 352 (2023) 133–156

Contents lists available at ScienceDirect

Geochimica et Cosmochimica Acta

journal homepage: www.elsevier.com/locate/gca

# Uranium and molybdenum isotope evidence for globally extensive marine euxinia on continental margins and in epicontinental seas during the Devonian-Carboniferous Hangenberg Crisis

Shuai Yang [a,b,*], Xinze Lu [b], Xinming Chen [c,d], Wang Zheng [e], Jeremy D. Owens [c], Seth A. Young [c], Brian Kendall [b]

[a] Department of Energy and Resources Engineering, College of Engineering, Peking University, 100871 Beijing, China
[b] Department of Earth and Environmental Sciences, University of Waterloo, 200 University Avenue West, Waterloo, Ontario N2L 3G1, Canada
[c] Department of Earth, Ocean, and Atmospheric Science, National High Magnetic Field Laboratory, Florida State University, Tallahassee, FL 32306, USA
[d] School of Oceanography, Shanghai Jiao Tong University, Shanghai 200030, China
[e] School of Earth System Science, Institute of Surface-Earth System Science, Tianjin University, 300072 Tianjin, China

ARTICLE INFO

*Associate editor:* Susan H. Little

*Keywords:*
Uranium isotope
Molybdenum isotope
Hangenberg Crisis
Mo-U Mass balance model
Redox conditions

ABSTRACT

The end-Devonian Hangenberg Crisis was one of the biggest Phanerozoic mass extinctions. However, the mechanism(s) that triggered this event is still debated. In this study, multiple geochemical paleoredox proxies (redox-sensitive trace metals [e.g., Mo, U, Re, V] and isotope systems [Mo, U, S, C]) were applied to the Exshaw Formation black shales to infer ocean redox conditions during the Hangenberg Crisis. The measured $\delta^{13}C_{org}$ values generally decrease upsection in the Exshaw Formation. The Exshaw black shales have increasing maturity levels from east to west in the Western Canada Sedimentary Basin. Large sulfur isotope fractionations (–15‰ to 65‰) between original seawater sulfate and pyrite is best explained by microbial sulfate reduction during deposition and early diagenesis rather than thermochemical sulfate reduction. Precise Re-Os ages previously reported for the Exshaw Formation suggest that metal geochemical signatures in these shales, including over-mature shales, were minimally affected by hydrocarbon maturation and reflected depositional conditions. Both Sr/Ba and TS/TOC ratios (the latter only from immature shales affected minimally by hydrocarbon generation) suggest predominantly brackish and marine settings with significant water exchange between the basin and open ocean. The TOC contents, redox-sensitive trace metal concentrations (Mo, U, Re), and Fe speciation indicate local bottom waters ranged from suboxic (with sulfidic pore waters) to euxinic. The authigenic $\delta^{98}$Mo and $\delta^{238}$U values for the Exshaw shales range from 0.3‰ to 1.1‰, and from –0.23‰ to 0.39‰, respectively. The $\delta^{98}$Mo of the Exshaw Formation may have been offset to lower values than coeval seawater because of a local particulate Fe-Mn shuttle and/or local weakly euxinic bottom waters. Two different correlation patterns (positive correlation and no correlation) of $\delta^{238}$U and U enrichment factors (EF) were observed for Exshaw black shales deposited from locally euxinic bottom waters. The positive correlation group samples (−0.13‰ to 0.23‰) suggest U isotope fractionations (0.4‰ to 0.8‰) between sediments and seawater like those observed in modern euxinic basins. Higher $\delta^{238}$U values (>0.2‰) in the no correlation group suggest even larger U isotope offsets (0.8–1.2‰) from seawater, possibly associated with removal of U into organic floccule layers during deposition. Applying the above Mo and U isotope fractionations to the Exshaw shales, global seawater $\delta^{98}$Mo and $\delta^{238}$U at the Devonian-Carboniferous boundary (DCB) may have been in the range of 1.4‰ to 1.9‰ and −0.9‰ to −0.5‰, respectively. A Mo and U isotope mass balance model suggests a large areal extent of euxinic seafloor (6–10%) at the DCB, which could be pervasive along continental margins and in epicontinental seas during transgression. Therefore, our data support expanded ocean euxinia at the DCB as an important contributor to the Hangenberg Crisis.

* Corresponding author at: Department of Energy and Resources Engineering, College of Engineering, Peking University, 100871 Beijing, China.
*E-mail address:* s244yang@pku.edu.cn (S. Yang).

https://doi.org/10.1016/j.gca.2023.04.027
Received 1 October 2022; Accepted 25 April 2023
Available online 18 May 2023

## 1. Introduction

The Late Devonian (385–359 Ma) had several mass extinction events, notably the Givetian-Frasnian (G-F) Taghanic event, the Frasnian-Famennian (F-F) Kellwasser events, and the end-Devonian Hangenberg Crisis (Ryder, 1996; McGhee et al., 2013; Formolo et al., 2014; Kaiser et al., 2011, 2016; Martinez et al., 2019; Paschall et al., 2019; Zhang et al., 2020a; Tolokonnikova and Ernst, 2021). The ca. 359 Ma Hangenberg Crisis at the Devonian-Carboniferous boundary (DCB) is characterized by ~20% extinction of marine invertebrate species (e.g., cephalopods, gastropods) and ~50% of vertebrates (Walliser, 1996; Sandberg et al., 2002; Scholze and Gess, 2017). However, the triggers of the event are still debated. Several killing mechanisms have been proposed, such as glaciations and associated global cooling (Brezinski et al., 2008; Isaacson et al., 2008), ocean anoxia and euxinia (Kazmierczak et al., 2012; Liu et al., 2019; Zhang et al., 2020a; Sahoo et al., 2023), volcanism (Paschall et al., 2019; Pisarzowska et al., 2020; Rakociński et al., 2021), and supernova explosions (Fields et al., 2020).

Expanded ocean anoxia/euxinia is one of the leading triggers to explain the Hangenberg Crisis, with supporting evidence from sedimentary facies changes and geochemical data (e.g., black shale deposition, C and S isotopes, Fe speciation, redox-sensitive trace metal abundances; Brand et al., 2004; Buggisch and Joachimski, 2006; Kaiser et al., 2006, 2008, 2016; Marynowski and Filipiak, 2007; Cramer et al., 2008; Myrow et al., 2011; Marynowski et al., 2012; Kumpan et al., 2013, 2014; Matyja et al., 2014; Cole et al., 2015; Liu et al., 2019; Li et al., 2022a; Sahoo et al., 2023). An increase in carbonate $\delta^{13}C$ values during the Hangenberg Event coincided with widespread black shale deposition, and both have been interpreted as the consequence of enhanced organic carbon burial (Walliser, 1996; Kaiser et al., 2006). In addition, a previous study reported Mo isotope data for the Hangenberg Black Shales (HBS) in the Carnic Alps, the Rhenish Massif, Thuringia, and the Holy Cross Mountains (Pisarzowska et al., 2020). These Mo isotope data were interpreted to reflect development of anoxic/euxinic redox conditions in the wake of large igneous province magmatism during HBS deposition (Ernst et al., 2020). Carbonate U isotope data from the Long'an section (South China Craton) were used to infer global ocean redox conditions at the DCB (Zhang et al., 2020a). A U isotope mass balance model suggested that >5% of the seafloor was covered by anoxic waters during the Hangenberg Crisis (Zhang et al., 2020a); this estimate may reflect the extent of euxinia, not overall anoxia, given generally larger U isotope fractionations in euxinic versus non-euxinic settings. More recently, a Mo elemental mass balance model was used to derive a lower estimate of ~0.5–1% for the extent of seafloor euxinia based on data from the Bakken Shale (Sahoo et al., 2023). Hence, the global extent of ocean euxinia during the Hangenberg Crisis remains poorly understood and has yet to be explored by the combined use of Mo and U isotope data from black shales.

The Mo and U isotope systems in black shales have been widely utilized to evaluate Earth's ocean oxygenation and biogeochemical evolution (e.g., Arnold et al., 2004; Algeo and Lyons, 2006; Poulson et al., 2006; Scott et al., 2008; Dahl et al., 2010, 2014; Montoya-Pino et al., 2010; Scott and Lyons, 2012; Zhou et al., 2012; Reinhard et al., 2013; Chen et al., 2015; Kendall et al., 2009, 2011, 2013, 2017; Andersen et al., 2017; Lau et al., 2017; Lu et al., 2017, 2020, 2023; Yang et al., 2017; Cheng et al., 2018; Chen et al., 2019; Ostrander et al., 2019; Kendall, 2021; McDonald et al., 2022; Gangl et al., 2023; Kipp et al., 2022; Clarkson et al., 2023). Both Mo and U isotope mass balance models can be used together to quantitatively constrain the extent of ocean euxinia (e.g., Dahl et al., 2011; Goldberg et al., 2016; Gilleaudeau et al., 2019; Stockey et al., 2020; Kipp and Tissot, 2022). Since reconstruction of ancient global ocean redox conditions by a single proxy could result in large uncertainties, the combination of the Mo and U isotope systems is more robust (Asael et al., 2013; Kendall et al., 2015, 2020; Lu et al., 2017, 2020; Cheng et al., 2020; Stockey et al., 2020; Pan et al., 2021). To assess the influence of expanded ocean euxinia as a driver of the Hangenberg Crisis, we investigated redox-sensitive trace metal enrichments and multiple isotope systems (authigenic Mo, authigenic U, pyrite S, and organic C) of the end-Devonian Exshaw Formation in western Canada.

## 2. Geological background

Western Canada was in an equatorial location facing Panthalassa during the Late Devonian (Fig. 1; Witzke and Heckel, 1988; Savoy, 1990; Robison, 1995; Pratt and van Heerde, 2016). The Exshaw Formation was deposited in an epeiric sea within the Western Canada Sedimentary Basin (WCSB), which trends approximately northwest to southeast between the Western Cordillera and Canadian Shield and occupies an area of $\sim 1.4 \times 10^6$ km$^2$ (Piggott and Lines, 1991; Robison, 1995; Creaser et al., 2002; Porter et al., 2014; Wang et al., 2018a). The Exshaw Formation is known for its critical stratigraphic horizon spanning the DCB and economic importance as an abundant hydrocarbon source rock in western Alberta (Fig. 1; Leenheer, 1984; Creaney and Allan, 1991; Selby and Creaser, 2003; Warren and Cooper, 2017). It extends from the outcrop in the thrust and fold belt of the Canadian Rockies eastward in the subsurface across Alberta and southern Saskatchewan (Robison, 1995) and is stratigraphically equivalent to the Bakken Shale (Leenheer, 1984; Smith and Bustin, 1998, 2000).

The Exshaw Formation consists of lower member Famennian and Tournaisian non-calcareous and calcareous black shales, and a Tournaisian upper member of siltstone to silty limestone (Fig. 2). It rests upon carbonates of the underlying Famennian Palliser Formation with minor disconformity, which resulted from a transgression onto the Alberta platform during the Famennian (Richards and Higgins, 1988; Caplan et al., 1996; Caplan and Bustin, 1999, 2001; Selby and Creaser, 2003; Porter et al., 2014). At the Jura Creek area (the type section) in western Alberta, the Exshaw Formation has a thickness of ~47 m, with a 9.3 m thick lower member and a 37.4 m thick upper member (Richards and Higgins, 1988; Smith and Bustin, 2000; Selby and Creaser, 2005). In stratigraphically ascending order at the Jura Creek area, the lower member is characterized by 1–6 cm of basal sandstone-conglomerate, 6.9 m of non-calcareous to calcareous black shale, and 2.4 m of calcareous black shale (Selby and Creaser, 2005). These shales were deposited below storm wave base (Richards and Higgins, 1988). The upper member consists of predominantly siltstone, which was deposited in a shallowing and regressing sea (Savoy, 1990).

The age of the Exshaw Formation and its relationship to the Hangenberg Crisis is constrained by both biostratigraphy and geochronology. Conodont species *Polyganthus communis* and *Siphonodella cooperi* (Fig. 2; MacQueen and Sandberg, 1970; Higgins et al., 1991; Savoy and Harris, 1993) were found in the uppermost part of the lower black shale unit in southwestern Alberta (~51°N, 115°W), and indicate an Early Tournaisian age (MacQueen and Sandberg, 1970; Savoy and Harris, 1993; Selby and Creaser, 2003). Lower member black shales in central Alberta (~54°N, ~118°W) contain *S. duplicate* conodont species that are between the *duplicate* Zone and Lower *S. crenulata* Zone, thus corresponding to an age from the Late Famennian to Early Tournasian (Creaser et al., 2002). Therefore, the Exshaw Formation was likely deposited spanning the DCB boundary. The Hangenberg Crisis lasted ca. 100–300 kyr and occurred between the Middle *praesulcata* and *sulcata* Zones (Fig. 2; Richards and Higgins, 1988; Selby and Creaser, 2005; Myrow et al., 2014; Kaiser et al., 2016; Scholze and Gess, 2017). Although the exact lower boundary of the Hangenberg Crisis in the Exshaw Formation is difficult to identify due to the sparse fossil occurrence, the lower black shale member in this study from the Peace River area is constrained within the *expansa* and *praesulcata* Zones, thus covering the Hangenberg Crisis (Selby and Creaser, 2003; Johnston et al., 2010). An age of 363.3 ± 0.4 Ma was obtained for the Exshaw Formation by U-Pb monazite geochronology on a tuff unit close to the base of the lower black shale member (Richards et al., 2002). This age is similar to the U-Pb zircon age (363.6 ± 1.6 Ma) of volcanic units within

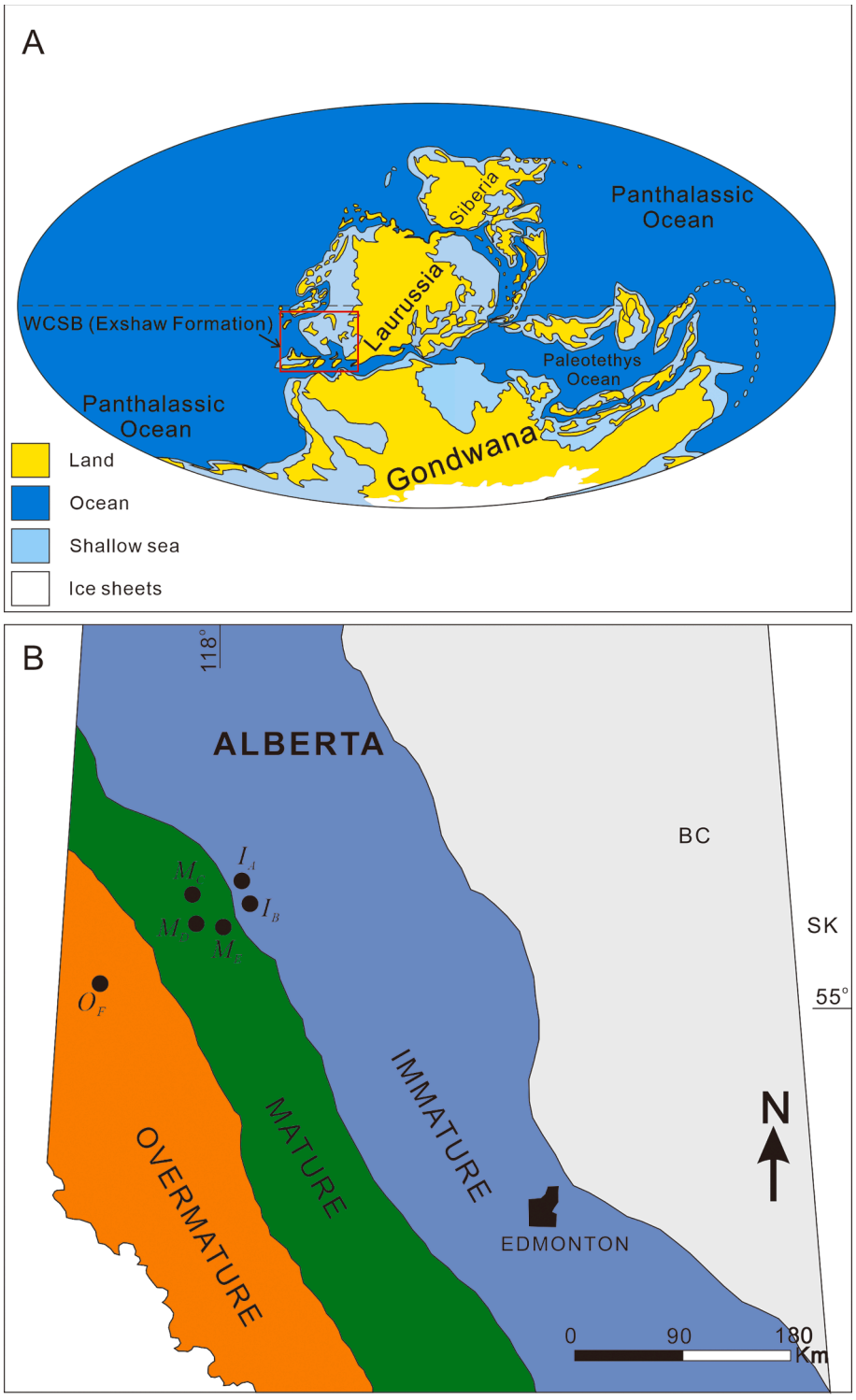


**Fig. 1.** (A) Paleogeographic map for the Late Devonian (modified from Scotese and McKerrow, 1990). The red rectangle refers to the position of the Western Canada Sedimentary Basin (Exshaw Formation). (B) Regional map showing the drill cores with Exshaw Formation black shales and the spatial extent of hydrocarbon maturity levels throughout the study area (modified from Piggott and Lines, 1991; Creaser et al., 2002). Drill cores 13-18-180-23W5 (denoted as $I_A$ hereafter) and 3-19-80-23W5 ($I_B$) are in the immature area. Drill cores 14-22-80-02W6 ($M_C$), 6-19-78-25W5 ($M_D$), and 8-29-78-01W6 ($M_E$) are in the mature area. Drill core 4-23-72-10W6 ($O_F$) is in the overmature area.

the Upper *expansa* Zone in New Brunswick (Tucker et al., 1998). The lower calcareous and upper non-calcareous black shales of the Exshaw Formation at the Jura Creek section yielded a Re-Os depositional age of 361.3 ± 2.4 Ma, directly constraining the age of the DCB boundary (Selby and Creaser, 2005). Considering the uncertainties, these ages are consistent with the timing of the DCB (358.9 ± 0.4 Ma; Cohen et al., 2013) and supports deposition of the Exshaw Formation black shale member during the Hangenberg Crisis.

The coincidence between deposition of the Exshaw Formation's lower black shale member in the Peace River area and the Hangenberg Crisis is further supported by organic carbon isotope data ($\delta^{13}C_{org}$). A previous study reported a negative $\delta^{13}C_{org}$ excursion during deposition of the Exshaw Formation lower black shale member from core 8-23-080-24W5 in the Peace River area (Caplan and Bustin, 1998). This negative $\delta^{13}C_{org}$ excursion is contemporaneous with the Hangenberg Crisis in several countries (i.e., Austria, Canada, Germany, Italy, Poland, United States; Fig. 2) and occurs during the onset of the positive $\delta^{13}C_{carb}$ excursion (which peaks in overlying Carboniferous strata; Pisarzowska et al., 2020; Ferri et al., 2021; Heath et al, 2021).

The maturity levels of the Exshaw Formation were determined by

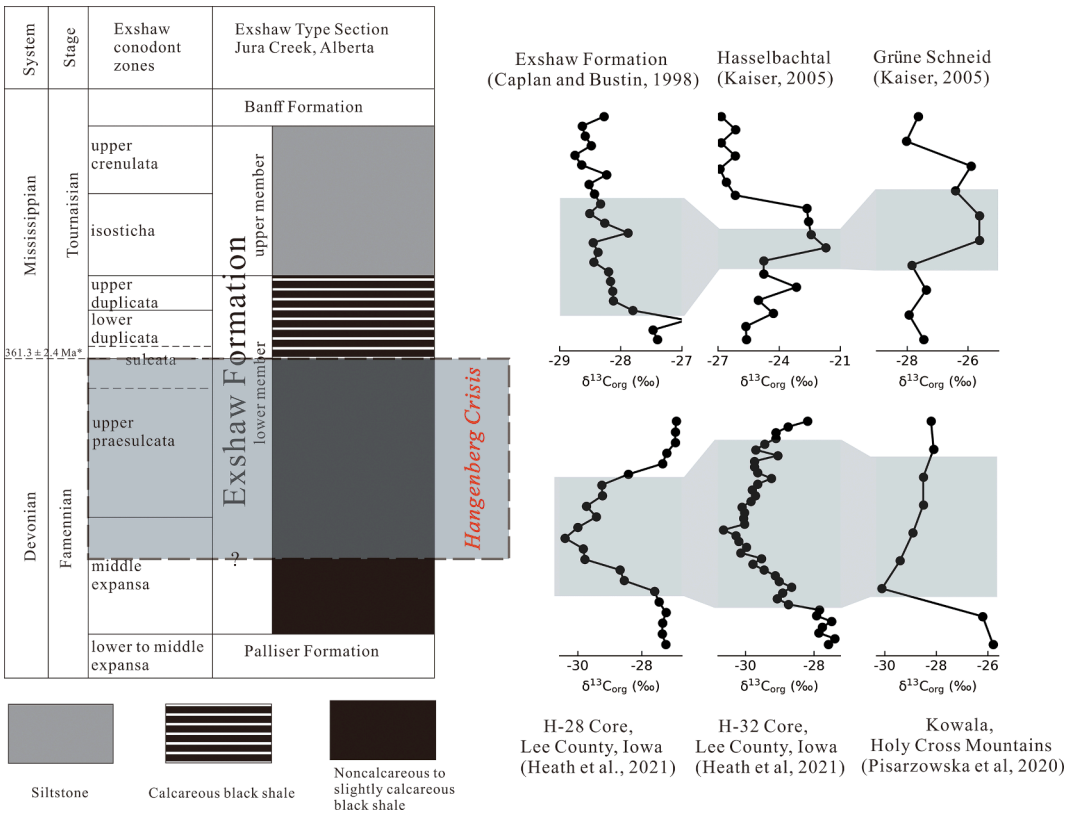


**Fig. 2.** Stratigraphic column of the Exshaw Formation. Dashed line denotes the Devonian-Carboniferous boundary. "*" represents Re-Os age (modified from the Jura Creek type section in Selby and Creaser, 2005). The shaded area in the stratigraphic column refers to the duration of the Hangenberg Crisis (Kaiser et al., 2016). "?" represents the estimated boundaries. The carbon isotope data are from previous studies, with the shaded areas in the carbon isotope profiles coeval with the Hangenberg Crisis.

Rock-Eval pyrolysis (Creaser et al., 2002). The parameter $T_{max}$ was used to evaluate sample hydrocarbon maturity level, which represents the temperature of peak hydrocarbon release by kerogen cracking in the Rock-Eval pyrolyzer (Creaser et al., 2002). The defined $T_{max}$ thresholds for immature, mature, and overmature shales are below 435 °C, between 435 °C and 465 °C, and above 465 °C, respectively (Peters, 1986). The $T_{max}$ of the Exshaw Formation increased westwards, in terms of hydrocarbon maturation levels, from immature to overmature (Piggott and Lines, 1991; Creaser et al., 2002). The boundaries between thermal maturity zones are roughly parallel to the Cordilleran orogenic front (Piggott and Lines, 1991; Creaser et al., 2002; Selby and Creaser, 2003).

## 3. Samples and analytical methods

### 3.1. Samples

Fifty-eight samples of organic-rich black shales from the Exshaw Formation were obtained from the Alberta Core Research Centre, Calgary, Alberta, Canada. Samples were collected from six drillcores that contain the entire Exshaw Formation black shale member with different hydrocarbon maturities over a lateral scale of >150 km. The six drillcores have differences in overall thickness and abundance of carbonate compared to the Jura Creek area (Fig. 2). In the immature and mature cores, the black shale member consists of ~1–5 m of generally non-calcareous black shales (see Table 1S for elemental data), sometimes interbedded with carbonates. The thicker Exshaw interval in the overmature core (~12.5 m) contains more calcareous shales. The upper contact of the Exshaw black shales in all cores is with siltstones. The number of samples taken from each core depended on the thickness of the Exshaw Formation, lithology, and quality of core preservation (i.e., stratigraphically intact core versus disaggregated core material). Specifically, there are 8 samples from immature core 3-19-80-23W5 ($I_A$), 8 samples from immature core 13-18-80-23W5 ($I_B$), 6 samples from mature core 14-22-80-02W6 ($M_C$), 7 samples from mature core 6-19-78-25W5 ($M_D$), 3 samples from mature core 8-29-78-01W6 ($M_E$), and 26 samples from overmature core 4-23-72-10W6 ($O_F$). All samples lacked obvious carbonate/quartz interbeds/veins and diagenetic macroscopic pyrite nodules.

### 3.2. Analytical methods

#### 3.2.1. TOC and elemental analyses

Total organic carbon (TOC) contents were measured at the Agriculture and Food Laboratory, University of Guelph. Total carbon (TC) and total inorganic carbon (TIC, with pre-ashing used to remove organic carbon) contents were measured by combustion in an Elementar Vario Macro Cube CN combustion analyzer. The United States Geological Survey (USGS) Pennsylvanian Brush Creek Shale (SBC-1) served as the reference standard and the accuracy was within 10% of the certified value. The TOC contents were calculated as the difference between TC and TIC. Total sulfur (TS) contents were measured via combustion in an ELTRA instrument at Activation Laboratories Ltd. The SBC-1 reference standard was analyzed along with samples and the accuracy was within 5% of the certified value. Sediment $C_{org}$/P ratios were calculated as 30.97/12 × TOC/P for all samples (Algeo and Ingall, 2007; Algeo and Li, 2020).

Major, minor, and trace element concentration measurements, ion exchange purification of Mo and U, and U isotope analyses were carried out at the Metal Isotope Geochemistry Laboratory, Department of Earth and Environmental Sciences, University of Waterloo. Analytical protocols for elemental analyses followed Kendall et al. (2020) and are briefly summarized here. A known amount (~100 mg) of sample

powder was ashed overnight at 550 °C in crucibles to destroy organic matter and then transferred to Savillex Teflon beakers for digestion in several rounds of concentrated HF-$HNO_3$-HCl acids at 110 °C. A portion of the digested solution was dried and diluted in 2% $HNO_3$, and an Agilent 8800 triple quadrupole inductively coupled plasma mass spectrometer (QQQ-ICP-MS) was used to measure elemental concentrations. The USGS black shale standards SBC-1, Eocene Green River Shale (SGR-1b), and Devonian Ohio Shale (SDO-1) were used as secondary standards to verify instrument accuracy (within 10%). Procedural blank levels (<1%) were negligible for all elements of interest.

Aluminum-normalized enrichment factors (EF) relative to average upper crust were used to determine the authigenic enrichment relative to detrital background (McLennan, 2001; Tribovillard et al., 2006):

$$EF = \frac{(element/Al)_{sample}}{(element/Al)_{average\ \ upper\ \ crust}}$$

### 3.2.2. Sedimentary iron speciation

Iron speciation data were obtained from the National High Magnetic Field Laboratory (NHMFL) at Florida State University (FSU). For all samples, we calculated the approximate degree of pyritization ($DOP_T$) as 55.85/64.12 × total sulfur (TS) / total Fe ($Fe_T$) (Algeo et al., 2008; Algeo and Li, 2020). It has been shown that $DOP_T$ generally underestimates true DOP, so we have obtained true Fe speciation data for most samples analyzed for Mo and U isotope compositions.

Sedimentary Fe speciation analyses followed the protocols in Poulton and Canfield (2005). Iron pools associated with carbonates ($Fe_{carb}$), oxide minerals ($Fe_{ox}$), and magnetite ($Fe_{mag}$) were sequentially extracted using acetate, dithionite, and oxalate solutions, respectively (Poulton and Canfield, 2005). After each iron extraction, an aliquot of the solution was taken and analyzed on an Agilent 7500cs quadrupole ICP-MS. The pyrite iron content ($Fe_{py}$) was determined by the gravimetric yields of extracted $Ag_2S$ from samples using the chromium reducible sulfides extraction method modified from Canfield et al. (1986), and assuming a stoichiometry of $FeS_2$:$Ag_2S$ of two. The $Fe_T$ contents were measured along with other major and trace metal concentrations (see Section 3.2.1). Highly reactive iron ($Fe_{HR}$) was calculated as the sum of these four species: $Fe_{carb}$, $Fe_{ox}$, $Fe_{mag}$, and $Fe_{py}$. The $Fe_{HR}/Fe_T$ ratios are used to infer local redox conditions of oxic or anoxic bottom waters and the $Fe_{py}/Fe_{HR}$ ratios are used to determine if the anoxic waters were ferruginous or euxinic (Poulton and Canfield, 2011; Raiswell et al., 2018; see details in Section 5.2.2).

### 3.2.3. Molybdenum isotope analyses

Molybdenum isotope analyses were performed at the Metals, Environment, and Terrestrial Analytical Laboratory (METAL) at Arizona State University (ASU). Purification of Mo from digested sample solutions was conducted following the analytical protocols in Kendall et al. (2020). Prior to ion-exchange chromatography, a known amount of $^{97}Mo$-$^{100}Mo$ double spike was added to sample solutions for instrumental mass fractionation correction. BioRad AG1-X8 100–200 mesh resin and BioRad AG50W-X8 200–400 mesh resin were used for Mo anion column chemistry and subsequent Mo cation column chemistry, respectively. Sample $\delta^{98}Mo$ relative to the NIST-SRM-3134 standard was calculated using the equation below (Nägler et al., 2014):

$$\delta^{98}Mo\ (‰) = \left[\frac{(^{98}Mo/^{95}Mo)_{sample}}{(^{98}Mo/^{95}Mo)_{NIST-SRM-3134}} - 1\right] \times 1000 + 0.25$$

In practice, the $\delta^{98}Mo$ of samples were first measured relative to ASU's in-house standard RochMo2 via standard-sample bracketing. The NIST-SRM-3134 standard was measured during the same analytical sessions as the samples and had an average $\delta^{98}Mo$ of 0.32 ± 0.02 ‰ (2SD; n = 4) relative to RochMo2. Hence, 0.07‰ was subtracted from the $\delta^{98}Mo$ of each sample relative to RochMo2 to yield the sample $\delta^{98}Mo$ relative to NIST-SRM-3134 = 0.25‰.

During this study, the USGS SDO-1 standard yielded $\delta^{98}Mo$ of 0.81 ± 0.02‰ (2SD, n = 3) relative to NIST-SRM-3134 = 0.0‰, which translates to 1.06 ± 0.02‰ (2SD, n = 3) relative to NIST-SRM-3134 = 0.25‰. The first value shows an excellent agreement with the long-term average $\delta^{98}Mo$ of 0.82 ± 0.11‰ (2SD, n = 145) measured at ASU (Goldberg et al., 2013). The uncertainty of a sample is reported as the 2SD of sample replicate measurements or the long-term reproducibility of SDO-1 (0.11‰), whichever is greater.

The authigenic Mo isotopic composition ($\delta^{98}Mo_{auth}$, relative to NIST-SRM-3134 = 0.25‰) is calculated as below to correct for the detrital Mo:

$$\delta^{98}Mo_{auth}\ (‰) = \delta^{98}Mo_{sample} - (Al/Mo)_{sample} \times \frac{\delta^{98}Mo_{detrital} - \delta^{98}Mo_{sample}}{\left(\frac{Al}{Mo}\right)_{detrital} - \left(\frac{Al}{Mo}\right)_{sample}}$$

The average upper crust values of Al (8.04 wt%) and Mo (1.50 ppm) are used to represent detrital Al and Mo contents (McLennan, 2001) and the $\delta^{98}Mo_{detrital}$ is assumed to be 0.3‰ (Voegelin et al., 2014; Willbold and Elliott, 2017).

### 3.2.4. Uranium isotope analyses

Purification of U for isotope analyses was made following the protocols in Weyer et al. (2008) and Kendall et al. (2020). To correct for instrumental mass fractionation, prior to ion-exchange chromatography, a known amount of $^{236}U$-$^{233}U$ double spike (IRMM-3636) was added to each sample solution that contains 300–500 ng sample U such that the U sample/spike ratio is ~30. Eichrom® UTEVA resin was used for U column chemistry. The U isotope compositions ($\delta^{238}U$) of 100 ppb solutions were measured on a Nu Plasma II MC-ICP-MS equipped with an Aridus II desolvating nebulizer system. Double-spiked CRM145 and CRM129a were measured every 2 and 10 samples, respectively, to monitor the drift of the instrumental mass bias. Sample $\delta^{238}U$ data are reported relative to the bracketing CRM145 standards as follows:

$$\delta^{238}U\ (‰) = \left[\frac{(^{238}U/^{235}U)_{sample}}{(^{238}U/^{235}U)_{CRM145}} - 1\right] \times 1000$$

Measurements of CRM145 and CRM129a during this study yielded average $\delta^{238}U$ values of 0.00 ± 0.08‰ (2SD, n = 140) and −1.42 ± 0.08‰ (2SD, n = 41), respectively. As reviewed by Andersen et al. (2017), heterogeneity exists in the CRM129a standards from different laboratories (i.e., variable $\delta^{238}U$ values have been reported), so our specific CRM129a standard solution is used only to monitor long-term reproducibility. The measured CRM129a value in this study is in excellent agreement with the reported CRM129a value (−1.42 ± 0.09‰, 2SD, n = 46) in Lu et al. (2023), which did the analyses in the same lab. Measurement of the three USGS black shale standards (SDO-1, SBC-1, SGR-1b) was used to make an interlaboratory comparison. The average $\delta^{238}U$ values of SBC-1 (−0.28 ± 0.07‰, 2SD, n = 7), SDO-1 (−0.13 ± 0.08‰, 2SD, n = 4), and SGR-1b (−0.21 ± 0.08‰, 2SD, n = 8) are consistent with published $\delta^{238}U$ data for these rock standards from several laboratories (Kendall et al., 2015, 2020; Tissot and Dauphas, 2015; Lu et al., 2017, 2020, 2023; Rolison et al., 2017; Yang et al., 2017; Brüske et al., 2020). In addition, we measured the $\delta^{238}U$ of one sample (KPR14) from the Kettle Point Formation and obtained a value of 0.16 ± 0.07‰ (2SD, n = 3) that is consistent with the previously reported $\delta^{238}U$ of 0.20 ± 0.06‰ (2SD, n = 3, measured at Arizona State University) by Kendall et al. (2020). Therefore, the accuracy and precision of U isotope data from our lab is comparable with other laboratories worldwide. The uncertainty of a sample is reported as the 2SD of sample replicate measurements or the long-term reproducibility of CRM145 and CRM129a (0.08‰), whichever is greater.

The authigenic U isotopic composition ($\delta^{238}U_{auth}$, relative to CRM145) is calculated using the equation below:

$$\delta^{238}U_{auth}\ (‰) = \delta^{238}U_{sample} - (Al/U)_{sample} \times \frac{\delta^{238}U_{detrital} - \delta^{238}U_{sample}}{\left(\frac{Al}{U}\right)_{detrital} - \left(\frac{Al}{U}\right)_{sample}}$$

The average upper crust values of Al (8.04 wt%) and U (2.80 ppm) are used to represent detrital Al and U contents (McLennan, 2001) and the $\delta^{238}U_{detrital}$ is assumed to be –0.3‰ (Tissot and Dauphas, 2015; Noordmann et al., 2016).

#### 3.2.5. Pyrite sulfur isotope analyses

Pyrite sulfur isotope compositions ($\delta^{34}S_{py}$) were measured at the Isotope Science Laboratory, University of Calgary. The procedure followed the protocols in Mayer and Krouse (2004) and Ardakani et al. (2016). The samples were mixed with 10 mL of ethanol and then reacted with a 1 M $CrCl_2$ solution for 2 h. The released $H_2S$ was captured using ZnS and converted to $Ag_2S$ (Mayer and Krouse, 2004). An Elemental Analyzer – Isotope Ratio Mass Spectrometer (EA-IRMS) was used for sulfur isotope analysis. The $^{34}S/^{32}S$ ratios were measured on $SO_2$ produced by thermal decomposition and are reported relative to the international standard Canyon Diablo Troilite (V-CDT) as follows:

$$\delta 34S\,(‰) = \left[\frac{(^{34}S/^{32}S)_{sample}}{(^{34}S/^{32}S)_{V-CDT}} - 1\right] \times 1000$$

Instrumental calibration was done using standards IAEA S1 (−0.3‰ by definition), S2 (22.7 ± 0.2‰), and S3 (−32.6 ± 0.2‰). The precision of sulfur isotope analyses in this study is ~1.0‰ (1SD).

#### 3.2.6. Organic carbon isotope analyses

Organic carbon isotope compositions ($\delta^{13}C_{org}$) were measured at the Environmental Isotope Laboratory, University of Waterloo. Samples were treated with excess amounts of 10% HCl to remove inorganic carbon, washed with nanopure water, and dried on a hotplate. Subsequently, samples were packed in tin capsules and analysed by a Costech 4010 Elemental Analyzer coupled to a Thermo-Finnigan Delta Plus XL continuous flow isotope ratio mass spectrometer. International reference material (NIST-2704) was measured along with samples and the precision is within 0.2‰ (2SD).

## 4. Results

The TOC, TS, elemental data, $C_{org}/P$ ratios, and organic carbon isotope data of the Exshaw Formation black shales are displayed in Table 1S. Element enrichment factors and geochemical ratios are shown in Table 2S. The Mo, U, and pyrite S isotope data as well as sedimentary iron speciation data are listed in Table 3S.

### 4.1. Iron-carbon–sulfur-phosphorus systematics and trace metal enrichments

The TOC contents in the Exshaw Formation black shales from the immature, mature, and overmature cores range from 1.0 wt% to 15 wt% (average [ave.] = 5.2 wt%), 2.2 wt% to 19 wt% (ave. = 7.6 wt%), and 1.3 wt% to 3.5 wt% (ave. = 2.1 wt%), respectively. By comparison, the TIC contents range from 0.1 to 4.6 wt% (ave. = 0.9 wt%), <0.1 to 1.6 wt % (ave. = 0.5 wt%), and 1.0 to 6.4 wt% (ave. = 2.3 wt%) for the immature, mature, and overmature cores, respectively. The TS contents of black shales from the immature, mature, and overmature cores range from 0.9 wt% to 4.2 wt% (ave. = 2.9 wt%), 1.8 wt% to 3.4 wt% (ave. = 2.5 wt%), and 0.3 wt% to 3.1 wt% (ave. = 1.0 wt%), respectively (Table 1S). The $C_{org}/P$ ratios are only determined in the immature cores, considering the loss of organic carbon via thermal maturation in the mature and overmature cores. Most samples in the two immature cores have $C_{org}/P$ ratios > 100 while two samples (1755.66 m and 1756.12 m) have $C_{org}/P$ ratios < 100.

Regarding sedimentary iron speciation, the $DOP_T$ values of the Exshaw Formation shales from the immature, mature, and overmature cores are 0.42–1.11 (ave. = 0.78), 0.59–1.06 (ave. = 0.78), and 0.13–0.78 (ave. = 0.45), respectively, whereas the $Fe_{py}/Fe_{HR}$ ratios range from 0.64 to 0.93 (ave. = 0.85), 0.67 to 0.92 (ave. = 0.86), and 0.65 to 0.77 (ave. = 0.72), respectively. Shales in the immature, mature, and overmature cores have $Fe_{HR}/Fe_T$ ratios that range from 0.08 to 0.64 (ave. = 0.44), 0.08 to 0.46 (ave. = 0.32), and 0.35 to 0.53 (ave. = 0.44), respectively. Samples with the lowest Mo and U EFs have $DOP_T$ values of 0.42–0.46 (from one immature core; Mo and U EFs ~1) and 0.13–0.35 (overmature core; Mo and U EFs ~2–3). Except for two samples with anomalously low $Fe_{HR}/Fe_T$ ratios (0.08) considering their high Mo EFs, a statistically significant correlation occurs between $DOP_T$ and $Fe_{py}/Fe_{HR}$ ($R^2 = 0.63$, $p < 0.01$; Fig. S1). No statistical difference in average $DOP_T$ and $Fe_{py}/Fe_{HR}$ ratios exists for the immature and mature cores, but $DOP_T$ values are consistently ~0.2 lower than $Fe_{py}/Fe_{HR}$ ratios for the overmature core.

Redox-sensitive trace metal concentrations of the Exshaw Formation vary significantly in cores with different maturities. The Mo, U and Re concentrations of black shales from the two immature cores vary considerably from 1.2 ppm to 117 ppm (EF: 1.2–203), 2.4 ppm to 45 ppm (EF: 1.2–42), and 3.9 ppb to 214 ppb (EF: 15–1399), respectively (Table 2S). Similarly, large variations in trace metal concentrations are observed for the three mature cores (Mo: 18–129 ppm, EF: 12–143; U: 6.1–66 ppm, EF: 2.1–39; Re: 11–316 ppb, EF: 27–1303). Generally lower but overlapping trace metal abundances are observed in the overmature core (Mo: 1.3–63 ppm, EF: 1.6–62; U: 2.1–21 ppm, EF: 2.1–9.5; Re: 6.8–89 ppb, EF: 44–230). Vanadium concentrations of black shales in the immature (91–1021 ppm; EF: 1.3–17) and mature cores (338–1460 ppm; EF: 4.5–23) span a wide range but most samples are characterized by high V concentrations (>500 ppm). In comparison, black shales from the overmature core have V concentrations (76–810 ppm; EF: 2.4–13) that are generally lower compared to the immature/mature cores.

Several geochemical ratios are calculated for the Exshaw Formation black shales (Figs. 3–6). Molybdenum concentrations are not well-correlated with total sulfur or pyrite iron (i.e., representing pyrite sulfur) contents regardless of thermal maturity. The Mo and TOC contents of the immature ($R^2 = 0.89$, $p < 0.01$) and mature shales ($R^2 = 0.84$, $p < 0.01$) have good correlations, whereas a weaker correlation was observed for the overmature shales ($R^2 = 0.43$, $p < 0.01$) (Fig. 3). Similarly, both U and TOC contents and Re and TOC contents of the immature and mature shales have good correlations ($R^2 = 0.72$–$0.96$, $p < 0.01$) while the overmature shales yield relatively weaker correlations ($R^2 = 0.41$–$0.60$, $p < 0.01$). By contrast, V and TOC contents yield no correlations ($R^2 < 0.09$, $p > 0.05$) for shales with different thermal maturity levels. Similar average Mo/TOC ratios (in unit of ppm/wt%) are observed for immature (ave. = 9.8, 1.1–15.0, n = 16), mature (ave. = 9.0, 4.8–13.6, n = 16), and overmature (ave. = 8.8, 0.7–24.6, n = 26) shales. The average Mo/U EF ratios of immature, mature, and overmature shales are 5.9 (0.9–8.2, n = 16), 5.4 (2.9–6.6, n = 16), and 4.9 (0.7–10.7, n = 26), respectively (Fig. 4). Good correlations are observed between Mo EF and U EF for immature ($R^2 = 0.97$, $p < 0.01$), mature ($R^2 = 0.83$, $p < 0.01$) and overmature ($R^2 = 0.74$, $p < 0.01$) shales. Most samples from all cores have Mo/U EF ratios between 1 and 3 times the modern seawater Mo/U ratio, whereas a small number of samples have Mo/U EF ratios between 0.1 and 1 times the modern seawater Mo/U ratio. The average Fe/Al ratios of immature, mature, and overmature shales are 0.5 (0.3–0.9, n = 16), 0.5 (0.4–0.8, n = 16), and 0.4 (0.3–0.8, n = 26), respectively. The TS/TOC ratios from all cores range between 0.1 and 1.4. The Sr/Ba ratios from all cores range from 0.19 to 2.9, and mostly are between 0.2 and 1.0.

### 4.2. Molybdenum, uranium, pyrite sulfur, and organic carbon isotope compositions

Overall, the bulk $\delta^{98}Mo$ of the Exshaw Formation black shales from all cores range from 0.26‰ to 1.11‰ (ave. = 0.76 ± 0.25‰, 1SD, n = 18). The bulk $\delta^{238}U$ of these shales range from –0.40‰ to 0.24‰ (ave. = –0.02 ± 0.17‰, 1SD, n = 28).

After detrital correction, the authigenic Mo isotope values ($\delta^{98}Mo_{auth}$) of the Exshaw Formation black shales (0.26–1.12‰, ave. =

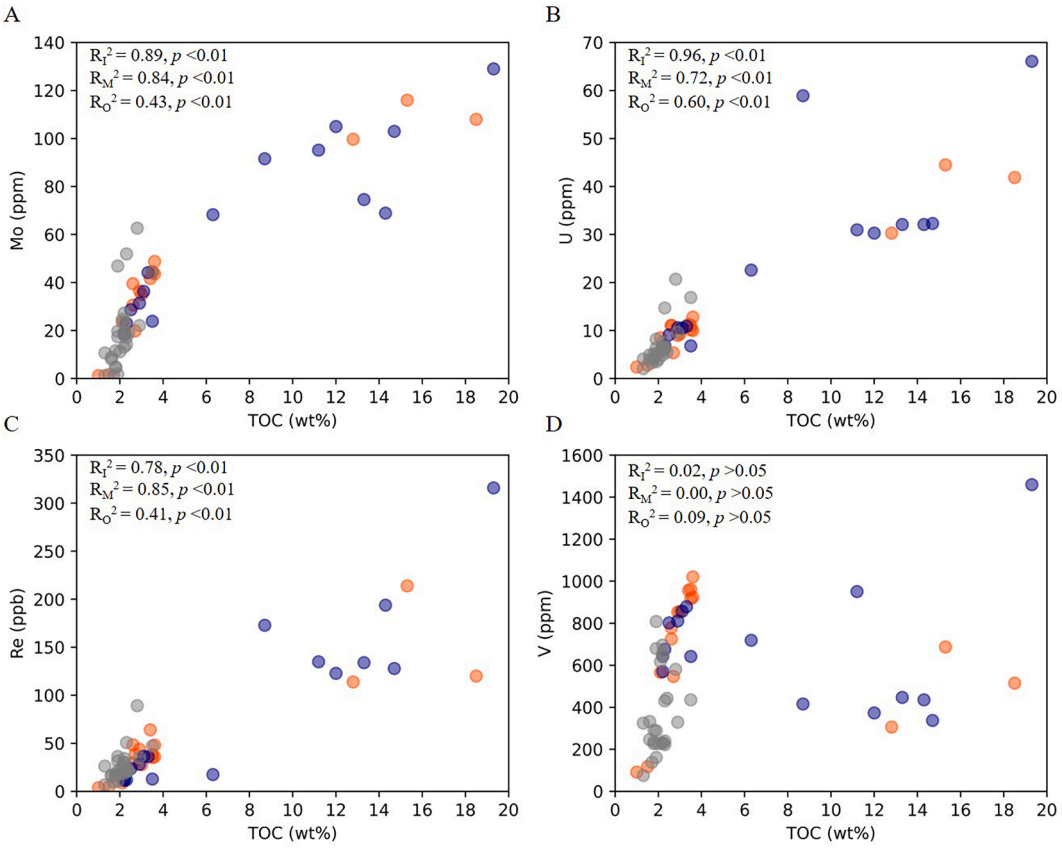


**Fig. 3.** Geochemical diagrams of (A) Mo, (B) U, (C) Re, and (D) V versus TOC contents for the Exshaw Formation black shales in immature (orange), mature (blue), and overmature (grey) zones. $R_I$, $R_O$, and $R_M$ refer to immature, mature, and overmature cores, respectively.

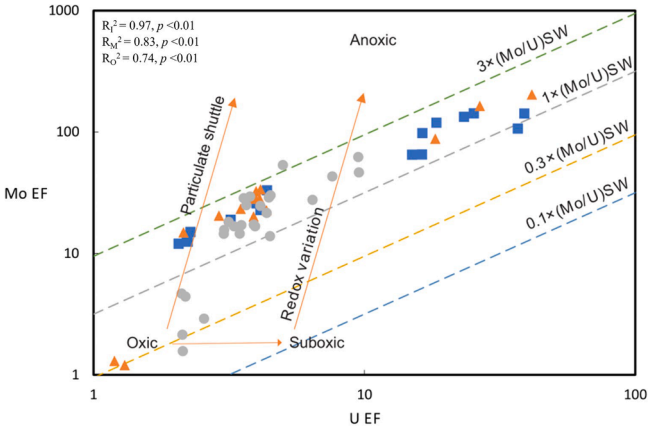


**Fig. 4.** Cross-plot of Mo EF versus U EF for the Exshaw Formation black shales. Orange triangles refer to data from immature cores; blue squares refer to data from mature cores; grey circles refer to data from the overmature core. Dashed lines represent the weight equivalents of the molar Mo/U EF ratios of modern seawater (1 × SW), and corresponding fractions of modern seawater (0.1 × SW, 0.3 × SW, and 3 × SW) (Algeo and Tribovillard, 2009). Enrichment patterns and corresponding controls in the figure are illustrated following Algeo and Tribovillard (2009). $R_I$, $R_O$, and $R_M$ refer to immature, mature, and overmature cores, respectively.

0.77 ± 0.26‰, 1SD, n = 18; Fig. 5; Table 2S) are similar to bulk $\delta^{98}$Mo values. The $\delta^{98}Mo_{auth}$ of black shales from the immature, mature, and overmature cores are 0.76–0.98‰ (ave. = 0.86 ± 0.11‰, 1SD, n = 5), 0.26–1.00‰ (ave. = 0.67 ± 0.28‰, 1SD, n = 9), and 0.41–1.12‰ (ave. = 0.88 ± 0.32‰, 1SD, n = 4), respectively. There is no significant difference in $\delta^{98}Mo_{auth}$ between cores of different hydrocarbon maturity based on unpaired t-tests (p-values of 0.2–0.9 for immature versus mature, immature versus overmature, and mature versus overmature cores).

The $\delta^{238}U_{auth}$ of all Exshaw Formation black shales range from −0.73‰ to 0.39‰ (ave. = 0.03 ± 0.25‰, 1SD, n = 28). Two samples from core $I_A$ have low U EF (<1.5), suggesting detrital U comprises a significant fraction of total U in these samples. The average $\delta^{238}U_{bulk}$ of these two samples is −0.36 ± 0.06‰ (1SD), which is indistinguishable from the upper crust value (−0.29 ± 0.09‰, 1SD; Tissot and Dauphas, 2015; Wang et al., 2018b). Detrital correction for these samples is associated with large uncertainties, and thus the $\delta^{238}U_{auth}$ of the two samples are not used for interpretation of ocean redox conditions. Excluding the two samples, the $\delta^{238}U_{auth}$ of immature, mature, and overmature shales range from −0.13‰ to 0.39‰ (ave. = 0.17 ± 0.18‰, 1SD, n = 7), −0.13‰ to 0.37‰ (ave. 0.11 ± 0.18‰, 1SD, n = 11), and −0.23‰ to 0.32‰ (ave. −0.04 ± 0.17‰, 1SD, n = 8), respectively. Statistically, there is no significant difference between immature and mature shales (p-value of 0.50) as well as mature and overmature shales (p-value of 0.08). However, a p-value of 0.04 was calculated for immature versus overmature shales, suggesting a statistically significant (albeit minor) difference between them.

The overall range of $\delta^{34}S_{py}$ for the Exshaw Formation is from −24.7‰ to 0.9‰ (ave. = −12.9 ± 7.2‰; 1SD, n = 18). Immature, mature, and overmature shales have a range of −22.1‰ to 0.9‰ (ave. = −9.5 ± 10.2‰; 1SD, n = 5), −24.7‰ to −6.9‰, (ave. = −14.5 ± 6.9‰; 1SD, n = 9), and −14.3‰ to −12.9‰, (ave. = −13.4 ± 0.6‰; 1SD, n = 4), respectively (Table 3S). There is no significant difference in $\delta^{34}S_{py}$ between cores of different hydrocarbon maturity based on unpaired t-tests (p-values of 0.3–0.8).

The overall range of $\delta^{13}C_{org}$ for the Exshaw Formation is from

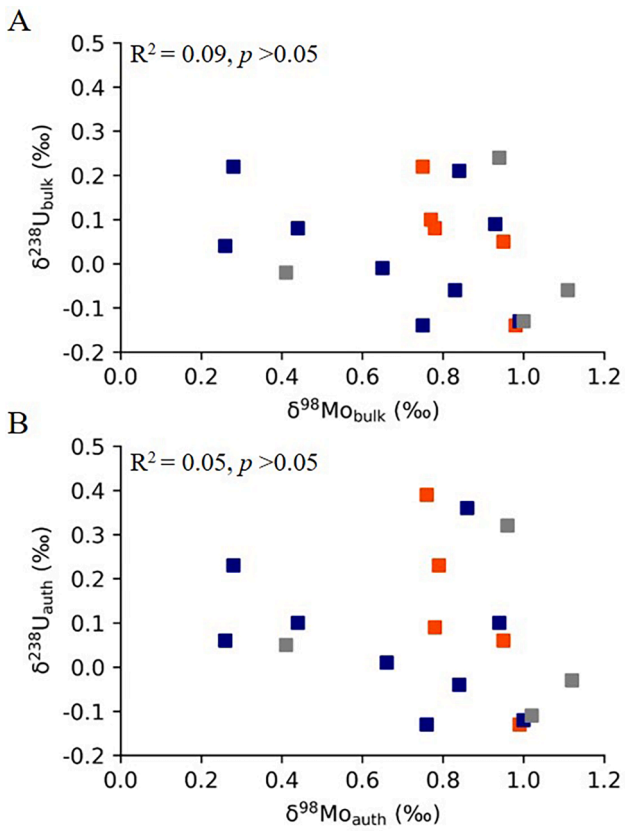


**Fig. 5.** Crossplots of (A) bulk $\delta^{238}U$ versus $\delta^{98}Mo$, and (B) authigenic $\delta^{238}U$ versus $\delta^{98}Mo$. Orange squares refer to immature samples; blue squares refer to mature samples; grey squares refer to overmature samples.

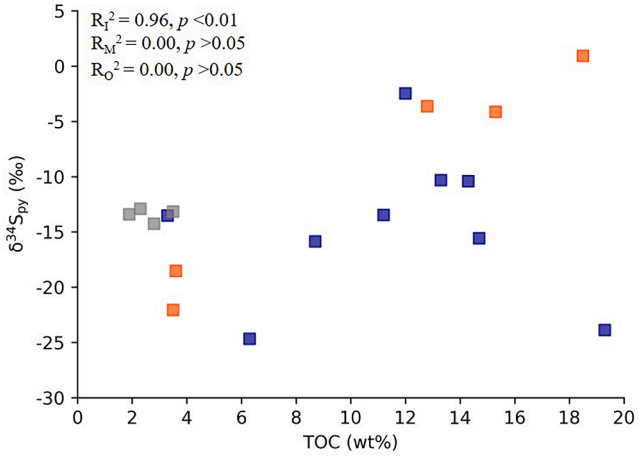


**Fig. 6.** Geochemical diagrams showing the correlation of $\delta^{34}S_{py}$ versus TOC for the immature (orange), mature (blue) and overmature (grey) Exshaw Formation black shales. $R_I$, $R_O$, and $R_M$ refer to immature, mature, and overmature cores, respectively.

−30.02‰ to −27.91‰ (ave. = −29.11 ± 0.45‰; 1SD, n = 58). Specifically, immature, mature, and overmature shales have a range of −29.57‰ to −28.03‰ (ave. = −28.99 ± 0.38‰; 1SD, n = 16), −29.57‰ to −28.03‰ (ave. = −28.75 ± 0.31‰; 1SD, n = 16), and −30.02‰ to −27.91‰ (ave. = −29.41 ± 0.36‰; 1SD, n = 26), respectively (Table 1S). There are no clear stratigraphic trends in $\delta^{13}C_{org}$ for the mature and overmature cores, whereas a general upsection decrease in $\delta^{13}C_{org}$ occurs in the immature cores (Fig. S2-S4).

## 5. Discussion

### 5.1. Evaluation of thermal maturation effects on geochemical paleoredox proxies

Organic-rich mudrocks and shales are characterized by various levels of redox-sensitive metal enrichments based on their depositional conditions. However, post-depositional processes including burial diagenesis and thermal maturation could cause the remobilization of some elements in sediments and alter their original signatures, leading to misinterpretation of the depositional environment (Lev et al., 2000; Algeo and Maynard, 2004; Abanda and Hannigan, 2006). The chemical composition of organic matter (OM) changes during thermal maturation through the loss of functional groups, generation of hydrocarbons, and subsequent change of the molecular compositions (Raiswell and Berner, 1987; Seewald, 2003; Ardakani et al., 2016; Dickson et al., 2020). Among these processes, thermochemical sulfate reduction (TSR) is the redox reaction involving sulfate ($SO_4^{2-}$) reduction and organic matter oxidation at relatively high temperatures (i.e., 80 < T < 200 °C; Orr, 1977; Machel et al., 1995; Cross et al., 2004), with the by-products of bitumen/pyrobitumen, hydrogen sulfide, and carbonates (Machel et al., 1995; Machel, 2001; King et al., 2014). By contrast, microbial sulfate reduction (MSR) occurs at relatively lower temperatures (0 < T < 60–80 °C; Machel et al., 1995) with the same by-products.

The magnitude of sulfur isotope fractionation can be effectively used to differentiate TSR and MSR processes. Previous experimental studies demonstrated that the sulfur isotope fractionation factors between sulfate and $H_2S$ ($\Delta^{34}S_{sulfide-sulfate} = \delta^{34}S_{sulfide} - \delta^{34}S_{sulfate}$) during TSR is temperature-dependent, ranging from –15‰ to –10‰ at 150–200 °C (overmature conditions) and from −20‰ to −15‰ at 100–150 °C (mature conditions) (Krouse et al., 1988; Machel et al., 1995). By comparison, a larger sulfur isotope fractionation is observed for MSR ($\Delta^{34}S_{sulfide-sulfate}$ = −75‰ to −15‰; Harrison and Thode, 1958; Canfield, 2001; Cross et al., 2004; Amrani, 2014; Liseroudi et al., 2021). Kampschulte and Strauss (2004) suggests the seawater $\delta^{34}S_{sulfate}$ values were ~20–30‰ from the Late Devonian to Early Carboniferous. For the Exshaw Formation, the immature shales have $\delta^{34}S_{py}$ from −22.1‰ to 0.9‰ (ave. = −9.5 ± 20.3‰; 2SD, n = 5), yielding $\Delta^{34}S_{sulfide-sulfate}$ of approximately −52.1‰ to −19.1‰ (ave. = −35.6‰). The mature and overmature shales have $\delta^{34}S_{py}$ from −24.7‰ to −2.5‰ (ave. = −14.5 ± 13.6‰; 2SD, n = 9) and from −14.3‰ to −12.9‰ (ave. = −13.4 ± 1.2‰; 2SD, n = 4), respectively. Therefore, the $\Delta^{34}S_{sulfide-sulfate}$ of mature and overmature shales are calculated to range from −54.7‰ to −22.5‰ (ave. = −38.6‰) and from −44.3‰ to −32.9‰ (ave. = −38.6‰), respectively. The large S isotope fractionations for both mature and overmature shales are similar to the immature shales and are like those of MSR rather than TSR, suggesting a predominantly microbial origin for pyrite formation in the Exshaw black shales.

Thermal maturation does not seem to have significantly altered depositional geochemical records. Firstly, unpaired t-tests of $\delta^{98}Mo_{auth}$ and $\delta^{34}S_{py}$ yield no statistically significant differences for black shales under different hydrocarbon thermal maturities (see Section 4.2 above), suggesting minimal effects of thermal maturation on these isotope systems. Even though there is a small significant difference in $\delta^{238}U_{auth}$ between immature and overmature shales (p-value = 0.04), distinctive local depositional conditions can explain this difference (see Section 5.3.2). Secondly, cross plots between $\delta^{34}S_{py}$ and TOC for mature and overmature shales do not show any negative correlations (Fig. 6). This observation is consistent with the minimal influence of TSR, given that this process has been shown previously to cause negative correlations between $\delta^{34}S_{py}$ and TOC contents due to the OM depletion caused by TSR (Ardakani et al., 2016).

Our interpretation of a limited influence of hydrocarbon maturation on the Exshaw shale metal geochemistry is also supported by previous studies (Raiswell and Berner, 1987; Cruse and Lyons, 2004; Selby and Creaser, 2005; Ross and Bustin, 2009; Dickson et al., 2020, 2022). Ross

and Bustin (2009) suggested minimal alteration of whole-rock geochemical signatures for the Devonian-Carboniferous thermally mature shales from northern British Columbia (Canada), based on the strong correlations between trace metal abundances (e.g., Mo, U, Re, V) and TOC contents. Although thermal maturation could cause a 40–60% decrease in TOC in fine-grained sedimentary rocks (Raiswell and Berner, 1987), the loss of metals is not necessarily associated with this process due to the bond with high weight molecular organics and low permeability of shales (Abanda and Hannigan, 2006). Some metals (e.g., Mo) originally associated with organic matter might be recaptured by other phases (e.g., sulfides) within shales (Helz et al., 1996; Helz and Vorlicek, 2019). Importantly, a precise Re-Os depositional age from overmature shales of the Exshaw Formation agrees with independent U-Pb zircon age constraints for the Devonian-Carboniferous boundary, demonstrating minimal effects of hydrocarbon maturation on the Re-Os radioactive isotope system (Selby and Creaser, 2005). Since the geochemical behavior and shale host phases (organic matter and sulfide minerals) of Re are similar to some other redox-sensitive trace metals (RSTMs) (e.g., Mo, U, V), the accurate Re-Os age suggests the RSTMs were not disturbed by overmature conditions. In addition, thermal maturation is suggested to minimally influence the Mo, U, Cd, and Zn isotope compositions for Jurassic organic-rich shales (Dickson et al., 2020, 2022).

Although the loss of trace metals (Mo, U, Re, V) was negligible during thermal maturation, the TOC contents of mature and overmature shales were probably influenced through maturation. The TOC contents of both immature and mature shales vary considerably (1.0–15 wt% and 2.2–19 wt%, respectively), whereas the overmature shales have a smaller range of generally lower TOC contents (1.3–3.5 wt%). The overmature shales have relatively poor correlations between trace metals (Mo, U, Re, V) and TOC contents, compared to immature and mature shales (Fig. 3). Lower TOC contents and poor correlations between trace metals and TOC contents are consistent with loss of TOC from the overmature shales via hydrocarbon generation and expulsion. Thus, some geochemical ratios of thermally overmature shales (e.g., trace metals/TOC, TS/TOC) cannot be used to reconstruct paleodepositional conditions. In addition, although trace metals were retained by the shales during thermal maturation, their concentrations could be indirectly elevated due to the loss of TOC. In this scenario, metal ratios (e.g., Mo/U) are more reliable tools than individual metal concentrations to infer depositional environmental conditions.

In summary, we conclude that there was no significant overprinting of the depositional geochemical records for immature and mature shales from the Exshaw Formation. However, there may have been some loss of TOC in the overmature (and possibly mature) shales due to thermal maturation, thus influencing the use of ratios involving TOC to infer depositional conditions. Nonetheless, the metal isotope systems do not seem to be significantly altered through maturation and can be applied to reconstruct global ocean redox conditions during Exshaw deposition.

### 5.2. Elemental constraints on the local depositional environment of the Exshaw Formation

#### 5.2.1. Paleosalinity and paleohydrographic conditions

Paleosalinity and paleohydrographic geochemical proxies provide valuable insights on the reconstruction of depositional environments in ancient sedimentary basins. Among the paleosalinity elemental proxies, the strontium/barium (Sr/Ba) and total sulfur/total organic carbon (TS/TOC) ratios have been proposed as effective proxies to distinguish between marine, brackish, and freshwater conditions during deposition (e.g., Hieshima and Pratt, 1991; Chen et al., 1997; Ge et al., 2003; Zhang et al., 2017; Wei and Algeo, 2020; Kendall et al., 2020). Based on data from modern basins with various hydrographic conditions, sediments deposited from marine, brackish, and fresh waters have Sr/Ba ratios of >0.5, 0.2–0.5, and <0.2, respectively (Wei and Algeo, 2020). The threshold of TS/TOC ratios are suggested to be <0.1 for freshwaters and > 0.1 for brackish-marine conditions (Wei and Algeo, 2020). The TS/TOC ratios cannot effectively distinguish between brackish and marine conditions for ratios of 0.1–0.5 because the extent of MSR depends on both sulfate and labile organic matter availability. Higher TS/TOC ratios (>0.5) are more likely to indicate marine settings. The accuracies of these two proxies are 66% for Sr/Ba and ~91% for TS/TOC, respectively, for modern environments (Wei and Algeo, 2020).

For the Exshaw Formation, overall, the Sr/Ba and TS/TOC ratios widely range from 0.20 to 2.86 (ave. = 0.57) and from 0.14 to 1.41 (ave. = 0.62), respectively. The immature shales were minimally affected by hydrocarbon maturation and have Sr/Ba ratios and TS/TOC ratios of 0.20–1.06 (ave. = 0.38) and 0.16–1.41 (ave. = 0.86), respectively, both of which suggest brackish to marine depositional settings. The mature and overmature shales have Sr/Ba ratios of 0.20–1.87 (ave. = 0.47) and 0.28–2.86 (ave. = 0.72), respectively, pointing to brackish or marine conditions. Considering Sr is able to substitute for $Ca^{2+}$ in carbonate minerals (Brand and Veizer, 1980; Wei and Algeo, 2020), some high Sr/Ba ratios (i.e., 1.87, 2.86) from the mature and overmature shales may be affected by diagenetic modification and/or high carbonate contents. The TS/TOC ratios from mature and overmature shales are not used to infer paleosalinity due to the potential loss of TOC during thermal maturation. Thus, the lower black shale member of the Exshaw Formation was deposited in brackish to marine settings where there was at least moderate water exchange with the open ocean.

#### 5.2.2. Constraints on local redox conditions from iron speciation and Mo, U, and Re abundances

Iron speciation and RSTM enrichments (e.g., Mo, U, Re) in sediments are used to infer local water column paleoredox conditions (Tribovillard et al., 2006; Algeo and Tribovillard, 2009; Scott et al., 2017; Bennett and Canfield, 2020). Based on iron speciation data from modern and ancient sediments, $Fe_{HR}/Fe_T > 0.38$ typically indicates anoxic bottom waters whereas $Fe_{HR}/Fe_T < 0.22$ suggests oxic bottom waters (Poulton and Raiswell, 2002; Poulton and Canfield, 2011). Ratios of $Fe_{HR}/Fe_T$ between 0.22 and 0.38 may indicate oxic or anoxic conditions, depending on local factors such as sedimentation rates and changes to Fe speciation or loss of highly reactive iron during diagenesis and metamorphism (Lyons and Severmann, 2006; Poulton and Canfield, 2011; Raiswell et al., 2018; Eroglu et al., 2021). When the bottom water is anoxic, the $Fe_{py}/Fe_{HR}$ ratios can distinguish euxinic conditions (>0.7–0.8) from ferruginous conditions (<0.7–0.8) although false euxinia signatures may arise from pyritization during diagenesis (Poulton and Canfield, 2011; Raiswell et al., 2018; Eroglu et al., 2021). Calibrations between $DOP_T$ values and $Fe_{py}/Fe_{HR}$ ratios (including a consistent difference of ~0.2 for the overmature core) for the Exshaw Formation suggest that $DOP_T$ values $\leq 0.4$ point to oxic/suboxic bottom waters while values $\geq 0.6$ suggest water column euxinia, which could be further used to constrain local redox conditions. In addition, it is important to also use redox-sensitive trace metal data to independently infer local redox conditions. Trace metals (Mo, U, Re) are soluble in oxygenated waters and are removed into sediments under anoxic conditions (Morford and Emerson, 1999; Tribovillard et al., 2006; Algeo and Tribovillard, 2009; Algeo and Li, 2020; Kendall, 2021). Removal of Mo mainly depends on the occurrence of aqueous hydrogen sulfide ($[H_2S]_{aq}$), whereas U and Re removal do not require $[H_2S]_{aq}$ but more generally $O_2$-deficient bottom waters and sediment pore waters (Anderson et al., 1989; Barnes and Cochran, 1990; Emerson and Huested, 1991; Colodner et al., 1993; Morford and Emerson, 1999; Morford et al., 2005; Tribovillard et al., 2006; Algeo and Tribovillard, 2009; Scott and Lyons, 2012; Algeo and Li, 2020; Algeo and Liu, 2020).

The Mo, U, and Re concentrations of Exshaw black shales from an immature core $I_A$ suggest variable bottom water redox conditions (Fig. 7). The sample at 1753.78 m has the highest TOC (19 wt%), $DOP_T$ value (1.11), and RSTM concentrations (Mo: 108 ppm, U: 42 ppm, Re: 120 ppb), suggesting a short interval of intense bottom water euxinia. This is consistent with a high $C_{org}/P$ ratio (>100) and high Mo/U EF

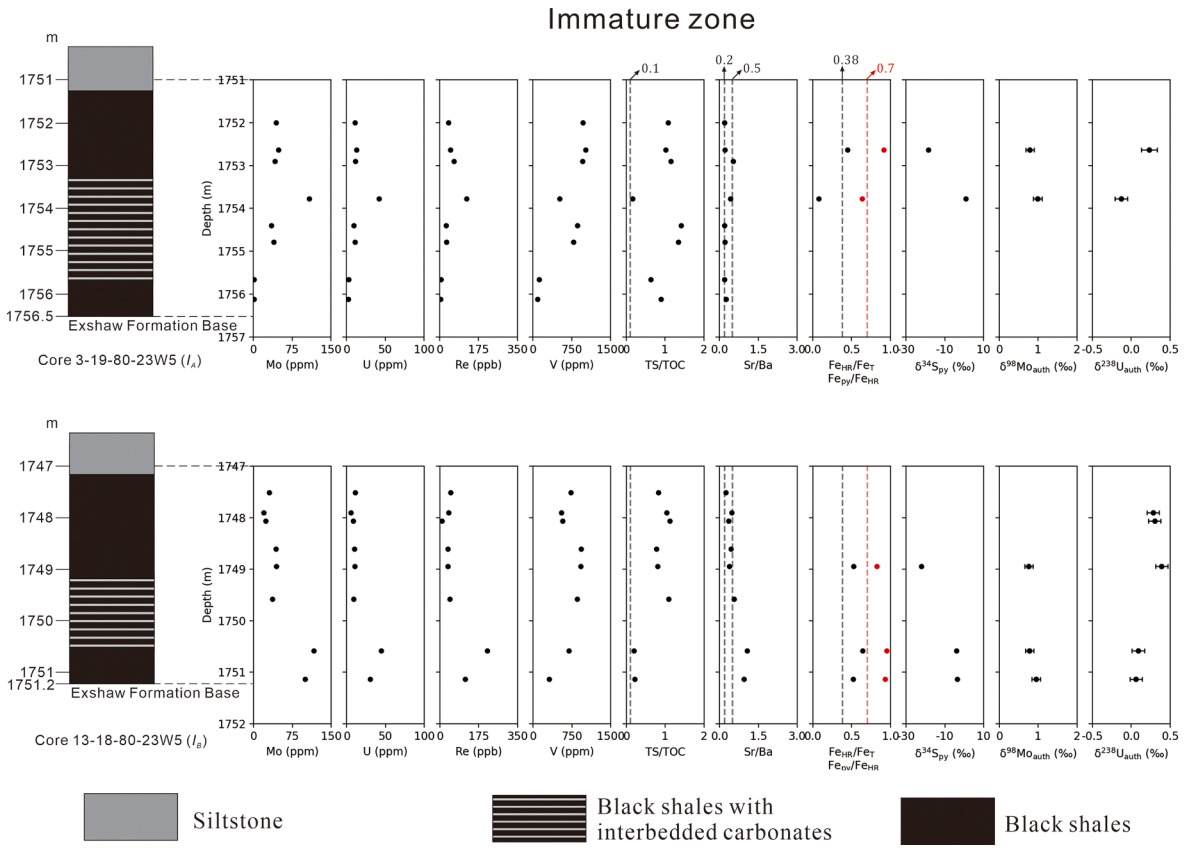


**Fig. 7.** Geochemical profiles for the Exshaw Formation in drillcores from the immature zone. The base of the Exshaw Formation in each drillcore is labeled at the bottom of the core stratigraphic log, corresponding to the depth of 1756.5 m ($I_A$), 1751.2 m ($I_B$), respectively. Black dashed lines in the TS/TOC subfigure refer to TS/TOC of 0.1 (higher values indicate brackish-marine conditions) (Wei and Algeo, 2020). Black dashed lines in the Sr/Ba subfigure refer to Sr/Ba of 0.2 (lower values indicate fresh waters) and 0.5 (higher values indicate marine waters), respectively (Wei and Algeo, 2020). Black dashed lines in the $Fe_{HR}/Fe_T$ subfigure refer to $Fe_{HR}/Fe_T$ of 0.38 (higher values unambiguously indicate local bottom water anoxia) and red dashed lines refer to $Fe_{py}/Fe_{HR}$ of 0.7 (higher values indicate local bottom water euxinia) (Poulton and Canfield, 2011). Error bars are the reported 2SD for each sample's Mo and U isotope compositions. The legend for stratigraphic log, dashed lines in the subfigures, and error bars are also applied for Fig. 8 and Fig. 9.

ratio for this sample that falls between 1 and 3 times the modern seawater Mo/U ratio ($[Mo/U]_{SW}$; Fig. 4). A low $Fe_{HR}/Fe_T$ ratio (0.08) for this sample suggests oxic bottom waters but is probably a false signal (possibly arising from the loss of highly reactive iron during diagenesis) considering the high Mo, U, Re, TOC content, $DOP_T$ value, and Mo/U ratio of this sample (Raiswell et al., 2018). The two stratigraphically lowest samples below 1755 m have the lowest Mo, U, Re, and TOC contents, $DOP_T$ values, $C_{org}/P$ ratios, and Mo/U ratios, suggesting the most oxygenated conditions. The other samples have intermediate Mo, U, Re, and TOC contents, $C_{org}/P$ ratios, and $DOP_T$ values that are consistent with suboxic/anoxic (with sulfidic pore waters) to less intensely euxinic bottom water conditions (Table 1S).

The geochemical profiles of the other immature core ($I_B$) and two mature cores ($M_C$, $M_D$) show different stratigraphic trends (Figs. 7–8). In these cores, the stratigraphically lower intervals are enriched in Mo (>60 ppm), U (>20 ppm), Re (>100 ppb), and TOC (>5 wt%), and have high $Fe_{HR}/Fe_T$ (mostly > 0.38), $Fe_{py}/Fe_{HR}$ (>0.8), and $DOP_T$ values (>0.78) that collectively point to predominantly euxinic bottom waters. The stratigraphically higher intervals contain <60 ppm Mo, <20 ppm U, <50 ppb Re, and <5 wt% TOC. Two of the more Mo-rich samples (1748.94 m in $I_B$ and 2006.69 m in $M_D$) from the higher intervals (~44 ppm for Mo and ~10 ppm for U) have Fe speciation data that suggest euxinic bottom water conditions ($Fe_{HR}/Fe_T$ > 0.38, $Fe_{py}/Fe_{HR}$ > 0.8, $DOP_T$ > 0.71). The less Mo-rich samples from the higher intervals of all three cores have $DOP_T$ > 0.59, suggesting deposition under euxinic bottom waters. Nearly all samples from both intervals have Mo/U EF ratios between 1 and 3 times modern $[Mo/U]_{SW}$, suggesting a faster Mo removal rate over U because of locally euxinic bottom waters that preferentially removed Mo to sediments relative to U, and/or an Fe-Mn particulate shuttle that accelerates Mo delivery to sediments compared to U (Algeo and Tribovillard, 2009).

The other mature core ($M_E$) has features similar to the lower intervals in cores $I_B$, $M_C$, and $M_D$. All three samples in core $M_E$ have relatively high trace metal concentrations and TOC contents (Mo > 60 ppm, U > 20 ppm, Re > 100 ppb and > 5 wt% TOC). Two samples (2099.12 m and 2099.3 m) have $Fe_{HR}/Fe_T$ > 0.27, $Fe_{py}/Fe_{HR}$ > 0.87, and $DOP_T$ > 0.73, suggesting euxinic bottom waters. The other sample (2099.0 m) has $Fe_{HR}/Fe_T$ = 0.08 and $Fe_{py}/Fe_{HR}$ = 0.67 that implies non-euxinic conditions but may be a false signal (possibly arising from loss of highly reactive iron during diagenesis) as it contradicts the high trace metal (Mo: 69 ppm; U: 32 ppm; Re: 194 ppb), $DOP_T$ value (0.82), and TOC (14 wt%) enrichments of this sample.

The overmature shales (core $O_F$) exhibit a general upward decreasing trend of Mo, U, and Re concentrations (Mo: 1.3–63 ppm, U: 2.1–21 ppm, Re: 6.8–89 ppb; Fig. 9). Four samples in the stratigraphically lower interval have higher Mo (44–65 ppm) and U (8–21 ppm) concentrations as well as $Fe_{HR}/Fe_T$ (>0.35) and $Fe_{py}/Fe_{HR}$ (>0.7, except for one sample with 0.65) ratios that collectively suggest euxinic bottom waters, although the $DOP_T$ values fall in a range of 0.4–0.6 and we cannot exclude the possibility of non-euxinic conditions with sulfidic pore waters. The Mo/U EF ratios of the stratigraphically lower shales are mostly between 1 and 3 times the modern $[Mo/U]_{SW}$, whereas stratigraphically higher shales mostly have Mo/U EF ratios between 0.1 and 1 times the $[Mo/U]_{SW}$, with some overlap between the two intervals

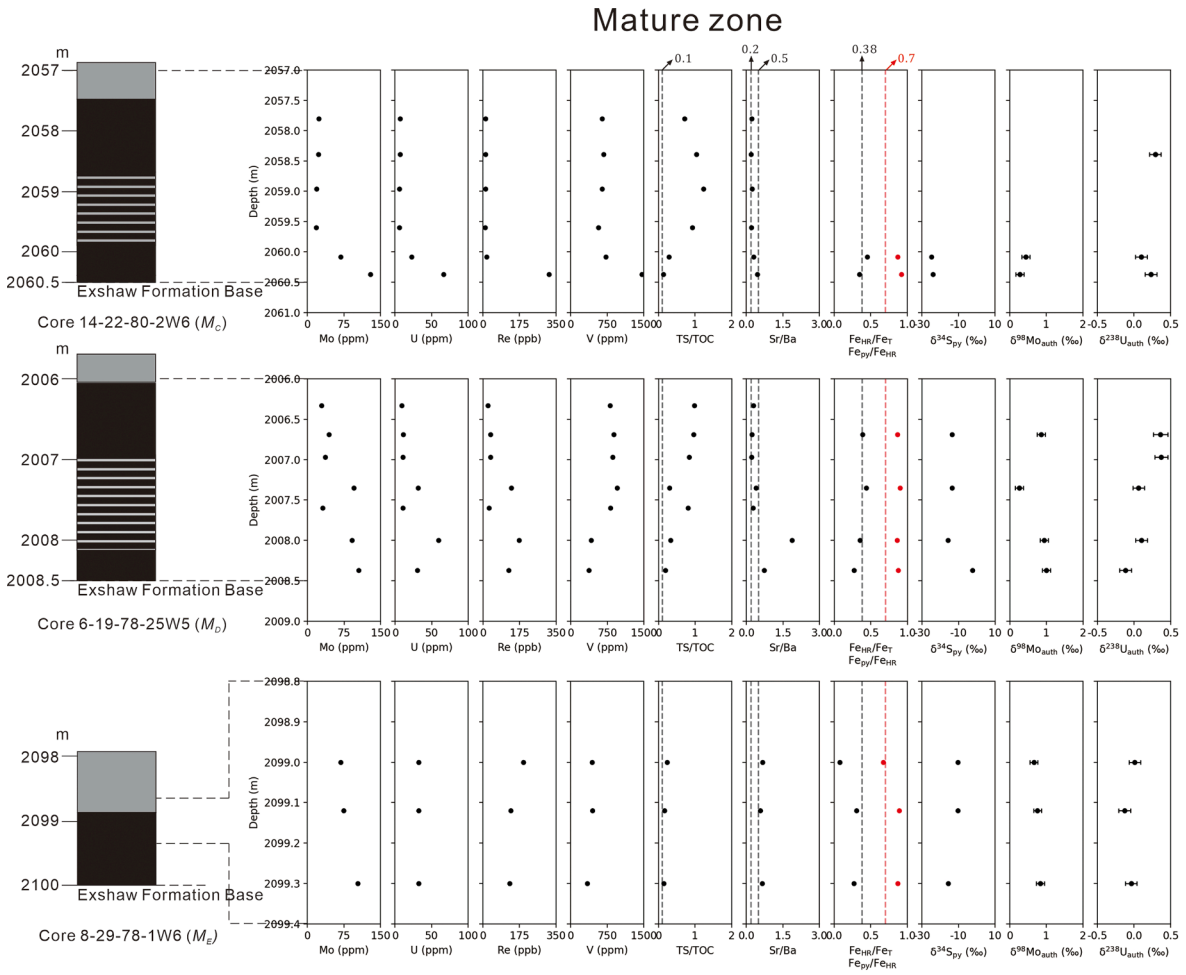


**Fig. 8.** Geochemical profiles for the Exshaw Formation in drillcores from the mature zone. The base of the Exshaw Formation in each drillcore is labeled at the bottom of the core stratigraphic log, corresponding to the depth of 2060.5 m ($M_C$), 2008.5 m ($M_D$), 2100.0 m ($M_E$), respectively.

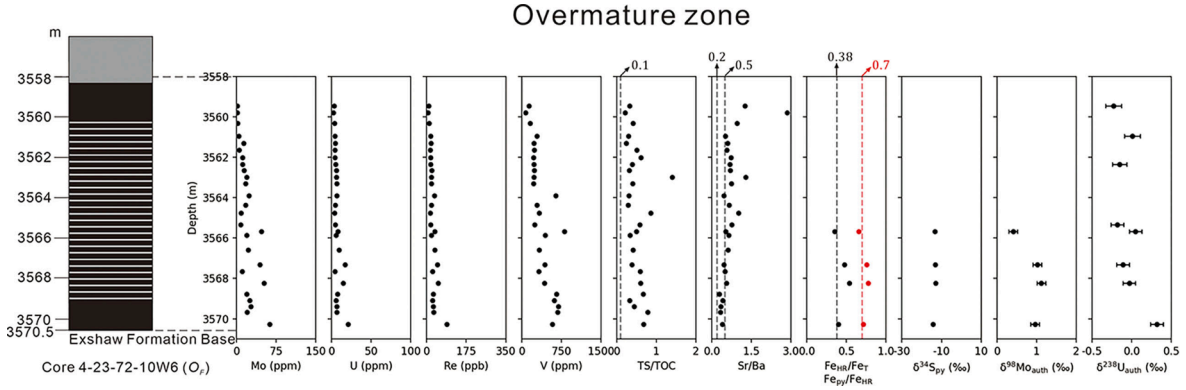


**Fig. 9.** Geochemical profiles for the Exshaw Formation in drillcores from the overmature zone. The base of the Exshaw Formation in each drillcore is labeled at the bottom of the core stratigraphic log, corresponding to the depth of 3570.5 m ($O_F$).

(Fig. 4). Combining the trace metal and iron speciation data, the local bottom waters at this locality may have generally evolved from more reducing to more oxygenated.

The Mo/TOC ratios of immature euxinic sediments are least affected by thermal alteration and provides constraints on the degree of basin restriction because this ratio is a function of the uptake of Mo per unit organic matter and has a positive correlation with the aqueous Mo concentration in bottom waters (Algeo and Lyons, 2006). A high extent of basin restriction leads to a reduced Mo/TOC ratio in euxinic sediments (Algeo and Lyons, 2006). Immature shales exhibit a positive correlation between Mo and TOC ($R^2 = 0.89, p < 0.01$; Fig. 3). Excluding two low-Mo samples (Mo < 2 ppm), the other immature shales were most likely deposited under at least intermittent anoxic/euxinic conditions based on high Mo/U EF ratios (between 1 and 3 times modern $[Mo/U]_{SW}$; Fig. 4), available Fe speciation and RSTM data. These samples yield an average Mo/TOC ratio of 11.0 ± 5.3 ppm/wt% (2SD, n = 14) with a slope of 6 ppm/wt% for the regression line on a plot of Mo versus TOC contents. This value is between the Black Sea (4.5 ± 1 ppm/

wt%) and Cariaco Basin (25 ± 5 ppm/wt%) and suggests at most a moderately restricted basin because expanded global ocean euxinia at the Devonian-Carboniferous boundary compared to the modern ocean should be associated with a lower global oceanic Mo reservoir and thus lower Mo enrichments and Mo/TOC ratios in euxinic black shales (see Section 5.3; Scott et al., 2008). This interpretation is consistent with the paleosalinity indicators (TS/TOC and Sr/Ba ratios).

In addition, the $C_{org}/P$ ratios provide further information regarding local redox conditions, with $C_{org}/P > 100$ suggesting reducing conditions whereas $C_{org}/P < 50$ point to oxidizing conditions (Algeo and Li, 2020). The $C_{org}/P$ ratios between 50 and 100 may represent either oxic or anoxic conditions. Most samples in the two immature cores are characterized by relatively high $C_{org}/P$ ratios (>100), except for two samples (1755.66 m and 1756.12 m) which have $C_{org}/P$ ratios < 100. Such relatively high $C_{org}/P$ ratios in the immature cores further support the interprations made with the other geochemical paleoredox proxies (loss of $C_{org}$ from shales during hydrocarbon maturation precludes robust application of the $C_{org}/P$ proxy to the mature and overmature shales).

#### 5.2.3. Controlling mechanisms on V enrichment

The V concentrations in some cores ($I_A$, $I_B$, $M_D$) exhibit no/weak covariation with other RSTMs (Fig. 10), suggesting additional mechanisms that influence the magnitude of V enrichments. Several processes have been proposed to explain unusually high V enrichments in ancient black shales.

First, "hyper-enrichment" of V (>500 ppm) has been suggested to reflect "hyper-sulfidic" conditions ($[H_2S]_{aq}$ up to 10 mM in porewater in sediments or bottom waters; Scott et al., 2017). The Late Devonian-Early Mississippian Bakken Shale (Williston Basin) was suggested to be deposited under such conditions because of V hyper-enrichment and elevated Mo concentrations (commonly > 200 ppm) (Scott et al., 2017). However, most Exshaw black shales with >500 ppm V have <60 ppm Mo, suggesting that bottom waters were typically not "hyper-sulfidic" because V removal to sediments could occur under low $O_2$ conditions whereas efficient Mo removal relies on the existence of $[H_2S]_{aq}$ in bottom waters (e.g., Morford and Emerson, 1999; Morford et al., 2005; Tribovillard et al., 2006).

Second, V hyper-enrichments in the Exshaw Formation could be explained by the operation of an Fe-Mn particulate shuttle, which accelerates the delivery of V into sediments (Emerson and Huested, 1991; Zhang et al., 2016; Ostrander et al., 2019; Kunert et al., 2020). When the Fe-Mn oxides are reduced and dissolved, the vanadate is released into anoxic waters, reduced to vanadyl form $[VO^{2+}]$, and then removed to the sediment (Emerson and Huested, 1991; Zhang et al., 2016). Those Exshaw samples with a combination of high V enrichments and low $\delta^{98}$Mo (see Fig. 11) provides evidence for the delivery of V and isotopically light Mo to sediments by sinking Fe-Mn oxides (Mn concentrations are low in these rocks because Mn accumulation in sediments is not favored in anoxic conditions; Ostrander et al., 2019; Kunert et al., 2020). For those samples with high V (>500 ppm) but low Mo (<40 ppm) concentrations, V transfer to the sediment may have been more efficient than Mo because of non-euxinic bottom waters (recapture of Mo released from dissolved Fe-Mn particulates requires dissolved sulfide whereas recapture of V does not; Ostrander et al., 2019). By contrast, samples with lower V (<500 ppm) but higher Mo (>50 ppm) concentrations suggest the chemocline was higher in the water column, thus decreasing the delivery of trace metals to sediments via the Fe-Mn particulate shuttle. Under such conditions, the Fe-Mn oxides would be dissolved in the euxinic water column rather than in the sediments, thus releasing metals back into the water column and allowing greater authigenic Mo enrichment over V. The development of photic zone euxinia in epicontinental seas during the Late Devonian (e.g., Scott et al., 2017; Kabanov and Jiang, 2020) can explain samples with lower V but higher Mo concentrations.

Third, it was recently proposed that the formation of clay-organic nanocomposites may promote V enrichments in ancient black shales (Lu et al., 2021). Specifically, V may have been adsorbed to dissolved organic matter (DOM) in the water column, incorporated into clays (e.g., smectite) to form clay-organic nanoparticles, and then released and taken up by illite during diagenesis (Lu et al., 2021). This process could potentially explain the V enrichments in the Exshaw black shales but there are no strong correlations between V and TOC contents that is expected for V delivery by clay-organic nanoparticles (Fig. 3).

#### 5.2.4. Summary of local depositional conditions

Based on the paleosalinity and paleoredox geochemical data of the Exshaw Formation, the main conclusions for the local depositional environment are: 1) the local sedimentary basin had brackish-marine conditions and had at least a moderate connection to the open ocean; 2) the local redox conditions varied from suboxic (with sulfidic pore waters) to euxinic; and 3) the operation of an Fe-Mn particulate shuttle and/or formation of clay-organic nanoparticles may have significantly enhanced V delivery to the sediments, especially for the samples that have high V (>500 ppm) concentrations.

### 5.3. Constraints on the extent of Devonian-Carboniferous ocean euxinia from Mo and U isotopes

#### 5.3.1. Mo isotopes

Molybdenum isotope compositions of euxinic organic-rich mudrocks have been utilized as a global ocean paleoredox proxy for two decades (see Kendall et al., 2017 for a review). The main source of ocean Mo is rivers and groundwaters, with low-temperature seafloor hydrothermal systems being a minor source (Moore, 1996; McManus et al., 2002; Miller et al., 2011; Reinhard et al., 2013; King and Pett-Ridge, 2018; Neely et al., 2018). Molybdenum in oxic seawater exists as soluble molybdate but in euxinic settings molybdate converts to thiomolybdate

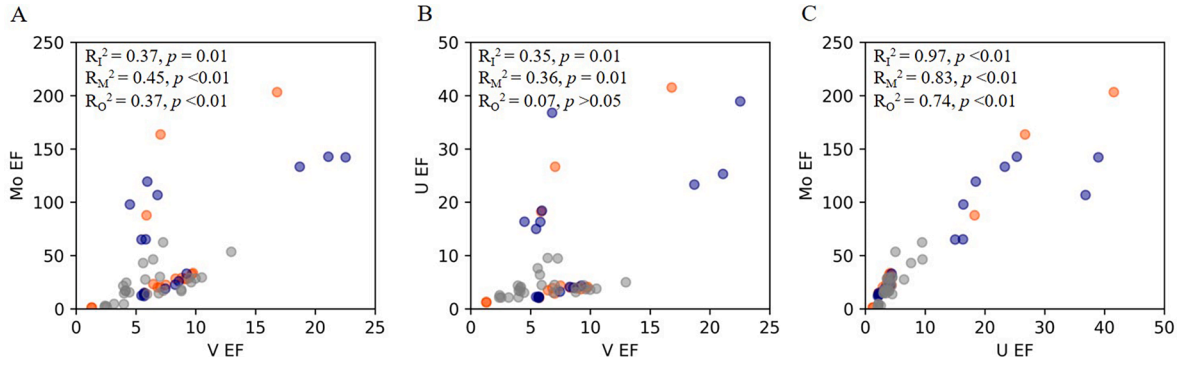


**Fig. 10.** Geochemical diagram showing cross-plots of (A) Mo EF versus V EF, (B) U EF versus V EF, and (C) Mo EF versus U EF for the Exshaw Formation black shales in the immature zone (orange), mature zone (blue), and overmature zone (grey). $R_I$, $R_O$, and $R_M$ refer to immature, mature, and overmature cores, respectively.

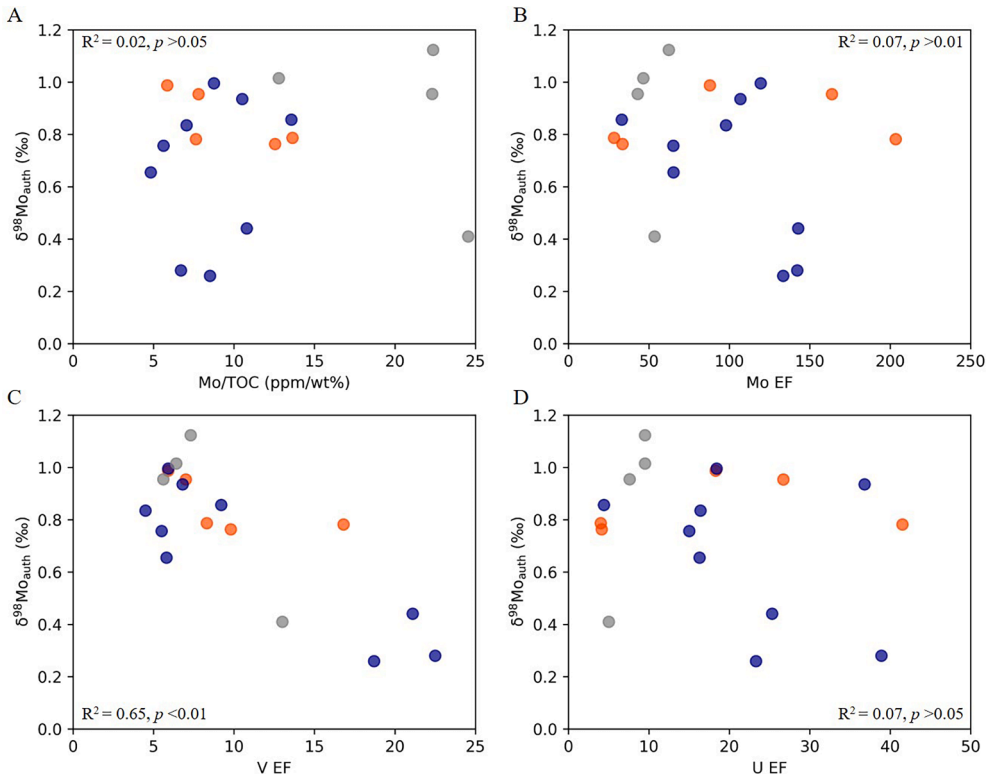


**Fig. 11.** Geochemical diagrams showing the correlations of (A) $\delta^{98}Mo_{auth}$ versus Mo/TOC ratio, (B) $\delta^{98}Mo_{auth}$ versus Mo EF, (C) $\delta^{98}Mo_{auth}$ versus V EF, and (D) $\delta^{98}Mo_{auth}$ versus U EF for the Exshaw Formation black shales. Orange circles refer to immature samples; blue circles refer to mature samples; grey circles refer to overmature samples.

(Helz et al., 1996, 2011; Morford and Emerson, 1999; Erickson and Helz, 2000; Dahl et al., 2013, 2017). The removal rate of Mo in euxinic environments is much higher than in non-euxinic settings (Bertine and Turekian, 1973; Emerson and Huested, 1991; Scott et al., 2008). The Exshaw samples chosen for Mo isotope analysis are characterized by some combination of elevated trace metal enrichments (Mo > 40 ppm, U > 10 ppm), $DOP_T$ values, and $Fe_{HR}/Fe_T$ and $Fe_{py}/Fe_{HR}$ ratios, as these are the samples most likely to reflect euxinic environment. The authigenic Mo isotope compositions ($\delta^{98}Mo_{auth}$) of these Mo-rich Exshaw shales are low (0.26–1.12‰, averaging 0.77 ± 0.52‰, 2SD, n = 18) compared to the modern global seawater Mo isotope composition ($\delta^{98}Mo$ = 2.34 ± 0.10‰; Barling et al., 2001; Siebert et al., 2003; Nakagawa et al., 2012; Nägler et al., 2014). The range of $\delta^{98}Mo$ in the Exshaw Formation is similar to the range observed for the Hangenberg Black Shales in Thuringia and Rhenish Massif (0.2–1.2‰), slightly lower than black shales in the Holy Cross Mountains (1.0–1.5‰), and significantly lower than the high end of the range observed for the Carnic Alps (0.8–2.2‰), suggesting a range of Mo isotopic offsets between the sediments and seawater for both the Exshaw Formation and Hangenberg black shales (Pisarzowska et al., 2020).

As isotopically lighter Mo isotopes are always preferentially removed into sediments during deposition (Barling et al., 2001; Barling and Anbar, 2004; Arnold et al., 2004; Siebert et al., 2006; Neubert et al., 2008) and there was a relatively good connection between the local basin and the open ocean, the highest $\delta^{98}Mo$ of the Exshaw Formation is most likely to capture the coeval seawater $\delta^{98}Mo$ or at least represent the smallest Mo isotope offset from coeval seawater. The highest $\delta^{98}Mo$ of 1.12‰ occurs in a sample (at 3568.23 m from $O_F$) with high $Fe_{HR}/Fe_T$ (0.53) and $Fe_{py}/Fe_{HR}$ (0.77) ratios, high Mo/U EF ratio, and relatively higher Mo (52 ppm) and U (15 ppm) but lower V concentrations (431 ppm, i.e., not hyper-enriched compared to samples with V > 500 ppm). Given that the basin was at most moderately restricted during deposition, iron speciation data and trace metal concentrations for this sample suggest that the bottom water was euxinic and the effects of an Fe-Mn particulate shuttle were relatively limited. Thus, the $\delta^{98}Mo$ of this sample likely comes closest to the coeval seawater $\delta^{98}Mo$.

When deducing coeval seawater $\delta^{98}Mo$, the Mo isotope offsets between euxinic sediments and seawater must be considered because different Mo isotope offsets are observed in modern euxinic settings (e.g., locally strongly versus weakly euxinic water columns; Arnold et al., 2004; Neubert et al., 2008; Nägler et al., 2011; Rolison et al., 2017; Bura-Nakić et al., 2018; Brüske et al., 2020). Bura-Nakić et al. (2018) observed a Mo isotope offset of 0.3‰ between local dissolved Mo and particulate Mo, even for near-quantitative removal of Mo to sediments under strongly euxinic bottom waters (aqueous $H_2S$ > 11 μM). By contrast, weakly euxinic bottom water conditions could cause a large and variable local Mo isotope offset between seawater and sediments, and there are no geochemical techniques to differentiate strongly versus weakly euxinic waters (Arnold et al., 2004; Neubert et al., 2008; Nägler et al., 2011). Deep-water sediments from the modern weakly euxinic Cariaco Basin have a $\delta^{98}Mo$ offset of 0.1–0.8‰ from the open ocean seawater (Arnold et al., 2004; Brüske et al., 2020). Applying the Mo isotope fractionation factor of 0.3‰ (strongly euxinic) and 0.8‰ (weakly euxinic) to the highest $\delta^{98}Mo$ of the Exshaw Formation (1.12‰), the coeval seawater $\delta^{98}Mo$ is estimated to be 1.4–1.9‰.

There are conspicuously low $\delta^{98}Mo$ values for samples at 2060.08 m (0.44‰) and 2060.37 m (0.28‰) in core $M_C$, 2007.35 m (0.26‰) in core $M_D$, and 3565.67 m (0.41‰) in core $O_F$ despite relatively high Mo concentrations (68.3 ppm, 129.3 ppm, 133.4 ppm, and 46.9 ppm, respectively) and elevated $Fe_{HR}/Fe_T$ (0.46, 0.36, 0.44, and 0.35, respectively) and $Fe_{py}/Fe_{HR}$ (0.87, 0.92, 0.90, and 0.65, respectively) ratios. If the deduced coeval seawater $\delta^{98}Mo$ of 1.4–1.9‰ is correct, a large Mo isotope offset between the local sediments and water columns occurred during the deposition of these samples. Alternatively, the low $\delta^{98}Mo$ of these samples could reflect a decrease in $\delta^{98}Mo$ of global seawater. However, this is not likely the only driver because seawater

$\delta^{98}$Mo should not be lower than plausible riverine input $\delta^{98}$Mo (see Table 4S). The low $\delta^{98}$Mo and high V concentrations (720–1460 ppm, EF > 10) of these samples may reflect the operation of an Fe-Mn particulate shuttle (Herrmann et al., 2012; Kendall et al., 2015; Ostrander et al., 2019; Kunert et al., 2020; Lu et al., 2020). There could also be an impact by the Fe-Mn shuttle on samples with intermediate $\delta^{98}$Mo (0.5–1.0‰) and high V concentrations (>500 ppm). For the samples with V concentrations <500 ppm, the effects of an Fe-Mn particulate shuttle on their Mo isotope compositions were likely less pronounced.

In summary, the potential change of global seawater $\delta^{98}$Mo during Exshaw Formation deposition cannot be robustly inferred due to the strong effect of dissolved $H_2S$ (larger seawater-sediment isotopic offsets for weakly euxinic conditions) and the impact of an Fe-Mn particulate shuttle on sedimentary $\delta^{98}$Mo. Nevertheless, based on the discussion above, the contemporaneous global seawater Mo isotope composition is estimated to be 1.4–1.9‰, which is consistent with other studies that suggested seawater $\delta^{98}$Mo values of ~1.5‰ to 2.0‰ during the Late Devonian (Dahl et al., 2010; Magnall et al., 2018; Kendall et al., 2020). The inferred global seawater $\delta^{98}$Mo at the DCB from the Exshaw Formation is lower than the modern ocean $\delta^{98}$Mo, suggesting a greater extent of ocean euxinia than today.

#### 5.3.2. U isotopes

Understanding of the U isotope system as a tracer of global ocean redox conditions has improved over the past decade (see Andersen et al., 2017; Zhang et al., 2020b for a review). Similar to Mo, the main source of U to the oceans is rivers (Dunk et al., 2002). Groundwaters may also supply U, but the input flux is not well understood. The average $\delta^{238}$U of oxygenated modern seawater is −0.39 ± 0.04‰ (2SD; Weyer et al., 2008; Tissot and Dauphas, 2015; Andersen et al., 2016; Noordmann et al., 2016). The weighted average $\delta^{238}$U of rivers has been estimated between −0.34‰ and −0.24‰, which is similar to the upper continental crust (−0.3‰; Stirling et al., 2007; Weyer et al., 2008; Tissot and Dauphas, 2015; Andersen et al., 2016; Noordmann et al., 2016).

Large effective U isotope offsets between the local water column and sediments (0.6 ± 0.2‰) occur in many modern euxinic basins and result in the preferential removal of $^{238}$U to sediments to an extent that depends on local environmental factors like sedimentation rates, sulfate reduction rates, and degree of basin restriction (Weyer et al., 2008; Andersen et al., 2014; Noordmann et al., 2015; Holmden et al., 2015; Rolison et al., 2017; Bura-Nakić et al., 2018; Brüske et al., 2020; Lau et al., 2020). The full range of U isotope offsets can be larger based on *ab initio* molecular orbital modeling (0.95‰; Abe et al., 2008) and laboratory experimental studies (~1.0–1.2‰; Basu et al., 2014; Stirling et al., 2015; Stylo et al., 2015; Brown et al., 2018). In euxinic settings, U diffusion and reduction below the sediment–water interface causes the effective isotope fractionation to be half of the maximum isotope fractionation (similar to Se; Clark and Johnson, 2008; Andersen et al., 2014) whereas non-diffusion-limited removal of U in the water column or to organic floccule layers at the sediment–water interface, with low-to-intermediate rates of U reduction and sedimentary enrichment in temporally dynamic (with respect to redox) and weakly euxinic environments, may be associated with larger U isotope offsets (Andersen et al., 2020; Cheng et al., 2020; Lau et al., 2020; Clarkson et al., 2023). Smaller U isotope offsets are generally found in other modern marine sediments (e.g., ferruginous, suboxic, Fe-Mn oxides in oxic sediments) (Stirling et al., 2007; Weyer et al., 2008; Brennecka et al., 2011; Romaniello et al., 2013; Goto et al., 2014; Tissot and Dauphas, 2015; Andersen et al., 2016; Noordmann et al., 2015, 2016; Wang et al., 2016; Chen et al., 2016, 2018; Tissot et al., 2018; Cole et al., 2020; He et al., 2021; Bruggmann et al., 2022). However, Namibian continental margin sediments and Miocene sediments in the Santa Barbara Basin deposited under non-euxinic conditions span a range of $\delta^{238}$U and the U isotope fractionation relative to seawater is similar to that of modern euxinic settings (Abshire et al., 2020; Lau et al., 2022). In addition, a fractionation factor of 0.6 ± 0.1‰ was proposed between black shales and seawater under constant euxinic conditions in non-restricted basins based on $\delta^{238}$U values from the Livello Bonarelli black shales deposited around the Cenomanian-Turonian boundary (Gangl et al., 2023). The operation of an Fe-Mn particulate shuttle has less effect on sedimentary $\delta^{238}$U compared to $\delta^{98}$Mo due to the weaker affinity of U for Fe-Mn oxyhydroxides.

Two different correlation patterns between $\delta^{238}$U and U EF are observed for the Exshaw Formation (Fig. 12). The first pattern exhibits a positive correlation between $\delta^{238}$U (−0.23‰ to 0.23‰) and U EF (2 to 42) (denoted as $U_1$ group; $R^2 = 0.54$, $p < 0.01$), which may be related to changes in the degree of basin restrictions (reservoir effect) or local bottom water redox conditions (Weyer et al., 2008; Andersen et al., 2017; Bura-Nakić et al., 2018; Lau et al., 2020). The lack of relationship between the degree of basin restriction indicator (Sr/Ba ratios) and $\delta^{238}$U for these samples ($R^2 = 0.00$, $p > 0.05$; Fig. 13) suggests the positive correlation between $\delta^{238}$U and U EF most likely results from variable local redox conditions. More intense bottom water euxinia likely led to higher U enrichments and $\delta^{238}$U. These samples ($U_1$ group) are from the immature and mature lower Exshaw intervals, as well as the whole overmature core. The other samples (denoted as $U_2$ group) have higher $\delta^{238}$U and show no significant correlation ($R^2 = 0.06$, $p > 0.05$) between $\delta^{238}$U (0.23‰ to 0.39‰) and U EF (2 to 8). These samples are mostly from the immature and mature higher Exshaw intervals, except one sample from the overmature core. Similarly, $\delta^{238}$U and Mo EF, $\delta^{238}$U and Re EF, and $\delta^{238}$U and V EF exhibit the same trends as $\delta^{238}$U and U EF (Fig. 12).

The $U_1$ group can be further divided into two subgroups based on local redox conditions. Four overmature samples with low Mo enrichments (<12 ppm, EF < 15), low U enrichments (<6 ppm, EF < 5), low $DOP_T$ values (0.29–0.51), and low Mo/U EF ratios (≤1 time the modern $[Mo/U]_{SW}$) were likely deposited under oxic to suboxic conditions ($U_{1a}$ group). These samples have an average $\delta^{238}U_{auth}$ of −0.14 ± 0.10‰ (1SD, n = 4; −0.23‰ to 0.01‰). The other samples with high Mo enrichments (>44 ppm, EF > 45), high U enrichments (>8 ppm, EF > 5), and high Mo/U EF ratios (>1 time the modern $[Mo/U]_{SW}$), relatively high $DOP_T$ values (0.46–1.11), and relatively high $Fe_{HR}/Fe_T$ (>0.27) and $Fe_{py}/Fe_{HR}$ (>0.65) ratios were most likely deposited under euxinic conditions ($U_{1b}$ group). These samples have an average of $\delta^{238}U_{auth}$ of 0.01 ± 0.11‰ (1SD, n = 14, −0.13‰ to 0.23‰).

The coeval seawater U isotope compositions can be deduced from the samples with a positive correlation between $\delta^{238}$U and U EF ($U_1$ group). A large and variable U isotope fractionation factor may occur under hypoxic conditions (Andersen et al., 2016; Dang et al., 2018; Abshire et al., 2020). Here, we tentatively apply a U isotope offset of 0.15‰ to 0.60‰ (based on the fractionation factors in modern oxic to suboxic basins; e.g., Dang et al., 2018; Abshire et al., 2020) to $U_{1a}$ subgroup samples (average $\delta^{238}U_{auth}$ = −0.14 ± 0.10‰, U EF: 2–5) and thus the coeval seawater $\delta^{238}$U may have been between −0.74‰ (=−0.14‰ to 0.60‰) and −0.29‰ (=−0.14‰ to 0.15‰). Applying an isotopic offset of 0.4‰ to 0.8‰ (~0.6 ± 0.2‰ from modern euxinic basins; e.g., Andersen et al., 2016; Brüske et al., 2020) to the $U_{1b}$ subgroup (average $\delta^{238}U_{auth}$ = 0.01 ± 0.11‰, U EF: 5–42) yields coeval seawater $\delta^{238}$U estimates of −0.79‰ (=0.01‰–0.80‰) to −0.39‰ (=0.01‰–0.40‰). The estimated seawater $\delta^{238}$U from the $U_1$ subgroup approaches the seawater $\delta^{238}$U of riverine inputs and the upper continental crust. However, the $\delta^{238}$U of global seawater inferred from carbonates from the DCB Long'an section in China remained below −0.5‰ at the DCB (Zhang et al., 2020a), which is similar to the lower estimates of seawater $\delta^{238}$U from the $U_1$ subgroup samples.

Deducing the coeval seawater $\delta^{238}$U from the $U_2$ group (no correlation between $\delta^{238}$U and U EF) is less straightforward. These samples have relatively higher $\delta^{238}$U (0.23–0.39‰, ave. = 0.32 ± 0.05‰, 1SD, n = 8). Four samples from the $U_2$ group have moderate Mo enrichments (44–63 ppm, EF > 28), high V enrichments (>500 ppm), relatively high Mo/U EF ratios (>1 time the modern $[Mo/U]_{SW}$), $DOP_T$ values (0.53–0.81), and high $Fe_{HR}/Fe_T$ (>0.39) and $Fe_{py}/Fe_{HR}$ (>0.71) ratios,

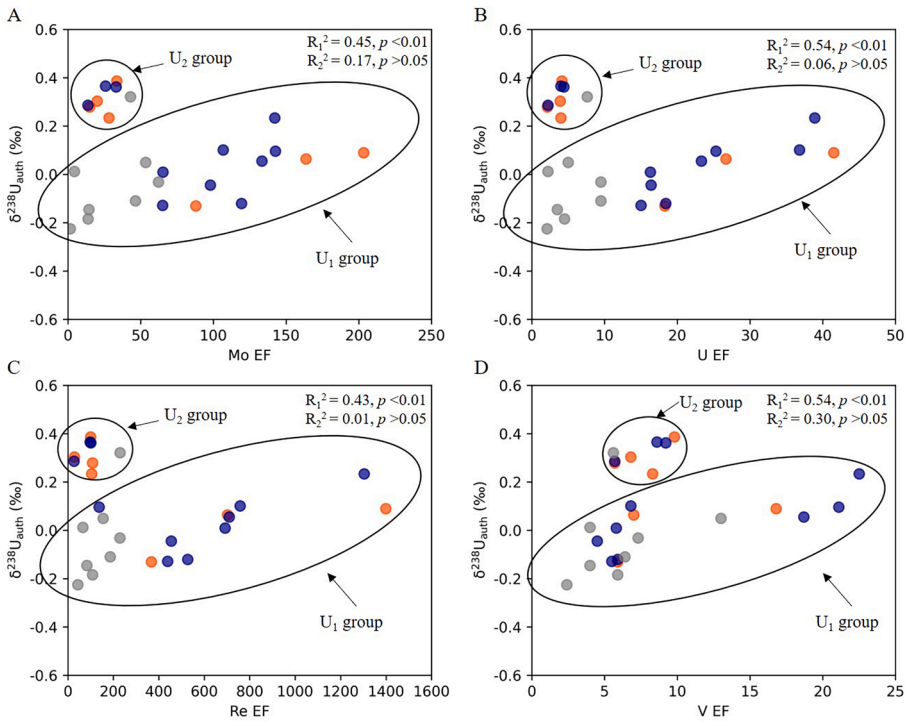


**Fig. 12.** Geochemical diagrams showing the correlations of (A) $\delta^{238}U_{auth}$ versus Mo EF, (B) $\delta^{238}U_{auth}$ versus U EF, (C) $\delta^{238}U_{auth}$ versus Re EF, and (D) $\delta^{238}U_{auth}$ versus V EF for the Exshaw Formation black shales. Orange circles refer to immature samples; blue circles refer to mature samples; grey circles refer to overmature samples. $R_1$ and $R_2$ refer to $U_1$ group and $U_2$ group, respectively.

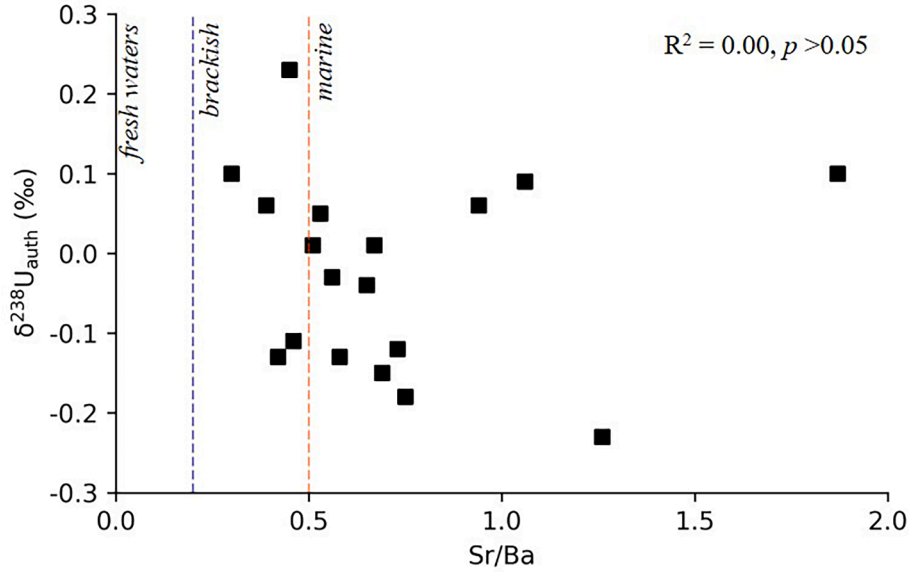


**Fig. 13.** Crossplots of authigenic $\delta^{238}U$ versus Sr/Ba for the $U_1$ group (Wei and Algeo, 2020). The blue and yellow dashed line refers to Sr/Ba ratios of 0.2 and 0.5, respectively, as inferred from Wei and Algeo (2020).

suggesting euxinic bottom water conditions. Although the other four samples lack Fe speciation data, they are characterized by relatively lower Mo enrichments (20–36 ppm, EF > 15) but similar levels of high V enrichment, high $DOP_T$ values, and high Mo/U EF ratios as the four euxinic samples, suggesting locally anoxic and possibly euxinic bottom water conditions. The higher $\delta^{238}U$ of the $U_2$ group suggests a larger U isotopic offset between these samples and coeval seawater. Applying a ~0.6‰ offset to the average $\delta^{238}U$ of 0.32 ± 0.05‰ for the $U_2$ group yields an unrealistic seawater $\delta^{238}U$ of −0.28 ± 0.05‰, which is less negative than modern seawater and would imply a more oxygenated ocean with less euxinia during the Late Devonian compared to the modern ocean. A study on a Holocene Mediterranean sapropel proposed that high productivity may promote U reduction and removal to an organic floccule layer at the sediment–water interface, leading to a large U isotope offset of up to ~1‰ (Andersen et al., 2020), in contrast to smaller U isotope offsets for sediments from modern upwelling continental margin settings and euxinic basins (e.g., Weyer et al., 2008; Bura-Nakić et al., 2018; Abshire et al., 2020; Brüske et al., 2020; Cole et al., 2020; He et al., 2021; Bruggmann et al., 2022). By contrast, a recent study reported that high U isotope offsets can result from limited

sedimentary U reduction in weakly euxinic settings or temporally dynamic reducing environments which have lower to moderate organic carbon and uranium accumulation rates (Clarkson et al., 2023). High rates of primary productivity and organic carbon burial may suppress the U isotopic offset between sediments and seawater owing to the greater efficiency of U burial, as shown by reactive transport modeling, unless other factors like U removal in the water column (as opposed to within sediments) are important (Lau et al., 2020). Although the effects of high productivity on sedimentary $\delta^{238}U$ remain debated, unusually large U isotope offsets (>0.8‰; up to the full expression of non-diffusion-limited U isotope fractionation of ~1.2‰) between black shales and coeval global seawater have been suggested for Member 4 of the Upper Ediacaran Doushantuo Formation (Kendall et al., 2015), the Lower Cambrian Niutitang Formation (Cheng et al., 2020), and the Upper Devonian Kettle Point Formation (Kendall et al., 2020). For the average $\delta^{238}U_{auth}$ of 0.32 ± 0.05‰ of the $U_2$ group and assuming an isotopic offset of 0.8–1.2‰, the estimated seawater $\delta^{238}U$ is between −0.88‰ (=0.32‰ − 1.20‰) to −0.48‰ (=0.32‰ − 0.80‰), which significantly overlaps the seawater $\delta^{238}U$ estimates derived from the $U_1$ group.

In summary, the estimated upper boundary of seawater $\delta^{238}U$ inferred from the Exshaw Formation and the Long'an section of South China probably is ~−0.5‰, and the lower boundary of seawater $\delta^{238}U$ is suggested to be −0.8‰ (from $U_1$ group) or −0.9‰ (from $U_2$ group), suggesting a larger extent of ocean euxinia at the end of the Devonian than today. Therefore, both $\delta^{98}Mo$ and $\delta^{238}U$ data from the Exshaw Formation, together with the $\delta^{238}U$ data from the Long'an section carbonates (Zhang et al., 2020a), collectively point to expanded ocean euxinia during the Hangenberg Crisis.

#### 5.3.3. Implications for the coupled use of Mo-U isotopes as a global ocean redox proxy

The covariations of $\delta^{238}U$ and $\delta^{98}Mo$ in black shales can reflect the relative influence of the local depositional environment versus changes in global ocean redox conditions (Asael et al., 2013; Kendall et al., 2015; Bura-Nakić et al., 2018; Andersen et al., 2020; Brüske et al., 2020; Kendall et al., 2020; Lu et al., 2020; Stockey et al., 2020; Dahl et al., 2021; Pan et al., 2021; Chiu et al., 2022; Li et al., 2022b; Zhao et al., 2023). A lack of correlation between $\delta^{238}U$ and $\delta^{98}Mo$ suggests the combination of both local and global changes or only changes in the local depositional environment that have distinctive impacts on Mo and U isotope signatures in sediments. No clear covariation between $\delta^{238}U$ and $\delta^{98}Mo$ is observed in the Exshaw Formation ($R^2 = 0.05$, $p > 0.05$; Fig. 5).

We suggest the large range of $\delta^{238}U$ (−0.23‰ to 0.39‰) and $\delta^{98}Mo$ (0.26‰ to 1.12‰) but lack of correlation between the isotope systems for the Exshaw Formation is a consequence of distinctive local depositional controls for Mo and U transfer to the sediments. The particulate shuttle, for example, has a significantly greater impact on Mo than U. The efficiency of Mo adsorption to Mn oxides and the magnitude of Mo isotope fractionation associated with this process are both greater than for U (Algeo and Tribovillard, 2009; Noordmann et al., 2015; Bura-Nakić et al., 2018; Lu et al., 2020). Variations in the extent of Fe-Mn particulate shuttling and bottom water sulfide concentrations can influence the Mo isotopic offset between seawater and sediments (see Section 5.3.1). Although U isotope fractionation is also affected by sulfide concentrations (Brüske et al., 2020), other factors controlling U removal exert a significant control on the $\delta^{238}U$ of sediments, with large U isotope fractionations occurring upon non-diffusion-limited U removal (e.g., in the water column or in an organic floccule layer at the sediment–water interface in dynamic or weakly euxinic environments) and smaller U isotope fractionations for diffusion-limited U removal in more persistently euxinic settings (Andersen et al., 2020; Cheng et al., 2020; Lau et al., 2020; Clarkson et al., 2023; Gangl et al., 2023). In contrast to Mo, the magnitude of U isotope fractionation and efficiency of U removal for the non-diffusion-limited and diffusion-limited scenarios are greater than for U adsorption to Mn-oxides, effectively decoupling the two isotope systems when all these processes are operating during deposition of a black shale formation. Consequently, estimates of the seawater isotope $\delta^{238}U$ and $\delta^{98}Mo$ must be made independently.

To alleviate the shortcomings of each approach, Mo-U isotope data from black shales and U isotope data from carbonates can be used together to infer global ocean redox conditions. The large uncertainty in the estimates for seawater $\delta^{238}U$ and $\delta^{98}Mo$ derived from the Exshaw Formation black shales makes it difficult to determine whether there was a change in global ocean redox conditions exclusive to the Hangenberg Crisis. We note, for example, that our seawater $\delta^{98}Mo$ estimates for the Hangenberg Crisis (1.4–1.9‰) overlaps with estimates of $\delta^{98}Mo$ for older Famennian seawater (1.5–2.0‰). The carbonate U isotope paleoredox proxy has an advantage in tracking changes in global ocean redox conditions because of generally smaller seawater-sediment U isotope fractionations (Zhang et al., 2020b) yet there are also risks, stemming from changes in the local depositional environment, with inferring global ocean redox changes at a single locality using carbonate U isotope data (e.g., Lu et al., 2023). Despite the complexity of the Exshaw black shale Mo-U isotope datasets, we can independently confirm that there was expanded ocean euxinia during the Hangenberg Crisis, as inferred from stratigraphic changes in carbonate U isotope data from the Long'an section (Zhang et al., 2020a) and mass-balance modelling of Mo enrichments in the Bakken Shale (Sahoo et al., 2023).

### 5.4. Quantitative constraints on the extent of Devonian-Carboniferous ocean anoxia from a U and Mo isotope mass balance model

To quantitatively estimate the extent of marine redox variations, a mass balance model that integrates the Mo and U isotope compositions with Monte Carlo simulations is used (following Stockey et al., 2020). The details are summarized as follows.

The metal concentrations (Me, in this case: Mo and U) and their seawater isotope compositions ($\delta^n Me_{sw}$, n = 98 for Mo, n = 238 for U) are described by Eqs. (1)–(2), where F represents flux; riv is riverine input; oxic stands for oxic settings (Fe-Mn oxides); red stands for sediments deposited under non-euxinic conditions with sulfidic porewaters; eux refers to euxinic environments; Δ refers to the isotopic offset between seawater and each sink.

$$\frac{d[Me]_{sw}}{dt} = F_{riv} - F_{oxic} - F_{red} - F_{eux} \quad (1)$$

$$\frac{d[Me]_{sw}\delta^n Me_{sw}}{dt} = F_{riv}\delta^n Me_{riv} - F_{oxic}(\delta^n Me_{sw} + \Delta^n Me_{oxic}) - F_{red}(\delta^n Me_{sw} + \Delta^n Me_{red}) - F_{eux}(\delta^n Me_{sw} + \Delta^n Me_{eux}) \quad (2)$$

Fluxes for the metal sinks are defined as the relationship among per area burial flux ($b_i$), the seafloor area of the metal sink ($A_i$), a pseudo-spatial scaling coefficient relating burial rate to the area of the sink ($\alpha_i$), the mean modeled oceanic metal concentration ($[Me]_{sw}$), and the mean oceanic metal concentration in modern seawater ($[Me]_{M.sw}$) (Eq. (3)).

$$F_i = b_i A_i \alpha_i \frac{[Me]_{sw}}{[Me]_{M.sw}} \quad (3)$$

The area of the metal sink for a specific redox state is represented as:

$$A_i = A f_i \quad (4)$$

where A is the total seafloor area in the modern ocean, and $f_i$ is the proportion of the global seafloor that covers a specific redox condition (oxic, red, eux).

In the Monte Carlo simulations, the proportion of euxinic seafloor area ($f_{eux}$) is modelled in 31 equally spaced, logarithmically scaled steps, with 1000-time simulations per $f_{eux}$ scenario. The areal extent of the

metal reducing sink ($f_{red}$) is involved in the sensitivity analysis and varies between 0% and (100 - $f_{eux}$)%. The range of the maximum extent of oxic deposition ($f_{ox.lim}$) is presented in Table 4S based on Reinhard et al. (2013) and physical oceanographic limits.

$$f_{oxic} = f_{ox.lim} - f_{eux} - f_{red} \quad (5)$$

A pseudospatial burial coefficient (α) is introduced to the model, such that metal burial in the sinks is scaled to the anticipated effects of organic carbon remineralization, depending on the extent of euxinic and reducing conditions across the continental shelf (Middelburg et al., 1996; Reinhard et al., 2013). Burial rate in oxic settings is assumed to be scaled linearly ($\alpha_{ox} = 1$) and independent of organic carbon remineralization.

Burial rates in euxinic settings scale with the expansion of euxinia, following the remineralization model in Reinhard et al. (2013). Therefore, this scaling algorithm is defined as:

$$\alpha_{eux} = \frac{\sum_{min(z_{eux})}^{max(z_{eux})} 1.58 - 0.16\ln(z_{eux})}{N(z_{eux})\{1.58 - 0.16\ln(\min(z_{eux}))\}} \quad (6)$$

where $N(z_{eux})$ represents the number of depths modeled following Menard and Smith (1966) and Reinhard et al. (2013) and z refers to water depth.

Burial rates of reducing settings could change and scale with the extent of euxinic and reducing conditions. Following previous application of Menard and Smith (1966) to the metal mass balances, red (non-euxinic; sulfidic pore waters) settings are modeled as expanding below euxinic depositional environments along continental shelves in the pseudospatial scaling algorithm.

$$\alpha_{red} = \frac{\sum_{min(z_{red})}^{max(z_{red})} 1.58 - 0.16\ln(z_{red} + \max\ln(z_{eux}))}{N(z_{red})\{1.58 - 0.16\ln(\min(z_{eux}))\}} \quad (7)$$

where $N(z_{red})$ describes the number of depths modeled, $\min(z_{red})$ is defined as $\max(z_{eux})$, and $\max(z_{red})$ is a function of $A_{red} + A_{eux}$, defined following Menard and Smith (1966).

The mass balance model was established to generate frequency distributions of feasible synthetic sedimentary Mo-U isotope values with respect to different paleoredox environments, using the following Eqs. (8)–(10) for calculating euxinic shale and carbonate values with local fractionation factors:

$$\delta^{98}Mo_{eux} = \delta^{98}Mo_{sw} + \Delta^{98}Mo_{eux.loc} \quad (8)$$

$$\delta^{238}U_{eux} = \delta^{238}U_{sw} + \Delta^{238}U_{eux.loc} \quad (9)$$

$$\delta^{238}U_{carb} = \delta^{238}U_{sw} + \Delta^{238}U_{carb.loc} \quad (10)$$

A variable coefficient ordinary differential equation solver was used to fully couple marine trace metal (Mo, U) concentrations and isotope values ($\delta^{98}$Mo, $\delta^{238}$U) in mass balance equations instead of the conventional assumption of instantaneous steady-state. Relevant values for Monte Carlo variables are listed in Table 4S. Fixed model parameters are listed in Table 5S.

The Mo and U isotope data from the Exshaw Formation in this study as well as carbonate U isotope data from the Yonghsien and Long'an formations (China) from Zhang et al. (2020a) are integrated and applied in this mass balance model to quantitatively estimate global ocean euxinia at the DCB. Four samples with exceptionally low $\delta^{98}Mo_{auth}$ (<0.5‰, below the riverine input) that were likely affected by a local Fe-Mn particulate shuttle were not used. The Mo isotope values of 0.66‰ to 1.12‰ with local fractionation factors of −0.8‰ to −0.3‰ are applied in this model (Table 6S). The two euxinic U isotope groups ($U_{1b}$, $U_2$) were modelled with different local fractionation factors (0.4–0.8‰, 0.8–1.2‰, respectively) to account for the potential influence of organic floccule layers on the $\delta^{238}$U of $U_2$ samples (Table 6S). Carbonate $\delta^{238}$U from Zhang et al. (2020a) ranges from −0.82‰ to 0.32‰, with local fractionation factors of 0.2–0.6‰ (Table 6S). As Eqs. (8)–(10) show, the coeval seawater $\delta^{238}U_{sw}$ and $\delta^{98}Mo_{sw}$ can be obtained based on the local $\delta^{238}U_{auth}$, $\delta^{238}U_{carb}$, and $\delta^{98}Mo_{auth}$ as well as their fractionation factors. The model can utilize these values to calculate the fraction of seafloor euxinia at the DCB. The Mo and U mass balance model results are shown as frequency distributions of predicted euxinic shale $\delta^{98}$Mo and $\delta^{238}$U values, corresponding to a range of logarithmically scaled scenarios for global marine euxinia (Fig. 14). The fraction of euxinia is estimated from both single proxy and combined proxies (Table 6S). Specifically, the Exshaw Formation $U_{1b}$ group yields a $f_{eux}$ mean of 10.2% (median: 1.3%; 5th percentile = 0.1%; 95th percentile = 63.1%) and the $U_2$ group yields a $f_{eux}$ mean of 15.6% (median: 4.0%, 5th percentile = 0.2%; 95th percentile = 74.9%). Molybdenum isotope data from the Exshaw Formation yields a $f_{eux}$ mean of 22.3% (median: 10.0%; 5th percentile = 0.3%; 95th percentile = 79.4%). Carbonate U isotope data from the Yonghsien and Long'an formations yield a $f_{eux}$ mean of 15.6% (median: 3.2%; 5th percentile = 0.1%; 95th percentile = 79.4%). The combined use of Mo isotopes and different U isotope groups from the Exshaw Formation yield 18.2–21.3% for the average $f_{eux}$ and 6.3–10% for the median $f_{eux}$ (5th percentile < 1%, 95th percentile = 79.4%). The combined use of Mo isotopes and different U isotope groups from the Exshaw Formation as well as carbonate U isotope data from the Long'an section yield the same average $f_{eux}$ and median $f_{eux}$ during the Hangenberg Crisis (Table 6S). Although there is a large distribution (5th percentile < 1%, 95th percentile = 79.4%), the modelled median/mean results of multi-proxies (6.3–21.3%) better represent the extent of ocean euxinia during the Hangenberg Crisis than one single proxy. Considering the extreme values cause the large uncertainties and significantly influence the mean, the median probabaly is better to reflect the extent of ocean euxinia rather than the mean. The estimated median $f_{eux}$ of 6–10% is thus our best estimate for the extent of ocean euxinia during the Hangenberg Crisis.

### 5.5. *Implications of coupling geochemical proxies for inferring the triggers of the Hangenberg Crisis*

Our Mo-U isotope data from the Exshaw Formation together with the carbonate $\delta^{238}$U data from Zhang et al. (2020a) constitute evidence for global ocean euxinia over an area of seafloor that was at least two orders of magnitude greater at the DCB compared with today. Expanded ocean anoxia/euxinia during the Hangenberg Crisis is supported by several local- and regional-scale geochemical proxies, such as low carbonate $\delta^{15}$N (Liu et al., 2016), low I/Ca ratios (Liu et al., 2019), Mo enrichments, Fe speciation, and N and S isotope data (Sahoo et al., 2023), and positive and negative $\delta^{13}C_{carb}$ excursions in pantropically widespread black shales (including the Exshaw Formation) around the DCB (Caplan and Bustin, 1998; Kaiser et al., 2006, 2016; Cramer et al., 2008; Kumpan et al., 2013, 2019; Qie et al., 2015; Kaiser et al., 2016; Pisarzowska et al., 2020; Stolfus et al., 2020; Ferri et al., 2021; Heath et al, 2021). A recent study reported that local bottom water redox conditions of the Exshaw Formation from the Jura Creek type section switched from euxinic to ferruginous during the Hangenberg Crisis, as evidenced by Fe speciation and a stratigraphic trend of decreasing trace metal enrichments (i.e., Mo, U, Re) (Li et al., 2022a). In comparison, the Exshaw black shales in the Peace River area exhibited a similar decreasing trend in Mo, U, and Re concentrations from stratigraphically lower to higher intervals (especially for the $I_B$, $M_C$, $M_D$, and $O_F$ cores). We interpret that the local redox conditions changed from more intensely euxinic to suboxic–weakly euxinic based on trace metal concentrations/ratios and Fe speciation. Such decreasing trends in trace metal enrichments point to a better ventilation of local bottom waters; similar findings were reported from several basins in North America and Europe (e.g., Scott et al., 2017; di Pasquo et al., 2019; Browne et al, 2020; Pisarzowska et al., 2020; Li et al., 2022a). Therefore, the local bottom water redox conditions during the Hangenberg Crisis may be not consistently anoxic/euxinic, but instead show some fluctuations and trended generally towards less

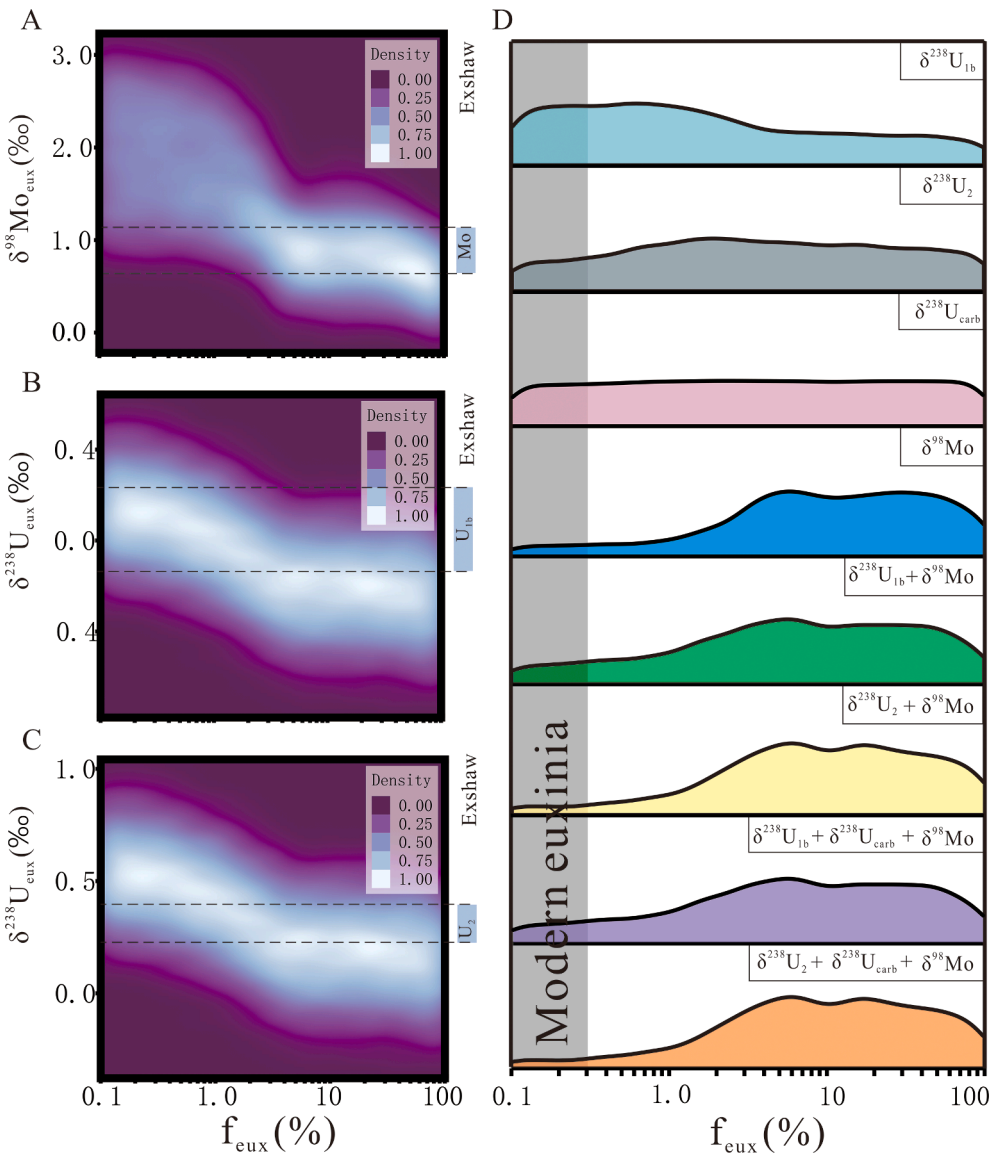


**Fig. 14.** Estimates of seafloor euxinia ($f_{eux}$) at the DCB boundary from Monte Carlo simulations (following Stockey et al. 2020) based on (A) Exshaw Mo isotope data, (B) Exshaw $U_{1b}$ isotope data, and (C) Exshaw $U_2$ isotope data. (D) A panel of frequency distributions for different scenarios associated with Exshaw data ($\delta^{238}U_{1b}$, $\delta^{238}U_2$, $\delta^{98}Mo$), carbonate data ($\delta^{238}U_{carb}$; Zhang et al., 2020a), and combined data ($\delta^{238}U_{1b}$ + $\delta^{98}Mo$, $\delta^{238}U_2$ + $\delta^{98}Mo$, $\delta^{238}U_{1b}$ + $\delta^{238}U_{carb}$ + $\delta^{98}Mo$, $\delta^{238}U_2$ + $\delta^{238}U_{carb}$ + $\delta^{98}Mo$), respectively (from top to bottom).

reducing conditions.

As the lower black shale member of the Exshaw Formation and coevally widespread black shales elsewhere were deposited during transgression, the expanded global euxinic seafloor area (~6–10%) likely covered a majority of the continental shelves (except the shallowest oxygenated waters) and epicontinental seas (Caplan and Bustin, 1999; Chen et al., 2013; Formolo et al., 2014; Kaiser et al., 2016), destroying the living habitat of metazoans, and triggering the mass extinction. Sahoo et al. (2023) derive a lower estimate of ~0.5–1.0% (and most likely < 2%) for the global extent of seafloor euxinia using a Mo elemental mass balance model for the Bakken Shale. However, this model does not recognize that the input flux of Mo to the DCB oceans may be different from today. An increase in riverine Mo flux in response to elevated continental weathering during large igneous province events will result in elemental mass balance models potentially underestimating the extent of ocean euxinia (Kendall, 2021; Kunert and Kendall, 2023). Changes to continental weathering fluxes have little impact on Mo and U isotope mass-balance models because plausible igneous sources have similar isotopic compositions (Tissot and Dauphas, 2015; Willbold and Elliott, 2017). The higher estimates for the extent of ocean euxinia from Mo and U isotope data (this study; Zhang et al., 2020a) do support the conclusion by Sahoo et al. (2023) that expansion of euxinia into shallow ocean regions was an important contributor to the Hangenberg Crisis.

Apart from ocean anoxia/euxinia, other kill mechanisms have been proposed for the Hangenberg Crisis. For instance, significant burial of organic carbon, as evidenced by the widespread deposition of black shales, might reduce the atmospheric $CO_2$, resulting in climate cooling and glaciations at the DCB that contributed to the Hangenberg Crisis (Kaiser et al., 2006, 2016; Brezinski et al., 2008; Caputo et al., 2008; Isaacson et al., 2008; Melott et al., 2020). Although frequent sea level fluctuations are suggested at the DCB, it is still under debate if the eustatic change caused the Hangenberg Crisis (Walliser, 1984; Johnson et al., 1985; Qie et al., 2015; Kaiser et al., 2016; Kabanov and Jiang, 2020). Volcanic activity attributed to large igneous province magmatism, as recorded in DCB sections from Asia and Europe (Pracht and Batchelor, 1998; Gonzalez et al., 2006; Filipiak and Racki, 2010; Liu et al., 2012; Marynowski et al., 2012; Paschall et al., 2019; Ernst et al., 2020; Pisarzowska et al., 2020), may have provided further biotic stress and considerably enhanced atmospheric $CO_2$ concentrations. High sedimentary Hg enrichments as well as pyroclastic material are observed within and below Hangenberg black shales in Europe, indicating magmatic activity was a trigger of global environmental and biological changes (Pisarzowska et al., 2020). However, a recent study found no Hg

enrichments in Laurussia at the DCB (Zhao et al. 2022), hence, it is uncertain if there was a volcanic trigger for euxinia at the DCB. In addition, a supernova explosion was proposed to contribute to the Hangenberg Crisis via accelerating cosmic rays that depleted the ozone layer and induced ultraviolet-B damage for thousands of years (Fields et al., 2020).

From the above discussion, the Late Devonian Hangenberg Crisis was probably driven by multiple factors rather than one single killing mechanism. Our geochemical data support expanded ocean euxinia as a significant factor that impacted and maybe even triggered the Hangenberg Crisis. In addition, we have demonstrated that Mo and U isotope data from black shales (this study) paired with carbonate U isotope data (Zhang et al., 2020a) collectively provide more robust information about ancient global ocean paleoredox conditions.

## 6. Conclusions

Geochemical data from the Exshaw Formation black shale member provide important insights into the local depositional environment and global ocean redox conditions at the Devonian-Carboniferous boundary. Hydrocarbon maturation had limited influence on the redox-sensitive trace metals analyzed in this study, based on low pyrite sulfur isotope ratios, large sulfur isotope fractionations between pyrite and original seawater sulfate (pointing to MSR rather than TSR), as well as no statistical difference in isotopic compositions ($\delta^{98}$Mo, $\delta^{238}$U, and $\delta^{34}S_{py}$) among the areas of different hydrocarbon maturity. Thus, the depositional environment of the Exshaw Formation can be reconstructed using these geochemical proxies.

The paleosalinity proxies (Sr/Ba from all shale samples and TS/TOC from immature shales) suggest a brackish to marine environment during Exshaw Formation deposition. Local bottom water redox conditions ranged from suboxic (with sulfidic pore waters) to euxinic based on Mo, U, and Re enrichments and Fe speciation data. Vanadium enrichments do not covary with other RSTMs and could be affected by additional processes (e.g., the operation of an Fe-Mn particulate shuttle; the formation of V-rich clay-organic nanocomposites).

Our study provides the first coupled estimates of seawater Mo and U isotope compositions at the DCB based our data from the Exshaw black shales. The $\delta^{98}$Mo of the Exshaw Formation was likely offset to lower values compared to coeval seawater due to incomplete Mo removal from bottom waters to sediments and the operation of an Fe-Mn particulate shuttle. Both local redox conditions and variations in the mechanism and site of U removal (water column, organic floccule layer at the sediment–water interface, or within sediments) influenced the $\delta^{238}$U of the Exshaw shales. Taking these local depositional factors into consideration, the coeval seawater $\delta^{98}$Mo and $\delta^{238}$U during Exshaw Formation deposition are estimated to be 1.4–1.9‰ and between −0.9‰ and −0.5‰, respectively. Compared with the modern seawater, the lower seawater $\delta^{98}$Mo and $\delta^{238}$U values at the DCB suggest a larger extent of global ocean euxinia. A mass balance model for Mo and U isotopes suggests the extent of euxinic seafloor area (~6–10%, based on the median results) was at least two orders of magnitude greater during the Hangenberg Crisis than today. Therefore, expanded ocean anoxia/euxinia, particularly in intracratonic and continental margin regions, could have significantly contributed to the Hangenberg mass extinction. Our study also highlights how Mo-U isotope data from black shales and U isotope data from carbonates together can provide more robust constraints on global ocean paleoredox conditions.

## Declaration of Competing Interest

The authors declare that they have no known competing financial interests or personal relationships that could have appeared to influence the work reported in this paper.

## Acknowledgements

We thank Liyan Xing and Sarah McCaugherty for technical assistance. This study was supported by a NSERC Discovery Grant (grant number RGPIN-2019-0409), and the Canada Research Chairs Program (BK). The Metal Isotope Geochemistry Laboratory at Waterloo was funded by the Canada Foundation for Innovation, Ontario Research Fund, and University of Waterloo. JDO would like to thank the National Aeronautics and Space Administration (80NSSC18K1532), the Sloan Foundation (FG-2020–13552) for funding the Fe extraction, and a portion of this work was performed at the National High Magnetic Field Laboratory in Tallahassee, Florida, which is supported by the National Science Foundation Cooperative Agreement No. DMR-1644779 and by the State of Florida.

## Appendix A. Supplementary material

The supplementary materials contain the research data, model parameters, and additional figures. Elemental data, DOP values, $C_{org}/P$ ratios, and organic carbon isotope values of the Exshaw Formation are listed in Table S1. Enrichment factors and geochemical ratios are listed in Table S2. The Mo, U, and pyrite S isotope compositions as well as iron speciation data are listed in Table S3. The model parameters are described in Table S4-S5. The data inputs and outputs for the mass balance model are exhibited in Table S6. Additional figures include the relationship between $DOP_T$ and $Fe_{py}/Fe_{HR}$ (Fig. S1) as well as the organic carbon isotope values and TOC contents for the Exshaw Formation in drillcores from the immature zone (Fig. S2), mature zone (Fig. S3) and overmature zone (Fig. S4). Supplementary material to this article can be found online at https://doi.org/10.1016/j.gca.2023.04.027.

## References

Abanda, P.A., Hannigan, R.E., 2006. Effect of diagenesis on trace element partitioning in shales. Chem. Geol. 230, 42–59.
Abe, M., Suzuki, T., Fujii, Y., Hada, M., Hirao, K., 2008. An ab initio molecular orbital study of the nuclear volume effects in uranium isotope fractionations. J. Chem. Phys. 129, 164309.
Abshire, M.L., Romaniello, S.J., Kuzminov, A.M., Cofrancesco, J., Severmann, S., Riedinger, N., 2020. Uranium isotopes as a proxy for primary depositional redox conditions in organic-rich marine systems. Earth Planet. Sci. Lett. 529, 115878.
Algeo, T.J., Ingall, E., 2007. Sedimentary $C_{org}$: P ratios, paleocean ventilation, and Phanerozoic atmospheric $p_O2$. Palaeogeogr. Palaeoclimatol. Palaeoecol. 256, 130–155.
Algeo, T.J., Li, C., 2020. Redox classification and calibration of redox thresholds in sedimentary systems. Geochim. Cosmochim. Acta 287, 8–26.
Algeo, T.J., Liu, J., 2020. A re-assessment of elemental proxies for paleoredox analysis. Chem. Geol. 540, 119549.
Algeo, T.J., Lyons, T.W., 2006. Mo-total organic carbon covariation in modern anoxic marine environments: Implications for analysis of paleoredox and paleohydrographic conditions. Palaeogeogr. Palaeoclimatol. Palaeoecol. 21, PA1016.
Algeo, T.J., Maynard, J.B., 2004. Trace-element behavior and redox facies in core shales of Upper Pennsylvanian Kansas-type cyclothems. Chem. Geol. 206, 289–318.
Algeo, T.J., Rowe, H., Hower, J.C., Schwark, L., Herrmann, A., Heckel, P., 2008. Changes in ocean denitrification during Late Carboniferous glacial-interglacial cycles. Nature Geosci. 1, 709–712.
Algeo, T.J., Tribovillard, N., 2009. Environmental analysis of paleoceanographic systems based on molybdenum-uranium covariation. Chem. Geol. 268, 211–225.
Amrani, A., 2014. Organosulfur compounds: molecular and isotopic evolution from biota to oil and gas. Annu. Rev. Earth Planet. Sci. 42, 733–768.
Andersen, M.B., Romaniello, S., Vance, D., Little, S.H., Herdman, R., Lyons, T.W., 2014. A modern framework for the interpretation of $^{238}U/^{235}U$ in studies of ancient ocean redox. Earth Planet. Sci. Lett. 400, 184–194.
Andersen, M.B., Vance, D., Morford, J.L., Bura-Nakić, E., Breitenbach, S.F., Och, L., 2016. Closing in on the marine $^{238}U/^{235}U$ budget. Chem. Geol. 420, 11–22.
Andersen, M.B., Stirling, C.H., Weyer, S., 2017. Uranium isotope fractionation. Rev. Mineral. Geochem. 82, 799–850.
Andersen, M.B., Matthews, A., Bar-Matthews, M., Vance, D., 2020. Rapid onset of ocean anoxia shown by high U and low Mo isotope compositions of sapropel S1. Geochem. Perspect. Lett. 15, 10–14.
Anderson, R.F., Fleisher, M.Q., LeHuray, A.P., 1989. Concentration, oxidation state, and particulate flux of uranium in the Black Sea. Geochim. Cosmochim. Acta 53, 2215–2224.

Ardakani, O.H., Chappaz, A., Sanei, H., Mayer, B., 2016. Effect of thermal maturity on remobilization of molybdenum in black shales. Earth Planet. Sci. Lett. 449, 311–320.
Arnold, G.L., Anbar, A.D., Barling, J., Lyons, T.W., 2004. Molybdenum isotope evidence for widespread anoxia in mid-Proterozoic oceans. Science 304, 87–90.
Asael, D., Tissot, F.L., Reinhard, C.T., Rouxel, O., Dauphas, N., Lyons, T.W., Ponzevera, E., Liorzou, C., Chéron, S., 2013. Coupled molybdenum, iron and uranium stable isotopes as oceanic paleoredox proxies during the Paleoproterozoic Shunga Event. Chem. Geol. 362, 193–210.
Barling, J., Anbar, A.D., 2004. Molybdenum isotope fractionation during adsorption by manganese oxides. Earth Planet. Sci. Lett. 217, 315–329.
Barling, J., Arnold, G.L., Anbar, A.D., 2001. Natural mass-dependent variations in the isotopic composition of molybdenum. Earth Planet. Sci. Lett. 193, 447–457.
Barnes, C.E., Cochran, J.K., 1990. Uranium removal in oceanic sediments and the oceanic U balance. Earth Planet. Sci. Lett. 97, 94–101.
Basu, A., Sanford, R.A., Johnson, T.M., Lundstrom, C.C., Löffler, F.E., 2014. Uranium isotopic fractionation factors during U(VI) reduction by bacterial isolates. Geochim. Cosmochim. Acta 136, 100–113.
Bennett, W.W., Canfield, D.E., 2020. Redox-sensitive trace metals as paleoredox proxies: a review and analysis of data from modern sediments. Earth Sci. Rev. 204, 103175.
Bertine, K.K., Turekian, K.K., 1973. Molybdenum in marine deposits. Geochim. Cosmochim. Acta 37, 1415–1434.
Brand, U., Legrand-Blain, M., Streel, M., 2004. Biochemostratigraphy of the DCB global stratotype section and point, Griotte Formation, La Serre, Montagne Noire, France. Palaeogeogr. Palaeoclimatol. Palaeoecol. 205, 337–357.
Brand, U., Veizer, J., 1980. Chemical diagenesis of a multicomponent carbonate system; 1, Trace elements. J. Sediment. Res. 50, 1219–1236.
Brennecka, G.A., Herrmann, A.D., Algeo, T.J., Anbar, A.D., 2011. Rapid expansion of oceanic anoxia immediately before the end-Permian mass extinction. Proc. Natl. Acad. Sci. 108, 17631–17634.
Brezinski, D.K., Cecil, C.B., Skema, V.W., Stamm, R., 2008. Late Devonian glacial deposits from the eastern United States signal an end of the mid-Paleozoic warm period. Palaeogeogr. Palaeoclimatol. Palaeoecol. 268, 143–151.
Brown, S.T., Basu, A., Ding, X., Christensen, J.N., DePaolo, D.J., 2018. Uranium isotope fractionation by abiotic reductive precipitation. Proc. Natl. Acad. Sci. U.S.A. 115, 8688–8693.
Browne, T.N., Hofmann, M.H., Malkowski, M.A., Wei, J., Sperling, E.A., 2020. Redox and paleoenvironmental conditions of the Devonian-Carboniferous Sappington formation, southwestern Montana, and comparison to the Bakken Formation, Williston Basin. Palaeogeogr. Palaeoclimatol. Palaeoecol. 560, 110025.
Bruggmann, S., Gilleaudeau, G.J., Romaniello, S.J., Severmann, S., Canfield, D.E., Anbar, A.D., Scholz, F., Frei, R., 2022. Uranium isotope cycling on the highly productive Peruvian margin. Chem. Geol. 590, 120705.
Brüske, A., Weyer, S., Zhao, M.Y., Planavsky, N.J., Wegwerth, A., Neubert, N., Dellwig, O., Lau, K.V., Lyons, T.W., 2020. Correlated molybdenum and uranium isotope signatures in modern anoxic sediments: implications for their use as paleo-redox proxy. Geochim. Cosmochim. Acta 270, 449–474.
Buggisch, W., Joachimski, M.M., 2006. Carbon isotope stratigraphy of the Devonian of Central and Southern Europe. Palaeogeogr. Palaeoclimatol. Palaeoecol. 240, 68–88.
Bura-Nakić, E., Andersen, M.B., Archer, C., De Souza, G.F., Marguš, M., Vance, D., 2018. Coupled Mo-U abundances and isotopes in a small marine euxinic basin: Constraints on processes in euxinic basins. Geochim. Cosmochim. Acta 222, 212–229.
Canfield, D.E., 2001. Isotope fractionation by natural populations of sulfate-reducing bacteria. Geochim. Cosmochim. Acta 65, 1117–1124.
Canfield, D.E., Raiswell, R., Westrich, J.T., Reaves, C.M., Berner, R.A., 1986. The use of chromium reduction in the analysis of reduced inorganic sulfur in sediments and shales. Chem. Geol. 54, 149–155.
Caplan, M.L., Bustin, R.M., 1998. Palaeoceanographic controls on geochemical characteristics of organic-rich Exshaw mudrocks: role of enhanced primary production. Org. Geochem. 30, 161–188.
Caplan, M.L., Bustin, R.M., 1999. Devonian-Carboniferous Hangenberg mass extinction event, widespread organic-rich mudrock and anoxia: causes and consequences. Palaeogeogr. Palaeoclimatol. Palaeoecol. 148, 187–207.
Caplan, M.L., Bustin, R.M., 2001. Palaeoenvironmental and palaeoceanographic controls on black, laminated mudrock deposition: example from Devonian-Carboniferous strata, Alberta, Canada. Sediment. Geol. 145, 45–72.
Caplan, M.L., Marc Bustin, R., Grimm, K.A., 1996. Demise of a Devonian-Carboniferous carbonate ramp by eutrophication. Geology 24, 715–718.
Caputo, M.V., de Melo, J.H.G., Streel, M., Isbell, J.L., Fielding, C.R., 2008. Late Devonian and early Carboniferous glacial records of South America. Spec. Pap. Geol. Soc. Am. 441, 161–173.
Chen, Z., Chen, Z., Zhang, W., 1997. Quaternary stratigraphy and trace-element indices of the Yangtze Delta, Eastern China, with special reference to marine transgressions. Quat. Res. 47, 181–191.
Chen, X., Ling, H.F., Vance, D., Shields-Zhou, G.A., Zhu, M., Poulton, S.W., Och, L.M., Jiang, S.Y., Li, D., Cremonse, L., Archer, C., 2015. Rise to modern levels of ocean oxygenation coincided with the Cambrian radiation of animals. Nature Comm. 6, 7142.
Chen, X., Romaniello, S.J., Herrmann, A.D., Wasylenki, L.E., Anbar, A.D., 2016. Uranium isotope fractionation during coprecipitation with aragonite and calcite. Geochim. Cosmochim. Acta 188, 189–207.
Chen, X., Romaniello, S.J., Herrmann, A.D., Hardisty, D., Gill, B.C., Anbar, A.D., 2018. Diagenetic effects on uranium isotope fractionation in carbonate sediments from the Bahamas. Geochim. Cosmochim. Acta 237, 294–311.
Chen, D., Wang, J., Racki, G., Li, H., Wang, C., Ma, X., Whalen, M.T., 2013. Large sulphur isotopic perturbations and oceanic changes during the Frasnian-Famennian transition of the Late Devonian. J. Geol. Soc. 170, 465–476.
Chen, J., Zhao, L., Algeo, T.J., Zhou, L., Zhang, L., Qiu, H., 2019. Evaluation of paleomarine redox conditions using Mo-isotope data in low-[Mo] sediments: A case study from the Lower Triassic of South China. Palaeogeogr. Palaeoclimatol. Palaeoecol. 519, 178–193.
Cheng, M., Li, C., Chen, X., Zhou, L., Algeo, T.J., Ling, H.F., Feng, L.J., Jin, C.S., 2018. Delayed Neoproterozoic oceanic oxygenation: evidence from Mo isotopes of the Cryogenian Datangpo Formation. Precambrian Res. 319, 187–197.
Cheng, M., Li, C., Jin, C., Wang, H., Algeo, T.J., Lyons, T.W., Zhang, F., Anbar, A., 2020. Evidence for high organic carbon export to the early Cambrian seafloor. Geochim. Cosmochim. Acta 287, 125–140.
Chiu, C.F., Sweere, T.C., Clarkson, M.O., de Souza, G.F., Hennekam, R., Vance, D., 2022. Co-variation systematics of uranium and molybdenum isotopes reveal pathways for descent into euxinia in Mediterranenan sapropels. Earth Planet. Sci. Lett. 585, 117527.
Clark, S.K., Johnson, T.M., 2008. Effective isotopic fractionation factors for solute removal by reactive sediments: A laboratory microcosm and slurry study. Environ. Sci. Technol. 42, 7850–7855.
Clarkson, M.O., Sweere, T.C., Chiu, C.F., Hennekam, R., Bowyer, F., Wood, R.A., 2023. Environmental controls on very high $\delta^{238}U$ values in reducing sediments: Implications for Neoproterozoic seawater records. Earth-Sci. Rev. 104306.
Cohen, K.M., Finney, S.C., Gibbard, P.L., Fan, J.X., 2013. The ICS international chronostratigraphic chart. Episodes 36, 199–204.
Cole, D., Myrow, P.M., Fike, D.A., Hakim, A., Gehrels, G.E., 2015. Uppermost Devonian (Famennian) to Lower Mississippian events of the western U.S.: stratigraphy, sedimentology, chemostratigraphy, and detrital zircon geochronology. Palaeogeogr. Palaeoclimatol. Palaeoecol. 427, 1–19.
Cole, D.B., Planavsky, N.J., Longley, M., Böning, P., Wilkes, D., Wang, X., Swanner, E.D., Wittkop, C., Loydell, D.K., Busigny, V., Knudsen, A.C., Sperling, E.A., 2020. Uranium isotope fractionation in non-sulfidic anoxic settings and the global uranium isotope mass balance. Global Biogeochem. Cycles 34, 12 e2020GB006649.
Colodner, D., Sachs, J., Ravizza, G., Turekian, K., Edmond, J., Boyle, E., 1993. The geochemical cycle of rhenium: a reconnaissance. Earth Planet. Sci. Lett. 117, 205–221.
Cramer, B.D., Saltzman, M.R., Day, J.E., Witzke, B.J., 2008. Record of the Late Devonian Hangenberg global positive carbon-isotope excursion in an epeiric sea setting: carbonate production, organic-carbon burial and paleoceanography during the Late Famennian. In: Holmden, H., Pratt, B.R. (Eds.), Dynamics of Epeiric Seas: Sedimentological, Paleontological and Geochemical Perspectives. Geosci. Canada. vol. 48, pp. 103–118.
Creaney, S., Allan, J., 1991. Hydrocarbon generation and migration in the Western Canada Sedimentary Basin. In Classic Petroleum Provinces (ed. J. Brooks). Geol. Soc. Spec. Publ. 50, 189–202.
Creaser, R.A., Sannigrahi, P., Chacko, T., Selby, D., 2002. Further evaluation of the Re-Os geochronometer in organic-rich sedimentary rocks: A test of hydrocarbon maturation effects in the Exshaw Formation, Western Canada Sedimentary Basin. Geochim. Cosmochim. Acta 66, 3441–3452.
Cross, M.M., Manning, D.A., Bottrell, S.H., Worden, R.H., 2004. Thermochemical sulphate reduction (TSR): experimental determination of reaction kinetics and implications of the observed reaction rates for petroleum reservoirs. Org. Geochem. 35, 393–404.
Cruse, A.M., Lyons, T.W., 2004. Trace metal records of regional paleoenvironmental variability in Pennsylvanian (Upper Carboniferous) black shales. Chem. Geol. 206, 319–345.
Dahl, T.W., Hammarlund, E.U., Anbar, A.D., Bond, D.P., Gill, B.C., Gordon, G.W., Canfield, D.E., 2010. Devonian rise in atmospheric oxygen correlated to the radiations of terrestrial plants and large predatory fish. Proc. Natl. Acad. Sci. U.S.A. 107, 17911–17915.
Dahl, T.W., Canfield, D.E., Rosing, M.T., Frei, R.E., Gordon, G.W., Knoll, A.H., Anbar, A. D., 2011. Molybdenum evidence for expansive sulfidic water masses in ~750 Ma oceans. Earth Planet. Sci. Lett. 311, 264–274.
Dahl, T.W., Boyle, R.A., Canfield, D.E., Connelly, J.N., Gill, B.C., Lenton, T.M., Bizzarro, M., 2014. Uranium isotopes distinguish two geochemically distinct stages during the later Cambrian SPICE event. Earth Planet. Sci. Lett. 401, 313–326.
Dahl, T.W., Chappaz, A., Fitts, J.P., Lyons, T.W., 2013. Molybdenum reduction in a sulfidic lake: Evidence from X-ray absorption fine-structure spectroscopy and implications for the Mo paleoproxy. Geochim. Cosmochim. Acta 103, 213–231.
Dahl, T.W., Connelly, J.N., Kouchinsky, A., Gill, B.C., Månsson, S.F., Bizzarro, M., 2017. Reorganisation of Earth's biogeochemical cycles briefly oxygenated the oceans 520 Myr ago. Geochem. Perspect. Lett. 3, 210–220.
Dahl, T.W., Hammarlund, E.U., Rasmussen, C.M.O., Bond, D.P.G., Canfield, D.E., 2021. Sulfidic anoxia in the oceans during the late ordovician mass extinctions; insights from molybdenum and uranium isotopic global redox proxies. Earth-Sci. Rev. 220, 103748.
Dang, D.H., Evans, R.D., Wang, W., Omanović, D., El Houssainy, A., Lenoble, V., Mullot, J.U., Mounier, S., Garnier, C., 2018. Uranium isotope geochemistry in modern coastal sediments: Insights from Toulon Bay. France. Chem. Geol. 481, 133–145.
di Pasquo, M., Grader, G.W., Kondas, M., Doughty, P.T., Filipiak, P., Rice, B.J., Isaacson, P.E., 2019. Lower Sappington formation palynofacies in Montana confirm upper famennian black shale paleoenvironments and sequences across western North America. Palaeogeogr. Palaeoclimatol. Palaeoecol. 536, 109370.
Dickson, A.J., Idiz, E., Porcelli, D., van den Boorn, S.H., 2020. The influence of thermal maturity on the stable isotope compositions and concentrations of molybdenum, zinc and cadmium in organic-rich marine mudrocks. Geochim. Cosmochim. Acta 287, 205–220.

Dickson, A.J., Idiz, E., Porcelli, D., Murphy, M.J., Celestino, R., Jenkyns, H.C., Poulton, S. W., Hesselbo, S.P., Hooker, J.N., Ruhl, M., van den Boorn, S.H., 2022. No effect of thermal maturity on the Mo, U, Cd, and Zn isotope compositions of Lower Jurassic organic-rich sediments. Geology 50, 598–602.
Dunk, R.M., Mills, R.A., Jenkins, W.J., 2002. A revaluation of the oceanic uranium budget for the Holocene. Chem. Geol. 190, 45–67.
Emerson, S.R., Huested, S.S., 1991. Ocean anoxia and the concentrations of molybdenum and vanadium in seawater. Mar. Chem. 34, 177–196.
Erickson, B.E., Helz, G.R., 2000. Molybdenum (VI) speciation in sulfidic waters:: stability and lability of thiomolybdates. Geochim. Cosmochim. Acta 64, 1149–1158.
Ernst, R.E., Rodygin, S.A., Grinev, O.M., 2020. Age correlation of Large Igneous Provinces with Devonian biotic crises. Glob. Planet. Change 185, 103097.
Eroglu, S., Scholz, F., Salvatteci, R., Siebert, C., Schneider, R., Frank, M., 2021. The impact of postdepositional alteration on iron- and molybdenum-based redox proxies. Geology 49, 1411–1415.
Ferri, F., McMechan, M., Richards, M.B., Friedman, R., 2021. Organic-rich Upper Devonian shales of the Patry and Exshaw formations (Besa River Group) in the subsurface of Liard basin. British Columbia Ministry of Energy, Mines and Low Carbon Innovation, British Columbia Geological Survey Paper 42.
Fields, B.D., Melott, A.L., Ellis, J., Ertel, A.F., Fry, B.J., Lieberman, B.S., Liu, Z.H., Miller, J.A., Thomas, B.C., 2020. Supernova triggers for end-Devonian extinctions. Proc. Natl. Acad. Sci. U.S.A. 117, 21008–21010.
Filipiak, P., Racki, G., 2010. Proliferation of abnormal palynoflora during the end-Devonian biotic crisis. Geol. Quart. 54, 1–14.
Formolo, M.J., Riedinger, N., Gill, B.C., 2014. Geochemical evidence for euxinia during the Late Devonian extinction events in the Michigan Basin (USA). Palaeogeogr. Palaeoclimatol. Palaeoecol. 414, 146–154.
Gangl, S.K., Stirling, C.H., Jenkyns, H.C., Preston, W.J., Clarkson, M.O., Moy, C.M., Dickson, A.J., Porcelli, D., 2023. Regional conditions cause contrasting behaviour in U-isotope fractionation in black shales: Constraints for global ocean palaeo-redox reconstructions. Chem. Geol. 623, 121411.
Ge, C., Slaymaker, O., Pedersen, T.F., 2003. Change in the sedimentary environment of Wanquan river Estuary, Hainan Island, China. Chin. Sci. Bull. 48, 2357–2361.
Gilleaudeau, G.J., Romaniello, S.J., Luo, G., Kaufman, A.J., Zhang, F., Klaebe, R.M., Kah, L.C., Azmy, K., Bartley, J.K., Zheng, W.J. E., Letters, P.S., 2019. Uranium isotope evidence for limited euxinia in mid-Proterozoic oceans. Earth Planet. Sci. Lett. 521, 150–157.
Goldberg, T., Gordon, G., Izon, G., Archer, C., Pearce, C.R., McManus, J., Anbar, A.D., Rehkämper, M., 2013. Resolution of inter-laboratory discrepancies in Mo isotope data: an intercalibration. J. Anal. At. Spectrom. 28, 724–735.
Goldberg, T., Poulton, S.W., Wagner, T., Kolonic, S.F., Rehkämper, M., 2016. Molybdenum drawdown during cretaceous oceanic anoxic event 2. Earth Planet. Sci. Lett. 440, 81–91.
Gonzalez, F., Moreno, C., Santos, A., 2006. The massive sulphide event in the Iberian Pyrite Belt: confirmatory evidence from the Sotiel-Coronada Mine. Geol. Mag. 143, 821–827.
Goto, K.T., Anbar, A.D., Gordon, G.W., Romaniello, S.J., Shimoda, G., Takaya, Y., Tokumaru, A., Nozaki, T., Suzuki, K., Machida, S., Hanyu, T., Usui, A., 2014. Uranium isotope systematics of ferromanganese crusts in the Pacific Ocean: Implications for the marine $^{238}U/^{235}U$ isotope system. Geochim. Cosmochim. Acta 146, 43–58.
Harrison, A.G., Thode, H.G., 1958. Mechanisms of the bacterial reduction of sulfate from isotope fractionation studies. Trans. Faraday Soc. 53, 84–92.
He, Z., Clarkson, M.O., Andersen, M.B., Archer, C., Sweere, T.C., Kraal, P., Guthauser, A., Huang, F., Vance, D., 2021. Temporally and spatially dynamic redox conditions on an upwelling margin: The impact on coupled sedimentary Mo and U isotope systematics, and implications for the Mo-U paleoredox proxy. Geochim. Cosmochim. Acta 309, 251–271.
Heath, M.N., Cramer, B.D., Stolfus, B.M., Barnes, G.L., Clark, R.J., Day, J.E., Barnett, B. A., Witzke, B.J., Hogancamp, N.J., Tassier-Surine, S., 2021. Chemoautotrophy as the driver of decoupled organic and carbonate carbon isotope records at the onset of the Hangenberg (Devonian-Carboniferous Boundary) Oceanic Anoxic Event. Palaeogeogr. Palaeoclimatol. Palaeoecol. 577, 110540.
Helz, G.R., Vorlicek, T.P., 2019. Precipitation of molybdenum from euxinic waters and the role of organic matter. Chem. Geol. 509, 178–193.
Helz, G.R., Bura-Nakić, E., Mikac, N., Ciglenečki, I., 2011. New model for molybdenum behavior in euxinic waters. Chem. Geol. 284, 323–332.
Helz, G.R., Miller, C.V., Charnock, J.M., Mosselmans, J.F.W., Pattrick, R.A.D., Garner, C. D., Vaughan, D.J., 1996. Mechanism of molybdenum removal from the sea and its concentration in black shales: EXAFS evidence. Geochim. Cosmochim. Acta 60, 3631–3642.
Herrmann, A.D., Kendall, B., Algeo, T.J., Gordon, G.W., Wasylenki, L.E., Anbar, A.D., 2012. Anomalous molybdenum isotope trends in Upper Pennsylvanian euxinic facies: Significance for use of $\delta^{98}$Mo as a global marine redox proxy. Chem. Geol. 324, 87–98.
Hieshima, G.B., Pratt, L.M., 1991. Sulfur/carbon ratios and extractable organic matter of the Middle Proterozoic Nonesuch Formation. North American Midcontinent rift. Precambrian Res. 54, 65–79.
Higgins, A.C., Richards, B.C., Henderson, C.M., 1991. Conodont biostratigraphy and paleoecology of the uppermost Devonian and Carboniferous of the Western Canada Sedimentary Basin. In: Orchard, M.J., McCracken, A.D. (Eds.), Ordovician to Triassic Conodont Paleontology of the Canadian Cordillera. Geological Survey of Canada, Calgary, Canada, pp. 215–251.
Holmden, C., Amini, M., Francois, R., 2015. Uranium isotope fractionation in Saanich Inlet: A modern analog study of a paleoredox tracer. Geochim Cosmochim Acta. 153, 202–215.
Isaacson, P.E., Diaz-Martinez, E., Grader, G.W., Kalvoda, J., Babek, O., Devuyst, F.X., 2008. Late Devonian–earliest Mississippian glaciation in Gondwanaland and its biogeographic consequences. Palaeogeogr. Palaeoclimatol. Palaeoecol. 268, 126–142.
Johnson, J., Klapper, G., Sandberg, C.A., 1985. Devonian eustatic fluctuations in Euramerica. Geol. Soc. Am. Bull. 96, 567–587.
Johnston, D.I., Henderson, C.M., Schmidt, M.J., 2010. Upper Devonian to Lower Mississippian conodont biostratigraphy of uppermost Wabamun Group and Palliser Formation to lowermost Banff and Lodgepole formations, southern Alberta and southeastern British Columbia, Canada: implications for correlations and sequence stratigraphy. Bulletin Can. Pet. Geol. 58, 295–341.
Kabanov, P., Jiang, C., 2020. Photic-zone euxinia and anoxic events in a Middle-Late Devonian shelfal sea of Panthalassan continental margin, NW Canada: Changing paradigm of Devonian ocean and sea level fluctuations. Glob. Planet. Change 188, 103153.
Kaiser, S.I., Steuber, T., Becker, R.T., 2008. Environmental change during the Late Famennian and Early Tournaisian (Late Devonian-Early Carboniferous)-implications from stable isotopes and conodont biofacies in southern Europe. In: Aretz, M., Herbig, H. G. and Somerville, I. D. (Eds) Carboniferous Platforms and Basins. Geol. J. vol. 43, pp. 241–260.
Kaiser, S.I., Steuber, T., Becker, R.T., Joachimski, M.M., 2006. Geochemical evidence for major environmental change at the Devonian-Carboniferous boundary in the Carnic Alps and the Rhenish Massif. Palaeogeogr. Palaeoclimatol. Palaeoecol. 240, 146–160.
Kaiser, S.I., Becker, R.T., Steuber, T., Aboussalam, S.Z., 2011. Climate-controlled mass extinctions, facies, and sea-level changes around the Devonian-Carboniferous boundary in the eastern Anti-Atlas (SE Morocco). Palaeogeogr. Palaeoclimatol. Palaeoecol. 310, 340–364.
Kaiser, S.I., Aretz, M., Becker, R.T., 2016. The global Hangenberg Crisis (Devonian-Carboniferous transition): review of a first-order mass extinction. Geol. Soc. London Spec. Publ. 423, 387–437.
Kampschulte, A., Strauss, H., 2004. The sulfur isotopic evolution of Phanerozoic seawater based on the analysis of structurally substituted sulfate in carbonates. Chem. Geol. 204, 255–286.
Kazmierczak, J., Kremer, B., Racki, G., 2012. Late Devonian marine anoxia challenged by benthic cyanobacterial mats. Geobiology 10, 371–383.
Kendall, B., 2021. Recent advances in geochemical paleo-oxybarometers. Annu. Rev. Earth Planet. Sci. 49, 399–433.
Kendall, B., Creaser, R.A., Gordon, G.W., Anbar, A.D., 2009. Re-Os and Mo isotope systematics of black shales from the Middle Proterozoic Velkerri and Wollogorang Formations, McArthur Basin, northern Australia. Geochim. Cosmochim. Acta 73, 2534–2558.
Kendall, B., Gordon, G.W., Poulton, S.W., Anbar, A.D., 2011. Molybdenum isotope constraints on the extent of late Paleoproterozoic ocean euxinia. Earth Planet. Sci. Lett. 307, 450–460.
Kendall, B., Brennecka, G.A., Weyer, S., Anbar, A.D., 2013. Uranium isotope fractionation suggests oxidative uranium mobilization at 2.50 Ga. Chem. Geol. 362, 105–114.
Kendall, B., Komiya, T., Lyons, T.W., Bates, S.M., Gordon, G.W., Romaniello, S.J., Jiang, G., Creaser, R.A., Xiao, S., McFadden, K., Sawaki, Y., Tahata, M., Shu, D., Han, J., Li, Y., Chu, X., Anbar, A.D., 2015. Uranium and molybdenum isotope evidence for an episode of widespread ocean oxygenation during the late Ediacaran Period. Geochim. Cosmochim. Acta 156, 173–193.
Kendall, B., Dahl, T.W., Anbar, A.D., 2017. The stable isotope geochemistry of molybdenum. Rev. Mineral. Geochem. 82, 683–732.
Kendall, B., Wang, J., Zheng, W., Romaniello, S.J., Over, D.J., Bennett, Y., Xing, L., Kunert, A., Boyes, C., Liu, J., 2020. Inverse correlation between the molybdenum and uranium isotope compositions of Upper Devonian black shales caused by changes in local depositional conditions rather than global ocean redox variations. Geochim. Cosmochim. Acta 287, 141–164.
King, E.K., Pett-Ridge, J.C., 2018. Reassessing the dissolved molybdenum isotopic composition of ocean inputs: The effect of chemical weathering and groundwater. Geology 46, 955–958.
King, H.E., Walters, C.C., Horn, W.C., Zimmer, M., Heines, M.M., Lamberti, W.A., Kliewer, C., Pottorf, R.J., Macleod, G., 2014. Sulfur isotope analysis of bitumen and pyrite associated with thermal sulfate reduction in reservoir carbonates at the Big Piney-La Barge production complex. Geochim. Cosmochim. Acta 134, 210–220.
Kipp, M.A., Li, H., Ellwood, M.J., John, S.G., Middag, R., Adkins, J.F., Tissot, F.L., 2022. $^{238}U$, $^{235}U$ and $^{234}U$ in seawater and deep-sea corals: A high-precision reappraisal. Geochim. Cosmochim. Acta 336, 231–248.
Kipp, M.A., Tissot, F.L., 2022. Inverse methods for consistent quantification of seafloor anoxia using uranium isotope data from marine sediments. Earth Planet. Sci. Lett. 577, 117240.
Krouse, H.R., Viau, C.A., Eliuk, L.S., Ueda, A., Halas, S., 1988. Chemical and isotopic evidence of thermochemical sulfate reduction by light hydrocarbon gases in deep carbonate reservoirs. Nature 333, 415–419.
Kumpan, T., Babek, O., Kalvoda, J., Fryda, J., Grygar, T.M., 2013. A high-resolution, multiproxy stratigraphic analysis of the Devonian-Carboniferous boundary sections in the Moravian Karst (Czech Republic) and a correlation with the Carnic Alps (Austria). Geol. Mag. 151, 201–215.
Kumpan, T., Bábek, O., Kalvoda, J., Grygar, T.M., Frýda, J., 2014. Sea-level and environmental changes around the Devonian–Carboniferous boundary in the Namur–Dinant Basin (S Belgium, NE France): a multi-proxy stratigraphic analysis of carbonate ramp archives and its use in regional and interregional correlations. Sediment. Geol. 311, 43–59.

Kumpan, T., Kalvoda, J., Bábek, O., Holá, M., Kanický, V., 2019. Tracing paleoredox conditions across the Devonian-Carboniferous boundary event: A case study from carbonate-dominated settings of Belgium, the Czech Republic, and northern France. Sediment. Geol. 380, 143–157.
Kunert, A., Clarke, J., Kendall, B., 2020. Molybdenum isotope constraints on the origin of vanadium hyper-enrichments in ediacaran-phanerozoic marine mudrocks. Minerals 10, 1075.
Kunert, A., Kendall, B., 2023. Global ocean redox changes before and during the Toarcian Oceanic Anoxic Event. Nature Comm. 14, 815.
Lau, K.V., Macdonald, F.A., Maher, K., Payne, J.L., 2017. Uranium isotope evidence for temporary ocean oxygenation in the aftermath of the Sturtian Snowball Earth. Earth Planet. Sci. Lett. 458, 282–292.
Lau, K.V., Lyons, T.W., Maher, K., 2020. Uranium reduction and isotopic fractionation in reducing sediments: Insights from reactive transport modeling. Geochim. Cosmochim. Acta 287, 65–92.
Lau, K.V., Hancock, L.G., Severmann, S., Kuzminov, A., Cole, D.B., Behl, R.J., Planavsky, N.J., Lyons, T.W., 2022. Variable local basin hydrography and productivity control the uranium isotope paleoredox proxy in anoxic black shales. Geochim. Cosmochim. Acta 317, 433–456.
Leenheer, M.J., 1984. Mississippian Bakken and other equivalent formations as source rocks in the Western Canada basin. Org. Geochem. 6, 521–533.
Lev, S.M., McLennan, S.M., Hanson, G.N., 2000. Late diagenetic redistribution of uranium and disturbance of the U-Pb whole rock isotope system in a black shale. J. Sediment. Res. 70, 1234–1245.
Li, J., Azmy, K., Kendall, B., 2022b. The Mo- and U-isotope signatures in alternating shales and carbonate interbeds of rhythmites: A comparison and implications for redox conditions across the Cambrian-Ordovician boundary. Chem. Geol. 602, 120882.
Li, S., Wignall, P.B., Poulton, S.W., Hedhli, M., Grasby, S.E., 2022a. Carbonate shutdown, phosphogenesis and the variable style of marine anoxia in the late Famennian (Late Devonian) in western Laurentia. Palaeogeogr. Palaeoclimatol. Palaeoecol. 589, 110835.
Liseroudi, M.H., Ardakani, O.H., Pedersen, P.K., Stern, R.A., Wood, J.M., Sanei, H., 2021. Microbial and thermochemical controlled sulfur cycle in the Early Triassic sediments of the Western Canadian Sedimentary Basin. J. Geol. Soc. 178 jgs2020-175.
Liu, Y.Q., Ji, Q., Kuang, H.W., Jiang, X.J., Xu, H., Peng, N., 2012. U-Pb zircon age, sedimentary facies, and sequence stratigraphy of the Devonian-Carboniferous boundary, Daposhang Section, Guizhou, China. Palaeoworld 21, 100–107.
Liu, J., Qie, W., Algeo, T.J., Yao, L., Huang, J., Luo, G., 2016. Changes in marine nitrogen fixation and denitrification rates during the end-Devonian mass extinction. Palaeogeogr. Palaeoclimatol. Palaeoecol. 448, 195–206.
Liu, J., Luo, G., Lu, Z., Lu, W., Qie, W., Zhang, F., Wang, X., Xie, S., 2019. Intensified ocean deoxygenation during the end Devonian mass extinction. Geochemistry. Geophys. Geosystems 20, 6187–6198.
Lu, X., Kendall, B., Stein, H.J., Li, C., Hannah, J.L., Gordon, G.W., Ebbestad, J.O.R., 2017. Marine redox conditions during deposition of Late Ordovician and Early Silurian organic-rich mudrocks in the Siljan ring district, central Sweden. Chem. Geol. 457, 75–94.
Lu, X., Dahl, T.W., Zheng, W., Wang, S., Kendall, B., 2020. Estimating ancient seawater isotope compositions and global ocean redox conditions by coupling the molybdenum and uranium isotope systems of euxinic organic-rich mudrocks. Geochim. Cosmochim. Acta 290, 76–103.
Lu, X., Edwards, C.T., Kendall, B., 2023. No evidence for expansion of global ocean euxinia during the base Stairsian mass extinction event (Tremadocian, Early Ordovician). Geochim. Cosmochim. Acta 341, 116–131.
Lu, Z., Hu, R., Han, T., Wen, H., Mo, B., Algeo, T.J., 2021. Control of V accumulation in organic-rich shales by clay-organic nanocomposites. Chem. Geol. 567, 120100.
Lyons, T.W., Severmann, S., 2006. A critical look at iron paleoredox proxies: New insights from modern euxinic marine basins. Geochim. Cosmochim. Acta 70, 5698–5722.
Machel, H.G., 2001. Bacterial and thermochemical sulfate reduction in diagenetic settings—old and new insights. Sediment. Geol. 140, 143–175.
Machel, H.G., Krouse, H.R., Sassen, R., 1995. Products and distinguishing criteria of bacterial and thermochemical sulfate reduction. Appl. Geochem. 10, 373–389.
MacQueen, R.A., Sandberg, C.A., 1970. Stratigraphy, age, and interregional correlation of the Exshaw Formation, Alberta Rocky Mountains. Bulletin Can. Pet Geol. 18, 32–66.
Magnall, J.M., Gleeson, S.A., Poulton, S.W., Gordon, G.W., Paradis, S., 2018. Links between seawater paleoredox and the formation of sediment-hosted massive sulphide (SHMS) deposits—Fe speciation and Mo isotope constraints from Late Devonian mudstones. Chem. Geol. 490, 45–60.
Martinez, A.M., Boyer, D.L., Droser, M.L., Barrie, C., Love, G.D., 2019. A stable and productive marine microbial community was sustained through the end-Devonian Hangenberg Crisis within the Cleveland Shale of the Appalachian Basin, United States. Geobiology 17, 27–42.
Marynowski, L., Filipiak, P., 2007. Water column euxinia and wildfire evidence during deposition of the Upper Famennian Hangenberg event horizon from the Holy Cross Mountains (central Poland). Geol. Mag. 144, 569–595.
Marynowski, L., Zaton, M., Rakocinski, M., Filipiak, P., Kurkiewicz, S., Pearce, T.J., 2012. Deciphering the upper Famennian Hangenberg Black Shale depositional environments based on multi-proxy record. Palaeogeogr. Palaeoclimatol. Palaeoecol. 346, 66–86.
Matyja, H., Sobien, K., Marynowski, L., Stempien-Salek, M., Malkowski, K., 2014. The expression of the Hangenberg Event (latest Devonian) in a relatively shallow-marine succession (Pomeranian Basin, Poland): the results of a multi-proxy investigation. Geol. Mag. 153, 429–443.
Mayer, B., Krouse, H.R., 2004. Procedures for sulfur isotope abundance studies. In: de Groot, P.A. (Ed.), Handbook of Stable Isotope Analytical Techniques, pp. 538–596.
McDonald, B.S., Partin, C.A., Sageman, B., Holmden, C., 2022. Uranium isotope reconstruction of ocean deoxygenation during OAE 2 hampered by uncertainties in fractionation factors and local U-cycling. Geochim. Cosmochim Acta. 331, 143–164.
McGhee, G.R., Clapham, M.E., Sheehan, P.M., Bottjer, D.J., Droser, M.L., 2013. A new ecological-severity ranking of major Phanerozoic biodiversity crises. Palaeogeogr. Palaeoclimatol. Palaeoecol. 370, 260–270.
McLennan, S.M., 2001. Relationships between the trace element composition of sedimentary rocks and upper continental crust. Geochem. Geophys. Geosyst. 2, 2000GC000109.
McManus, J., Nägler, T.F., Siebert, C., Wheat, C.G., Hammond, D.E., 2002. Oceanic molybdenum isotope fractionation: Diagenesis and hydrothermal ridge-flank alteration. Geochem. Geophys. Geosyst. 3, 1–9.
Melott, A.L., Thomas, B.C., Fields, B.D., 2020. Climate change via $CO_2$ drawdown from astrophysically initiated atmospheric ionization? Int. J. Astrobiology 19, 349–352.
Menard, H.W., Smith, S.M., 1966. Hypsometry of ocean basin provinces. J. Geophys. Res. 71, 4305–4325.
Middelburg, J.J., Soetaert, K., Herman, P.M., Heip, C.H., 1996. Denitrification in marine sediments: A model study. Glob. Biogeochem. Cycles 10, 661–673.
Miller, C.A., Peucker-Ehrenbrink, B., Walker, B.D., Marcantonio, F., 2011. Re-assessing the surface cycling of molybdenum and rhenium. Geochim. Cosmochim. Acta 75, 7146–7179.
Montoya-Pino, C., Weyer, S., Anbar, A.D., Pross, J., Oschmann, W., van de Schootbrugge, B., Arz, H.W., 2010. Global enhancement of ocean anoxia during Oceanic Anoxic Event 2: A quantitative approach using U isotopes. Geology 38, 315–318.
Moore, W.S., 1996. Large groundwater inputs to coastal waters revealed by $^{226}Ra$ enrichments. Nature 380, 612–614.
Morford, J.L., Emerson, S., 1999. The geochemistry of redox sensitive trace metals in sediments. Geochim Cosmochim Acta 63, 1735–1750.
Morford, J.L., Emerson, S.R., Breckel, E.J., Kim, S.H., 2005. Diagenesis of oxyanions (V, U, Re, and Mo) in pore waters and sediments from a continental margin. Geochim. Cosmochim Acta. 69, 5021–5032.
Myrow, P.M., Strauss, J.V., Creveling, J.R., Sicard, K.R., Ripperdan, R., Sandberg, C.A., Hartenfels, S., 2011. A carbon isotopic and sedimentological record of the latest Devonian (Famennian) from the Western U.S. and Germany. Palaeogeogr. Palaeoclimatol. Palaeoecol. 306, 147–159.
Myrow, P.M., Ramezani, J., Hanson, A.E., Bowring, S.A., Racki, G., Rakociński, M., 2014. High-precision U-Pb age and duration of the latest Devonian (Famennian) Hangenberg event, and its implications. Terra Nova 26, 222–229.
Nägler, T.F., Neubert, N., Böttcher, M.E., Dellwig, O., Schnetger, B., 2011. Molybdenum isotope fractionation in pelagic euxinia: Evidence from the modern Black and Baltic Seas. Chem. Geol. 289, 1–11.
Nägler, T.F., Anbar, A.D., Archer, C., Goldberg, T., Gordon, G.W., Greber, N.D., Siebert, C., Sohrin, Y., Vance, D., 2014. Proposal for an international molybdenum isotope measurement standard and data representation. Geostand. Geoanal. Res. 38, 149–151.
Nakagawa, Y., Takano, S., Firdaus, M.L., Norisuye, K., Hirata, T., Vance, D., Sohrin, Y., 2012. The molybdenum isotopic composition of the modern ocean. Geochem. J. 46, 131–141.
Neely, R.A., Gislason, S.R., Ólafsson, M., McCoy-West, A.J., Pearce, C.R., Burton, K.W., 2018. Molybdenum isotope behaviour in groundwaters and terrestrial hydrothermal systems. Iceland. Earth Planet. Sci. Lett. 486, 108–118.
Noordmann, J., Weyer, S., Montoya-Pino, C., Dellwig, O., Neubert, N., Eckert, S., Paetzel, M., Böttcher, M.E., 2015. Uranium and molybdenum isotope systematics in modern euxinic basins: Case studies from the central Baltic Sea and the Kyllaren fjord (Norway). Chem. Geol. 396, 182–195.
Neubert, N., Nägler, T.F., Böttcher, M.E., 2008. Sulfidity controls molybdenum isotope fractionation into euxinic sediments: Evidence from the modern Black Sea. Geology 36, 775–778.
Noordmann, J., Weyer, S., Georg, R.B., Jöns, S., Sharma, M., 2016. $^{238}U/^{235}U$ isotope ratios of crustal material, rivers and products of hydrothermal alteration: New insights on the oceanic U isotope mass balance. Isotopes Environ. Health Stu. 52, 141–163.
Orr, W.L., 1977. Geologic and geochemical controls on the distribution of hydrogen sulfide in natural gas. In: Advances in Org. Geochem, pp. 571–597.
Ostrander, C.M., Sahoo, S.K., Kendall, B., Jiang, G., Planavsky, N.J., Lyons, T.W., Nielsen, S.G., Owens, J.D., Gordon, G.W., Romaniello, S.J., Anbar, A.D., 2019. Multiple negative molybdenum isotope excursions in the Doushantuo Formation (South China) fingerprint complex redox-related processes in the Ediacaran Nanhua Basin. Geochim. Cosmochim. Acta 261, 191–209.
Pan, W., Cao, M., Du, Y., Cheng, M., Zhou, Y.Q., Algeo, T.J., Zhao, M.Y., Thibault, N., Li, C., Wei, G.Y., Dahl, T.W., 2021. Paired U and Mo isotope evidence for pervasive anoxia in the Cryogenian early interglacial ocean. Precambrian Res. 361, 106244.
Paschall, O., Carmichael, S.K., Königshof, P., Waters, J.A., Ta, P.H., Komatsu, T., Dombrowski, A., 2019. The Devonian-Carboniferous boundary in Vietnam: Sustained ocean anoxia with a volcanic trigger for the Hangenberg Crisis? Glob. Planet. Change 175, 64–81.
Peters, K.E., 1986. Guidelines for evaluating petroleum source rock using programmed pyrolysis. AAPG Bull. 70, 318–329.
Piggott, N., Lines, M.D., 1991. A case study of migration from the West Canada Basin. In Petroleum Migration (eds. W. A. England and A. J. Fleet). Geol. Soc. Spec. Publ. 59, 207–225.
Pisarzowska, A., Rakociński, M., Marynowski, L., Szczerba, M., Thoby, M., Paszkowski, M., Perri, M.C., Spalletta, C., Schönlaub, H.P., Kowalik, N., Gereke, M.,

2020. Large environmental disturbances caused by magmatic activity during the Late Devonian Hangenberg Crisis. Glob. Planet. Change 190, 103155.
Porter, S.J., Selby, D., Cameron, V., 2014. Characterising the nickel isotopic composition of organic-rich marine sediments. Chem. Geol. 387, 12–21.
Poulson, R.L., Siebert, C., McManus, J., Berelson, W.M., 2006. Authigenic molybdenum isotope signatures in marine sediments. Geology 34, 617–620.
Poulton, S.W., Canfield, D.E., 2005. Development of a sequential extraction procedure for iron: implications for iron partitioning in continentally derived particulates. Chem. Geol. 214, 209–221.
Poulton, S.W., Canfield, D.E., 2011. Ferruginous conditions: a dominant feature of the ocean through Earth's history. Elements 7, 107–112.
Poulton, S.W., Raiswell, R., 2002. The low-temperature geochemical cycle of iron: From continental fluxes to marine sediment deposition. Am. J. Sci. 302, 774–805.
Pracht, M., Batchelor, R., 1998. A geochemical study of late Devonian and early Carboniferous tuffs from the South Munster Basin, Ireland. Iri. J. Earth Sci. 17, 25–38.
Pratt, B.R., van Heerde, J., 2016. An arborescent lycopsid stem fragment from the Palliser Formation (Famennian) carbonate platform, southwestern Alberta, Canada, and its paleogeographic and paleoclimatic significance. Can. J. Earth Sci. 54, 141–145.
Qie, W., Liu, J., Chen, J., Wang, X., Mii, H.S., Zhang, X., Huang, X., Yao, L., Luo, G., 2015. Local overprints on the global carbonate $\delta^{13}C$ signal in Devonian-Carboniferous boundary successions of South China. Palaeogeogr. Palaeoclimatol. Palaeoecol. 418, 290–303.
Raiswell, R., Berner, R.A., 1987. Organic carbon losses during burial and thermal maturation of normal marine shales. Geology 15, 853–856.
Raiswell, R., Hardisty, D.S., Lyons, T.W., Canfield, D.E., Owens, J.D., Planavsky, N.J., Poulton, S.W., Reinhard, C.T., 2018. The iron paleoredox proxies: A guide to the pitfalls, problems and proper practice. Amer. J. Sci. 318, 491–526.
Rakociński, M., Pisarzowska, A., Corradini, C., Narkiewicz, K., Dubicka, Z., Abdiyev, N., 2021. Mercury spikes as evidence of extended arc-volcanism around the Devonian-Carboniferous boundary in the South Tian Shan (southern Uzbekistan). Sci. Rep. 11, 1–15.
Reinhard, C.T., Planavsky, N.J., Robbins, L.J., Partin, C.A., Gill, B.C., Lalonde, S.V., Bekker, A., Konhauser, K.O., Lyons, T.W., 2013. Proterozoic ocean redox and biogeochemical stasis. Proc. Natl. Acad. Sci. U.S.A. 110, 5357–5362.
Richards, B.C., Ross, G.M., Utting, J., 2002. U-Pb geochronology, lithostratigraphy and biostratigraphy of tuff in the upper Famennian to Tournaisian Exshaw Formation: Evidence for a mid-Paleozoic magmatic arc on the northwestern margin of North America. In Hills, L.V., et al. (Eds.), Carboniferous and Permian of the world: Canadian Society of Petroleum Geologists Memoir. vol. 19, pp. 158–207.
Richards, B.C., Higgins, A.C., 1988. Devonian-Carboniferous boundary beds of the Palliser and Exshaw formations at Jura Creek, Rocky Mountains, southwestern Alberta. In: McMillan, N.J., Embry, A.F., Glass, D.J. (Eds.), Devonian of the world. Canadian Society of Petroleum Geologists Memoir, pp. 399–412.
Robison, V.D., 1995. The Exshaw Formation: a Devonian/Mississippian hydrocarbon source in the Western Canada Basin. Petroleum Source Rocks 9–24.
Rolison, J.M., Stirling, C.H., Middag, R., Rijkenberg, M.J., 2017. Uranium stable isotope fractionation in the Black Sea: Modern calibration of the $^{238}U/^{235}U$ paleo-redox proxy. Geochim. Cosmochim. Acta 203, 69–88.
Romaniello, S.J., Herrmann, A.D., Anbar, A.D., 2013. Uranium concentrations and $^{238}U/^{235}U$ isotope ratios in modern carbonates from the Bahamas: Assessing a novel paleoredox proxy. Chem. Geol. 362, 305–316.
Ross, D.J., Bustin, R.M., 2009. Investigating the use of sedimentary geochemical proxies for paleoenvironment interpretation of thermally mature organic-rich strata: Examples from the Devonian-Mississippian shales, Western Canadian Sedimentary Basin. Chem. Geol. 260, 1–19.
Ryder, R.T., 1996. Fracture patterns and their origin in the upper Devonian Antrim Shale gas reservoir of the Michigan basin; a review. US Department of the Interior. US Geological Survey.
Sahoo, S.K., Gilleaudeau, G.J., Wilson, K., Hart, B., Barnes, B.D., Faison, T., Bowman, A. R., Larsen, T.E., Kaufman, A.J., 2023. Basin-scale reconstruction of euxinia and Late Devonian mass extinctions. Nature 615, 640–645.
Sandberg, C.A., Morrow, J.R., Ziegler, W., 2002. Late Devonian sea-level changes, catastrophic events, and mass extinctions. In: Koeberl, C., Macleod, K.G. (Eds.), Catastrophic Events and Mass Extinction: Impacts and Beyond. Geological Society of America Special. Paper. vol. 356, pp. 473–487.
Savoy, L.E., Harris, A.G., 1993. Conodont biofacies and taphonomy along a carbonate ramp to black shale basin (latest Devonian and earliest), southernmost Canadian Cordillera and adjacent Montana. Can. J. Earth Sci. 30, 2404–2422.
Savoy, L.E., 1990. Sedimentary record of Devonian-Mississippian carbonate and black shale systems, southernmost Canadian Rockies and adjacent Montana: facies and processes.
Scholze, F., Gess, R.W., 2017. Oldest known naiaditid bivalve from the high-latitude Late Devonian (Famennian) of South Africa offers clues to survival strategies following the Hangenberg mass extinction. Palaeogeogr. Palaeoclimatol. Palaeoecol. 471, 31–39.
Scott, C., Lyons, T.W., Bekker, A., Shen, Y.A., Poulton, S.W., Chu, X.L., Anbar, A.D., 2008. Tracing the stepwise oxygenation of the Proterozoic ocean. Nature 452, 456–459.
Scotese, C.R., McKerrow, W.S., 1990. Revised world maps and introduction. Geol. Soc. London Memoirs 12, 1–21.
Scott, C., Lyons, T.W., 2012. Contrasting molybdenum cycling and isotopic properties in euxinic versus non-euxinic sediments and sedimentary rocks: Refining the paleoproxies. Chem. Geol. 324, 19–27.
Scott, C., Slack, J.F., Kelley, K.D., 2017. The hyper-enrichment of V and Zn in black shales of the Late Devonian-Early Mississippian Bakken Formation (USA). Chem. Geol. 452, 24–33.
Seewald, J.S., 2003. Organic–inorganic interactions in petroleum-producing sedimentary basins. Nature 426, 327–333.
Selby, D., Creaser, R.A., 2003. Re–Os geochronology of organic rich sediments: An evaluation of organic matter analysis methods. Chem. Geol. 200, 225–240.
Selby, D., Creaser, R.A., 2005. Direct radiometric dating of the Devonian-Mississippian time-scale boundary using the Re-Os black shale geochronometer. Geology 33, 545–548.
Siebert, C., Nagler, T.F., von Blanckenburg, F., Kramers, J.D., 2003. Molybdenum isotope records as a potential new proxy for paleoceanography. Earth Planet. Sci. Lett. 211, 159–171.
Siebert, C., McManus, J., Bice, A., Poulson, R., Berelson, W.M., 2006. Molybdenum isotope signatures in continental margin marine sediments. Earth Planet. Sci Lett 241, 723–733.
Smith, M.G., Bustin, R.M., 1998. Production and preservation of organic matter during deposition of the Bakken Formation (Late Devonian and Early Mississippian), Williston Basin. Palaeogeogr. Palaeoclimatol. Palaeoecol. 142, 15–200.
Smith, M.G., Bustin, R.M., 2000. Late Devonian and Early Mississippian Bakken and Exshaw black shale source rocks, Western Canada Sedimentary Basin: a sequence stratigraphic interpretation. AAPG Bull. 84, 940–960.
Stirling, C.H., Andersen, M.B., Potter, E.K., Halliday, A.N., 2007. Low-temperature isotopic fractionation of uranium. Earth Planet. Sci. Lett. 264, 208–225.
Stirling, C.H., Andersen, M.B., Warthmann, R., Halliday, A.N., 2015. Isotope fractionation of $^{238}U$ and $^{235}U$ during biologically-mediated uranium reduction. Geochim. Cosmochim. Acta 163, 200–218.
Stockey, R.G., Cole, D.B., Planavsky, N.J., Loydell, D.K., Frýda, J., Sperling, E.A., 2020. Persistent global marine euxinia in the early Silurian. Nature Comm. 11, 1–10.
Stolfus, B.M., Cramer, B.D., Clark, R.J., Hogancamp, N.J., Day, J.E., IER-SURINE, S.A., Witzke, B.J., 2020. An expanded stratigraphic record of the Devonian-Carboniferous boundary Hangenberg biogeochemical Event from Southeast Iowa (USA). Bull Geosci. 95.
Stylo, M., Neubert, N., Wang, Y., Monga, N., Romaniello, S.J., Weyer, S., Bernier-Latmani, R., 2015. Uranium isotopes fingerprint biotic reduction. Proc. Natl. Acad. Sci. U.S.A. 112, 5619–5624.
Tissot, F.L., Chen, C., Go, B.M., Naziemiec, M., Healy, G., Bekker, A., Swart, P.K., Dauphas, N., 2018. Controls of eustasy and diagenesis on the $^{238}U/^{235}U$ of carbonates and evolution of the seawater ($^{234}U/^{238}U$) during the last 1.4 Myr. Geochim. Cosmochim. Acta 242, 233–265.
Tissot, F.L., Dauphas, N., 2015. Uranium isotopic compositions of the crust and ocean: Age corrections, U budget and global extent of modern anoxia. Geochim. Cosmochim. Acta 167, 113–143.
Tolokonnikova, Z., Ernst, A., 2021. Richness of Famennian-Tournaisian (late Devonian-early Carboniferous) bryozoans in shallow areas of Palaeotethys and Palaeoasian oceans. Palaeobio. Palaeoenv. 1–22.
Tribovillard, N., Algeo, T.J., Lyons, T., Riboulleau, A., 2006. Trace metals as paleoredox and paleoproductivity proxies: an update. Chem. Geol. 232, 12–32.
Tucker, R.D., Bradley, D.C., Ver Straeten, C.A., Harris, A.G., Ebert, J.R., McCutcheon, S. R., 1998. New U-Pb zircon ages and the duration and division of Devonian time. Earth Planet. Sci. Lett. 158, 175–186.
Voegelin, A.R., Pettke, T., Greber, N.D., von Niederhäusern, B., Nägler, T.F., 2014. Magma differentiation fractionates Mo isotope ratios: Evidence from the Kos Plateau Tuff (Aegean Arc). Lithos. 190, 440–448.
Walliser, O.H., 1984. Pleading for a natural D/C boundary. Cour. Forschungsinst. Senckenberg 67, 241–246.
Walliser, O.H., 1996. Global events in the Devonian and Carboniferous. In: Walliser, O. (Ed.), Global Events and Event Stratigraphy in the Phanerozoic. Springer-Verlag, pp. 225–250.
Wang, P., Chen, Z., Jin, Z., Jiang, C., Sun, M., Guo, Y., Chen, X., Jia, Z., 2018a. Shale oil and gas resources in organic pores of the Devonian Duvernay Shale, Western Canada Sedimentary Basin based on petroleum system modeling. J. Nat. Gas Sci.e Eng. 50, 33–42.
Wang, X., Planavsky, N.J., Reinhard, C.T., Hein, J.R., Johnson, T.M., 2016. A Cenozoic seawater redox record derived from $^{238}U/^{235}U$ in ferromanganese crusts. Am J. Sci. 316, 64–83.
Wang, X., Planavsky, N.J., Hofmann, A., Saupe, E.E., De Corte, B.P., Philippot, P., LaLonde, S.V., Jemison, N.E., Zou, H., Ossa, F.O., Rybacki, K., Alfimova, N., Larson, M.J., Tsikos, H., Fralick, P.W., Johnson, T.M., Knudsen, A.C., Reinhard, C.T., Konhauser, K.O., 2018b. A Mesoarchean shift in uranium isotope systematics. Geochim. Cosmochim. Acta 238, 438–452.
Warren, M.J., Cooper, M., 2017. Classic hydrocarbon traps and analog structures in the southern Canadian Rockies. AAPG Bull. 101, 589–597.
Wei, W., Algeo, T.J., 2020. Elemental proxies for paleosalinity analysis of ancient shales and mudrocks. Geochim. Cosmochim. Acta 287, 341–366.
Weyer, S., Anbar, A.D., Gerdes, A., Gordon, G.W., Algeo, T.J., Boyle, E.A., 2008. Natural fractionation of $^{238}U/^{235}U$. Geochimi. Cosmochim. Acta. 72, 345–359.
Willbold, M., Elliott, T., 2017. Molybdenum isotope variations in magmatic rocks. Chem. Geol. 449, 253–268.
Witzke, B.J., Heckel, P.H., 1988. Paleoclimatic indicators and inferred Devonian paleolatitudes of Euramerica. In: McMillan, N.J., Embry, A.F., Glass, D.J. (Eds.), Devonian of the World. Canadian Society Petroleum Geology, vol. 14, pp. 49–63.
Yang, S., Kendall, B., Lu, X., Zhang, F., Zheng, W., 2017. Uranium isotope compositions of mid-Proterozoic black shales: Evidence for an episode of increased ocean oxygenation at 1.36 Ga and evaluation of the effect of post-depositional hydrothermal fluid flow. Precambrian Res. 298, 187–201.

Zhang, F., Dahl, T.W., Lenton, T.M., Luo, G., Shen, S.Z., Algeo, T.J., Planavsky, N., Liu, J., Cui, Y., Qie, W., Romaniello, S.J., Anbar, A.D., 2020a. Extensive marine anoxia associated with the Late Devonian Hangenberg Crisis. Earth Planet. Sci. Lett. 533, 115976.

Zhang, F., Lenton, T.M., del Ray, Á., Romaniello, S.J., Chen, X., Planavsky, N.J., Clarkson, M.O., Dahl, T.W., Lau, K.V., Wang, W., Li, Z., Zhao, M., Isson, T., Algeo, T. J., Anbar, A.D., 2020b. Uranium isotopes in marine carbonates as a global ocean paleoredox proxy: A critical review. Geochim. Cosmochim. Acta 287, 27–49.

Zhang, X., Lin, C., Zahid, M.A., Jia, X., Zhang, T., 2017. Paleosalinity and water body type of eocene Pinghu formation, Xihu depression, East China Sea Basin. J. Petrol. Sci. Eng. 158, 469–478.

Zhang, S., Wang, X., Wang, H., Bjerrum, C.J., Hammarlund, E.U., Costa, M.M., Connelly, J.N., Zhang, B., Su, J., Canfield, D.E., 2016. Sufficient oxygen for animal respiration 1,400 million years ago. Proc. Natl. Acad. Sci. U.S.A. 113, 1731–1736.

Zhao, Z., Pang, X., Zou, C., Dickson, A.J., Basu, A., Guo, Z., Pan, S., Nielsen, A.T., Schovsbo, N.H., Jing, Z., Dahl, T.W., 2023. Dynamic oceanic redox conditions across the late Cambrian SPICE event constrained by molybdenum and uranium isotopes. Earth Planet. Sci. Lett. 604, 118013.

Zhao, H., Shen, J., Algeo, T.J., Racki, G., Chen, J., Huang, C., Song, J., Qie, W., Gong, Y., 2022. Mercury isotope evidence for regional volcanism during the Frasnian-Famennian transition. Earth Planet. Sci. Lett. 581, 117412.

Zhou, L., Wignall, P.B., Su, J., Feng, Q., Xie, S., Zhao, L., Huang, J., 2012. U/Mo ratios and $\delta^{98/95}$Mo as local and global redox proxies during mass extinction events. Chem. Geol. 324, 99–107.